Magnetic Resonance Imaging and Magnetic Resonance Spectroscopy Characterize a Rodent Model of Covert Stroke

by

Sheryl Lyn Herrera

A thesis submitted to the Faculty of Graduate Studies of

The University of Manitoba

in partial fulfilment of the requirements of the degree of

MASTER OF SCIENCE

Department of Physics & Astronomy

University of Manitoba

Winnipeg

Abstract

Covert stroke (CS) comprises lesions in the brain often associated by risk factors such as a diet high in fat, salt, cholesterol and sugar (HFSCS). Developing a rodent model for CS incorporating these characteristics is useful for developing and testing interventions. The purpose of this thesis was to determine if magnetic resonance (MR) can detect brain abnormalities to confirm this model will have the desired anatomical effects. *Ex vivo* MR showed brain abnormalities for rats with the induced lesions and fed the HFSCS diet. Spectra acquired on the fixed livers had an average percent area under the fat peak relative to the water peak of (20±4)% for HFSCS and (2±2)% for control. *In vivo* MR images had significant differences between surgeries to induce the lesions (p=0.04). These results show that applying MR identified abnormalities in the rat model and therefore is important in the development of this CS rodent model

Acknowledgements

I would first like to thank Dr. Melanie Martin for taking me on as a clueless undergrad those many years ago, and for opening my eyes to the opportunities that can be found being a physicist. It has been, and will continue to be a rewarding experience. Thank you Melanie for all the years of guidance, support, advice and caching you have given me since.

To my co-advisor Dr. Chris Bidinosti for taking me on as a student, as well as for helping edit my thesis. To my committee members, Dr. Esmat Elhami, Dr. Francis Lin, and Dr. Alberto Civetta, thank you for agreeing to read my thesis as reviewers for my defence. Many thanks to Dr. Richard Buist for his support and guidance and in his role in enhancing my knowledge and understanding of MRI. Thank you to Randy Summers for with helping me with my statistical analysis and for the added 'punch' to my results. Many thanks to Dr. Dale Corbett and his group at Memorial University of allowing me to participate in their study.

To my fellow lab members, many thanks to all of you for your help and advice: Dr. Jonathan Thiessen, Dr. Marzena Kastyak-Ibrahim, Trevor Vincent, Kerrie Hayes, and Laryssa Kurjewicz. Thank you to the administrative staff and the faculty in the Department of Physics and Astronomy for your guidance throughout my studies. To the faculty of the Department of Physics at the University of Winnipeg, many thanks to all of you for your support and encouragement all these years.

To my friends, even though you probably did not understand what I talked about you were all always there willing to let me go on and on, and just nod and smile. Thank you for putting up with my crazy. And lastly to my parents, my Nanay and Tatay, thank you for your support and patience in my pursuit to figure things out. *Maraming salamat sa iyo para sa iyong pag-ibig at suporta.*

I would like to acknowledge the funding for this project from The University of Manitoba and the Faculty of Graduate Studies, Memorial University, The University of Winnipeg, Natural Sciences and Engineering Council of Canada (NSERC), Canadian Foundation for Innovation (CFI), Manitoba Research and Infrastructure Fund (MRIF), as well as for the Faculty of Science at the University of Manitoba for funding my education.

Contents

List of Figures

List of Tables

1 Introduction

Stroke is the leading cause of death and disability with approximately 50,000 strokes occurring in Canada each year, with nearly 14,000 people dying from stroke. There are 315,000 Canadians living with the after-effects of stroke, and for those who survive, there is about a 20% chance of having another stroke within two years [1]. Ischemic stroke, the most common kind of stroke, is caused by the interruption of blood flow to the brain, and accounts for about 80% of all strokes. Stroke is often referred to as the 'silent killer' because unlike heart attack, it strikes without any warning. However, recent evidence [2-5] has revealed an even more insidious form of stroke distinguished by the fact that the more obvious symptoms of stroke (such as paralysis, loss of vision, impaired speech or comprehension, etc.) are not present. This type of stroke, termed 'covert stroke' does not produce acute clinical symptoms, but it cannot be considered benign, or even asymptomatic because it is often associated with an increased risk of cognitive impairments affecting executive function, attention and memory.

Several studies have shown that the prevalence of covert strokes, in comparison to acute clinical stroke, is several times higher in the general population, and it also rises appreciably with age and in select patient populations such as those with cardiovascular disease (CVD), depression, first ischemic stroke, and Alzheimer's disease [4-6]. Particularly alarming data shows that covert stroke increases the risk for stroke by about two to four times, and also doubles the risk for mild cognitive decline and the subsequent

progression to dementia [4,5,7]. There are currently no treatments for covert stroke, and with an aging population, the resulting burden on the Canadian health care system will increase dramatically.

Efforts to understand covert stroke better is needed, but an impediment to this disease and to the development of treatments is the lack of an animal model. Developing and characterizing a rodent model for covert stroke that would replicate the pattern of neurophysiological and cognitive decline in this disease could provide insights to the underlying mechanisms of injury and, more importantly, identify potential therapies that could be translated to the clinic.

1.1 Experimental Design

The goal of this project was to develop and characterize a rodent model of covert stroke which would replicate the pattern of neurophysiological and cognitive decline of this disease, ultimately to be able to develop therapies that could slow or reverse the symptoms. This project was a cross-country collaboration between Memorial University (MUN), University of Manitoba (UM), and the University of British Columbia (UBC). The team at MUN developed the rodent model, and assessed executive function with the use of behavioural tests such as the attentional set-shifting test [8]. This test (explained in Chapter 3) was used to measure the executive function because of its sensitivity to prefrontal injury in the brain, and it was also developed to further capture other aspects of

human executive function [9]. The UM team performed magnetic resonance imaging and spectroscopy (MRI and MRS) to follow morphological changes and lesion development in the rodent model, as well as detect changes in cerebral blood flow. The team at UBC performed microvascular functional assessment and mapping of electrophysiological function in regions that were associated with executive function. The work done at UBC will not be discussed in this thesis.

1.2 Covert Stroke

Covert stroke mainly comprises lacunar infarcts and diffuse white matter damage [6, 10-13]. Lacunar infarcts are a type of stroke that results from the occlusion (or blockage) of one of the penetrating arteries that provides blood to the brain's deep structures [14]. In covert stroke, the type of lacunar infarcts found are either single or multiple, and are small, with lesions ranging in size from 3 – 20 mm in diameter [6]. They are usually found in both the cortical and subcortical regions of the brain, and with the latter, in the basal ganglia or midline thalamus [6,11,12]. The thalamus, consisting of the anterior and medial dorsal nuclei, is involved in the storage of short-term memory [10]. Each time blockage to the arteries occurs, neural pathways are shut down and brain interconnectivity is reduced, creating the decline in executive function [15]. White matter damage frequently arises in the midline thalamic nuclei that may interrupt connections to the prefrontal cortex [7, 12,16,17] by slowing down information processing and interfering with the transfer of

information to the brain, which contributes to the development of executive cognitive dysfunction.

The cardiovascular disease risk factors of stroke are also associated with covert stroke. Hypertension and small vessel disease occurring in the small arteries and arterioles are the most widely accepted risk factors. A strong association exists between lacunar infarcts and these risk factors in most studies [6,10,11,18], because hypertension causes the thickening of the arterial walls and increased vascular stiffness [13]. The main consequence of covert stroke is the development of vascular cognitive impairment (VCI) which is the leading cause of disability in the elderly [19]. VCI is an epidemic that includes a wide range of cognitive disorders or impairments related to CVD, and occurring as a result of a variety of risk factors, such as hypertension, stroke, as well as covert stroke [20-23]. The onset of cognitive impairment is gradual and patients may not be aware of any problems because symptoms or signs of covert stroke only emerge after considerable disease progression, making it very difficult to develop treatments [10]. Studies show worse performance in the neurophysiological tests and a steeper decline in global cognitive functions for patients who were found to have lacunar infarcts compared to those without. These lacunar infarcts are associated with a decline in memory performance, and with non-thalamic infarcts being associated with a decline in psychomotor speed [11]. Studies have also shown that the lacunar infarcts and white matter damage attributed to small vessel disease have been associated with decreased brain volume [24], cognitive impairment [25-27], and cognitive decline [28-29], and an increased risk of dementia [5].

Developing and characterizing a rodent model for covert stroke that incorporates the several key clinical neuropathological features, namely white matter damage, small lacunar infarcts, co-morbidity risk factors (age, diet and hypertension), and most importantly, the progressive loss of cognitive function will be useful for determining if declining executive function can be attenuated or delayed by different interventions.

1.3 Animal Covert Stroke Model

No animal model will perfectly capture all aspects of covert stroke, but the model must be able to mimic the deficits that are a result of this disease as well as the associated neuropathology as closely as possible. Therefore, the model needed to have the neuropathological features seen in humans, namely the white matter damage and lacunar infarcts. Based on a review article by Hainsworth and Marcus [30] which examined fifteen ischemic models for the potential use as models of covert stroke, the model that was developed for this project incorporated the ideas of some of the models presented in this review article. One of the models from this review was the rat 2-vessel occlusion (or permanent bilateral carotid artery occlusion, 2-VO) model. This model resulted in prolonged hypoperfusion, or the reduction of blood flow in the vessels, which created the white matter damage akin to covert stroke. This model however did not produce any evident lacunar infarcts usually found in patients with covert stroke. Another model mentioned in this review was the spontaneously hyperintensive rat that did show signs of

lacunar infracts however the size of which were often much larger than the size of the infarcts generally found in covert stroke. Therefore in order to create lacunar infarcts found in the regions of the brain most affected by covert stroke, the protein Endothelin-1 (ET-1) was used. ET-1 produced ischemia by vasoconstriction [31], or the constriction of blood vessels, which in turn creates sporadic small infarcts.

This model also needed to reveal a progressive decline in cognitive function with aging (as in human covert stroke). Rats with 2-VO are impaired on a number of cognitive tasks, and like cognitive decline in humans, studies have found that these deficits develop over several months in the absence of major cell loss [32-35]. Additionally, common clinical co-morbidities including hypertension, diet and lifestyle were included in the model. A sedentary lifestyle and a diet high in fat, salt, cholesterol, and sugar (HFSCS diet) have been linked to cognitive decline in normal aging because both of these contribute to the increased risk of hypertension. Studies have shown that this type of diet may render the brain less able to respond to challenges arising from aging that were thought to contribute to the development of covert stroke [36].

In summary, in order for this model to mimic the effects of covert stroke in humans, the rodent model used in this project was the 2-VO rodent model in combination with discrete infusions of ET-1. The rodent model also incorporated the co-morbidity risk factors of age, diet and hypertension, all of which contribute to the progressive loss of cognitive function. The experimental design of this rodent model will be further discussed in

Chapter 3. The use of the 2-VO model is expected to reduce the blood flow to the brain and in turn create the white matter changes. By injecting the ET-1 into the regions of the brain most where lacunar infarcts tend to be found (i.e. the mediodorsal thalamic nucleus), this would produce the desired lacunar infarcts that are attributed to covert stroke. Lastly, incorporating cardiovascular risk factors, such as a sedentary lifestyle as well as a HFSCS diet, will also create the type of model that will be more susceptible to covert stroke.

1.4 The Use of Magnetic Resonance Imaging in Stroke

MR imaging, as described in Chapter 2, is an important clinical tool for the differential diagnosis of dementia and for monitoring disease progression. The most common clinical pulse sequences use the difference in relaxation times, T_1 and T_2, between tissues to show contrast. T_2-weighted MR imaging has been used to measure cerebral atrophy [14,37] and white matter lesions [38,39], with these results correlating with neurological impairment [39]. T_2-weighted MRI is sensitive enough to identify edema in stroke, however it is not reliable in the first 12 hours after the onset of symptoms to identify a stroke [40-42]. Diffusion weighted imaging (DWI) is used for the detection of early changes in stroke, as well as in other diseases. Contrast in these images respresent variations in the random motion of water molecules in tissues which vary with various brain pathologies, including acute ischemic stroke. White matter damage appears as hyperintensites in T_2-weighted

MRI [7,12,16,17]. Lacunar infarcts, which are areas of dead tissue which fill up with fluid and may show up as dark spots in T_1-weighted MRI and bright spots in T_2-weighted and diffusion-weighted MRI [15,43,44].

Because T_2-weighted MRI is not as reliable as DWI at the onset of stroke symptoms, DWI is typically used as a diagnostic technique for stroke. In humans, ischemic lesions in the brain initially become hypointense in DWI within minutes to a few hours [43,45-48]. These lesions then become hyperintense with an increasing signal intensity and eventually reaching its maximum intensity at about one week after symptom onset before the normalization of DWI occurs. The normalization is most likely as a result of water diffusivity and the intrinsic T_2 properties of tissue being examined [46,49,50]. From this point, although lesions still appear hyperintense, the intensity of the signal fades for a period of about 3 weeks after the onset of symptoms. Because of this, the sensitivity of DWI for detecting recent ischemic damage starts to diminish after 3 weeks and may even fail to pinpoint lesions in humans. In humans, T_2-weighted images remain hyperintense for a long period of time and reaches its maximum between 7 – 30 days, before the signal intensity decreases and eventually fades [47]. In animals, this time period is drastically shorter; hypointense DWI within minutes of onset of stroke; hyperintense within an hour and reaching a maximum signal intensity at approximately 24 hours after onset, before signal intensity fades at about 48 hours [41,49].

In the studies presented in this thesis, and explained in Chapter 3, the rats were imaged at 9 weeks after the induction of the infarcts and the reduction of blood flow to create the white matter damage. The rats were imaged at this time to mimic middle age in humans for rats of this particular strain. Because the images were taken at this age point, DWI was not performed on these rats because it would fail to detect any of the lesions at this time period. Instead T_2-weighted imaging was performed to verify the presence of lesions.

1.5 Goals

The purpose of this thesis was to determine if MRI and magnetic resonance spectroscopy (MRS) are sensitive enough of a modality to detect abnormalities in the brain morphology – lacunar infarcts and white matter damage, as well as detect any physical changes created by a HFSCS diet, ultimately to confirm that this new rodent model will have the desired anatomical and behavioural effects.

In the remainder of this thesis, magnetic resonance imaging will be discussed (Chapter 2), followed by experimental design (Chapter 3), the presentation and interpretation of the results (Chapter 4 and 5), conclusions (Chapter 6), and the possibility of future work on this experiment (Chapter 7).

2 Theory

2.1 Nuclear Magnetic Resonance

Magnetic resonance imaging (MRI) is founded on the basis of nuclear magnetic resonance (NMR) which was experimentally demonstrated in 1946 independently by Purcell et al.[51] and Bloch [52]. In this chapter, the phenomenon of NMR will be explained, expanding from that NMR imaging and NMR spectroscopy.

2.1.1 Nuclear Magnetic Moments

Most MRI uses the signal produced from the nucleus of a hydrogen atom (^{1}H) for image generation. Nuclei of a hydrogen atom possess a proton which has a positive electric charge. Because of this charge, the proton in the nucleus rotates about its own axis as if it has a nonzero spin and possesses a magnetic dipole moment $\vec{\mu}$ which in turn produces a magnetic field, behaving similar to that of a bar magnet (Figure 2.1).

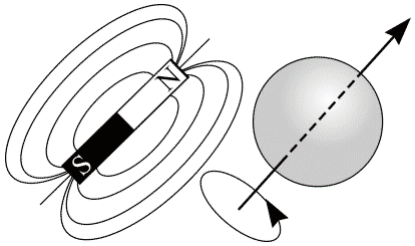

Figure 2.1: A charged nucleus, spins about its own axis and creates a magnetic moment similar to that of a bar magnet (modified from [53,54]).

These nuclear magnetic moments have a random orientation in the absense of an externally applied magnetic field. (Figure 2.2 (a)). When an external magnetic field is applied, the magnetic moment vectors become oriented in one of two directions (parallel or anti-parallel) with respect to the applied magnetic field B_o (Figure 2.2 (b), (c)).

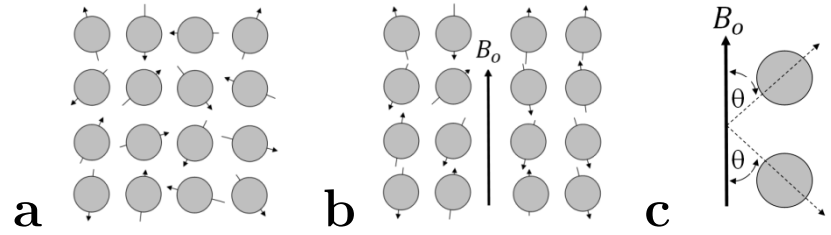

Figure 2.2: (a) Nuclear magnetic moment vectors have random orientations when no magnetic field is present. (b) Magnetic moment vectors become oriented in one of two directions with respect to the applied magnetic field B_o. (c) Nuclei either align themselves either point parallel or anti-parallel with respect to the B_o field. (modified from [53,54])

Although the properties of spin in particles are quantum in nature, they can also be described by classical mechanics, because MRI depends on a large group of spins which is classical in nature [55]. Using the classical mechanics vector model, when a magnetic dipole moment $\vec{\mu}$ is placed in an external magnetic field $\vec{B_o}$, its motion is similar to that of a spinning top, which experiences a torque (Figure 2.3).

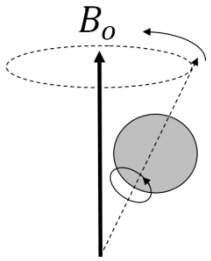

Figure 2.3: Precession of the nuclear magnetic moment about an external field is similar to a spinning top in a gravitational field. (modified from [54])

The classical equation of the motion of the magnetic dipole moment in equilibrium in a static magnetic field is

$$\frac{d\vec{\mu}}{dt} = \gamma\, \vec{\mu} \times \overrightarrow{B_o}. \tag{2.1}$$

The solution to the Equation (2.1) using the convention in MRI to assign the z-axis to align with the magnetic field B_o is expressed as follows [53]:

$$\begin{cases} \mu_{xy}(t) = \mu_{xy}(0)e^{-i\gamma B_o t}, \\ \mu_z(t) = \mu_z(0) \end{cases} \tag{2.2}$$

where
$$\mu_{xy}(t) = \begin{cases} \mu_x(t) = \mu_x(0)\cos(\gamma B_o t) + \mu_y(0)\sin(\gamma B_o t) \\ \mu_y(t) = -\mu_x(0)\sin(\gamma B_o t) + \mu_y(0)\cos(\gamma B_o t) \end{cases}. \tag{2.3}$$

This describes a vector with a z-component that does not change the xy-component rotating about the z-axis. Thus the vector precesses about the z-axis with a frequency ω_o, known as the Larmor frequency:

$$\vec{\omega}_o = -\gamma \vec{B}_o, \tag{2.4}$$

where γ is the gyromagnetic ratio which is dependent on the nucleus. It can be written in the form of another constant $\bar{\gamma} = \frac{\gamma}{2\pi}$ which changes the units to Hertz (Hz) from radians/seconds. The ^{1}H atom has a gyromagnetic ratio of $\gamma = 2.675 \times 10^8$ rad/sec·T or $\bar{\gamma} = 42.58$ MHz/T. The MRI scanner used in this thesis has a magnetic field of $B_o = 7T$ which results in a Larmor frequency of $f_o = 300\, MHz$.

When placed in an external magnetic field, the nuclear dipoles have an energy associated with their alignment in the z-axis, which is given by

$$E = -\vec{\mu} \cdot \overrightarrow{B_o} = -\mu_z B_o = -\gamma \hbar m_I B_o, \tag{2.5}$$

where m_I is the spin quantum number. Because $m_I = \pm\frac{1}{2}$, the spin-$\frac{1}{2}$ ^{1}H nucleus has 2 energy states:

$$E_\uparrow = -\frac{1}{2}\gamma\hbar B_o \quad and \quad E_\downarrow = +\frac{1}{2}\gamma\hbar B_o \quad . \tag{2.6}$$

The energy difference between these two states is

$$\Delta E = E_\downarrow - E_\uparrow = \gamma\hbar B_o \ . \tag{2.7}$$

The two different energy states correspond with the proton magnetic moments aligning parallel (lower energy) or anti-parallel (higher energy) with B_o, where this energy level splitting is known as the Zeeman effect as shown in Figure 2.4.

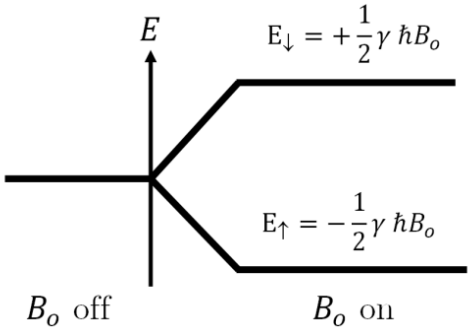

Figure 2.4: Zeeman splitting for a spin-$\frac{1}{2}$ system with an applied magnetic field, B_o.

A nucleus in the lower energy state would need to absorb a photon with energy $\Delta E = \gamma\hbar B_o = \hbar\omega_o$ to move to the higher energy state and $\omega_o = \gamma B_o$ is exactly the Larmor frequency.

To calculate the relative number of protons in the parallel state $N_\uparrow$ versus the anti-parallel state $N_\downarrow$ in thermal equilibrium, the Boltzmann equation is used:

$$\frac{N_\uparrow}{N_\downarrow} = \exp\left(\frac{\Delta E}{k_B T}\right) = \exp\left(\frac{\gamma \hbar \mathrm{B_o}}{k_B T}\right) \tag{2.8}$$

where T is the temperature of the spin system (for live imaging body temperature is about 310 K), k_B is the Boltzmann constant ($k_B = 1.38 \times 10^{-23}\, J/K$), $\hbar$ is Planck's constant ($\hbar = 1.05546 \times 10^{-34}\, J \cdot s$), and γ is gyromagnetic ratio.

The ratio of $\frac{N_\uparrow}{N_\downarrow}$ for the following conventional clinical and animal MRI magnetic fields are given as follows:

$$\frac{N_\uparrow}{N_\downarrow} = \exp\left(\frac{2\pi(42.58\times10^{6}\frac{\mathrm{Hz}}{\mathrm{T}})(1.05546\times10^{-34}\, J\cdot s)\mathrm{B_o}}{(1.38\times10^{-23}\frac{J}{K})(310\, K)}\right).$$

For experiments performed for this thesis at a magnetic field of $B_o = 7T$ which corresponds to $\Delta E = \gamma \hbar B_o = 1.976 \times 10^{-25}$, the ratio of dipoles in the two energy states is $\frac{N_\uparrow}{N_\downarrow} = 46 \times 10^{-6}$. Table 2.1 gives the ratio of $\frac{N_\uparrow}{N_\downarrow}$ for magnetic fields at 1.5, 3.0, 7 and 11.7 Tesla.

Table 2.1: Ratio of $\frac{N_\uparrow}{N_\downarrow}$ for magnetic fields at 1.5, 3.0, 7 and 11.7 Tesla

B_o	$1.5\,(T)$	$3.0\,(T)$	$7.0\,(T)$	$11.7\,(T)$
$\frac{N_\uparrow}{N_\downarrow}$	9.9×10^{-6}	20×10^{-6}	46×10^{-6}	77×10^{-6}

2.1.2 Net Magnetization Vector

The difference in the number of nuclei aligned parallel and anti-parallel to B_o leads to a net magnetization vector $\vec{M}$ that is used to generate a signal. By adding all the individual dipole moments $\overrightarrow{\mu_n}$ in a sample, we obtain the net magnetization

$$\vec{M} = \sum_{n=1}^{N} \overrightarrow{\mu_n} = \left(\sum_{n=1}^{N} \mu_{x,n}\right)\hat{x} + \left(\sum_{n=1}^{N} \mu_{y,n}\right)\hat{y} + \left(\sum_{n=1}^{N} \mu_{z,n}\right)\hat{z}\,, \tag{2.9}$$

where N is the total number of spins in a unit volume. Because there is no preferential orientation in the xy-plane, the x- and y- components of the magnetization vector averages to zero, thus

$$\vec{M} = \left(\sum_{n=1}^{N} \mu_{z,n}\right)\hat{z} = \left(\sum_{n=1}^{N} \gamma\hbar(m_I)_n\right)\hat{z}\,. \tag{2.10}$$

For ^{1}H nuclei,

$$\sum_{n=1}^{N} (m_I)_n = \frac{1}{2}(N_\uparrow - N_\downarrow) \tag{2.11}$$

therefore the magnetization vector becomes:

$$\vec{M} = \left[\gamma\hbar\frac{1}{2}(N_\uparrow - N_\downarrow)\right]\hat{z} \tag{2.12}$$

In practice, because the energy difference is so small $(\Delta E \ll k_B T)$, by first order approximation, Equation (2.8) can be written as

$$N_\uparrow - N_\downarrow \cong \frac{N}{2}\frac{\gamma\hbar B_o}{k_B T}\,. \tag{2.13}$$

For the experiments in this thesis with magnetic field at $B_o = 7T$, the difference of dipoles is $N_\uparrow - N_\downarrow \cong 23$ ppm. The difference, $N_\uparrow - N_\downarrow$, for the following clinical and animal MRI magnetic fields are given in Table 2.2. with $N = 10^6$ total dipoles.

Table 2.2: Difference $N_\uparrow - N_\downarrow$ in ppm for magnetic fields 1.5, 3.0, 7.0, 11.7 Tesla

B_o	$1.5\ (T)$	$3.0\ (T)$	$7.0\ (T)$	$11.7\ (T)$
$N_\uparrow - N_\downarrow$	5.0	9.9	23	39

Combining Equations (2.12) and (2.13) gives the magnitude of the magnetization vector at equilibrium

$$\vec{M}_o = \left[\gamma\hbar\frac{1}{2}\left(\frac{N}{2}\frac{\gamma\hbar B_o}{k_B T}\right)\right]\hat{z} = \frac{N}{4}\frac{\gamma^2\hbar^2 B_o}{k_B T}\hat{z}\,. \tag{2.14}$$

which points exactly along the positive direction of the z-axis. Here, this magnitude of $\vec{M}$ is directly proportional to the total number of spins N, and also to the external magnetic strength B_o with $M_o \ll B_o$ because it is static at equilibrium.

2.2 Magnetic Resonance Signal

In order to produce an MR signal, the spin system needs to be perturbed or excited using an external force such as a radio frequency (RF) pulse. The components required to produce an MR signal will be discussed in this section, namely RF-pulses and extending from that the rotating frame of reference, Bloch equation and the flip angle.

2.2.1 Radio-Frequency Pulse

In order to measure the NMR signal generated, the magnetization vector $\vec{M}$ must be made to vary with time. This is done by applying a radio frequency (RF) pulse. An RF pulse is a short, time-varying magnetic field $\vec{B}_1$ that is perpendicular to the main magnetic field $\vec{B}_o$ with $|\vec{B}_1| \ll |\vec{B}_o|$. The B_1 field, for example, can take on the following form:

$$\vec{B}_1(t) = B_1 \cdot \cos(\omega_o t).$$

The NMR signal arises from the transitions between the two energy states of protons, with energy difference of $\Delta E = \gamma \hbar B_o$ as given in Equation (2.7). Thus the B_1 field must supply this energy $\Delta E = \gamma \hbar B_o$ so that the nuclei can move from the lower state to the higher state. Therefore the B_1 field must vary in time with frequency ω_o and for typical MR field strengths, ω_o is within the RF range.

The RF pulse is described by the function [53]

$$\vec{B}_1(t) = B_1^e(t)\,[\cos(\omega_o t + \phi)\hat{x} - sin(\omega_o t + \phi)\hat{y}]. \tag{2.15}$$

This can also be written in complex form:

$$\vec{B}_1(t) = B_1^e(t) e^{-i(\omega_o t + \phi)}\ , \tag{2.16}$$

where ω_o is the frequency of the applied RF pulse, ϕ is the initial phase angle of the B_1 field, and $B_1^e(t)$ is the envelope of the pulsed RF function, which describes its shape and

duration. Common shapes for RF pulses are rectangle and sinc, the reasoning for these two typical pulse shapes will be given in Section 2.7.1.

A rectangular pulse can be defined as

$$B_1^e(t) = B_1 \prod \left(\frac{t - \tau_P/2}{\tau_P} \right). \tag{2.17}$$

where τ_P is the pulse width, and Π is a boxcar function that is zero outside the interval t=$[0, \tau_P]$ and at an amplitude of B_1 inside this interval. A sinc pulse can be defined as

$$B_1^e(t) = \begin{cases} B_1 sinc\left[\pi \Delta f \left(t - \frac{\tau_P}{2}\right)\right] \; ; \; 0 \leq t \leq \tau_P \\ 0 \quad ; \; t > \tau_P \end{cases}. \tag{2.18}$$

where the peak of the main lobe of the pulse is at an amplitude of B_1 when $t = \frac{\tau_P}{2}$, which makes sinc(0)=1. The zeroes of this curve are found at $t = \pm n\pi + \frac{\tau_P}{2}$ for $n = 1, 2, ...$, with the main lobe found between $\pm\pi + \frac{\tau_p}{2}$.

The shape of the rectangle and sinc RF pulses are given in Figure 2.5.

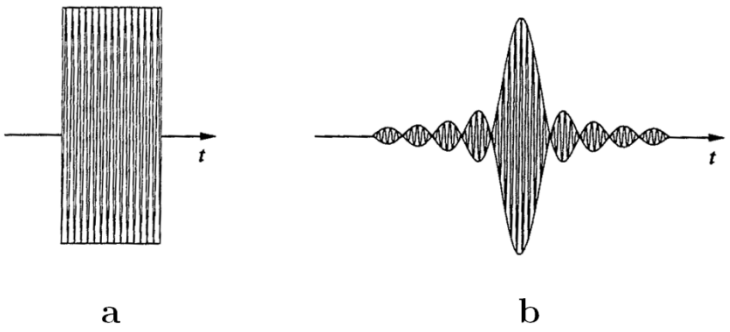

Figure 2.5: RF pulses with (a) rectangle envelope function, and (b) sinc envelope function[53].

2.2.2 Rotating Frame of Reference

To explain the effect of the rotating magnetization vector $\vec{M}$ from the rotating B_1 field, $\vec{M}$ and B_1 can be viewed in a reference frame rotating at the same rate as $\vec{M}$ or B_1, that is at a rate of Larmor frequency, ω_o. Mathematically, the rotating frame is a transformation expressed as follows:

$$\begin{Bmatrix} \hat{x}' = \cos(\omega_o t)\,\hat{x} - sin(\omega_o t)\hat{y} \\ \hat{y}' = \cos(\omega_o t)\,\hat{x} + sin(\omega_o t)\hat{y} \\ \hat{z}' = \hat{z} \end{Bmatrix} \tag{2.19}$$

Rewriting the B_1 field in terms of x and y components

$$\text{(i)} \qquad \vec{B}_1(t) = B_{1x}(t)\hat{x} + B_{1y}(t)\hat{y} \tag{2.20}$$

$$\text{(ii)} \qquad \vec{B}_{1,rot}(t) = B_{1x'}(t)\hat{x}' + B_{1y'}(t)\hat{y}',$$

where in the (i) laboratory frame, the spin system precesses about the magnetic field at Larmor frequency, and in (ii) the entire rotating frame rotates at Larmor frequency.

The magnetization vector, can also be written in terms of x and y components

$$\text{(i)} \qquad \vec{M} = M_x\hat{x} + M_y\hat{y} + M_z\hat{z} \tag{2.21}$$

$$\text{(ii)} \qquad \vec{M}_{rot} = M_{x'}\hat{x}' + M_{y'}\hat{y}' + M_{z'}\hat{z}'$$

where (i) is in the laboratory frame, and (ii) is in the rotating frame. To convert the magnetization vector and $\vec{B}_1$ vector between the laboratory and the rotating frame, the following coordinate transformations are performed respectively in Equations (2.22) and (2.23).

Setting $\vec{M}_{rot} = \vec{M}$ gives the transformation as follows:

$$\begin{bmatrix} M_{x'} \\ M_{y'} \\ M_{z'} \end{bmatrix} = \begin{bmatrix} \cos(\omega_o t) & -\sin(\omega_o t) & 0 \\ \sin(\omega_o t) & \cos(\omega_o t) & 0 \\ 0 & 0 & 1 \end{bmatrix} \begin{bmatrix} M_x \\ M_y \\ M_z \end{bmatrix}. \tag{2.22}$$

Similarly, setting $\vec{B}_{1,rot} = \vec{B}$ gives the transformation of

$$\begin{bmatrix} B_{1x'} \\ B_{1y'} \end{bmatrix} = \begin{bmatrix} \cos(\omega_o t) & -\sin(\omega_o t) \\ \sin(\omega_o t) & \cos(\omega_o t) \end{bmatrix} \begin{bmatrix} B_{1x} \\ B_{1y} \end{bmatrix}. \tag{2.23}$$

The precession of the magnetization vector in the presence of a rotating RF field can be observed as shown in Figure 2.6.

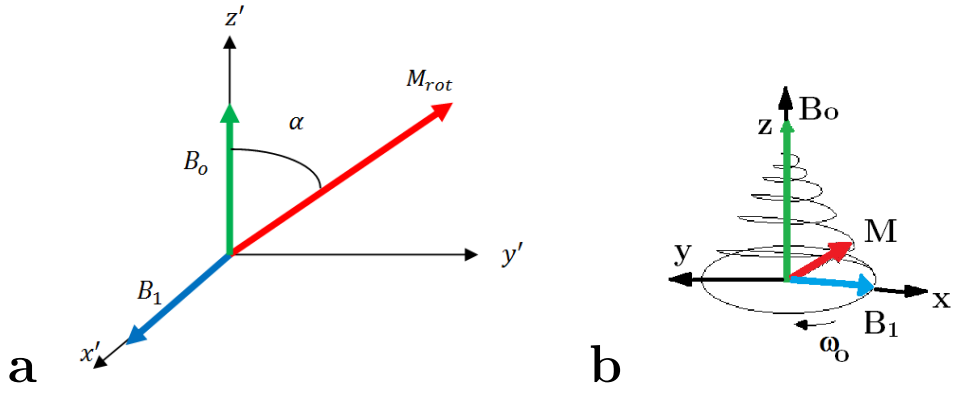

Figure 2.6: The precession of net magnetization in (a) the rotating frame and (b) the laboratory frame. The angle at which the RF field tips M_{rot} is denoted as α in the rotating frame. In the laboratory frame the magnetization spirals down towards the transverse plane as it is under the influence of the longitudinal field B_o and the transverse field (modified from [56]).

2.2.3 Bloch Equation

The time-dependent change of the net magnetization vector $\vec{M}$ is described by the Bloch [52] Equation:

$$\frac{d\vec{M}}{dt} = \gamma\vec{M} \times \vec{B} - \frac{M_x\hat{x} + M_y\hat{y}}{T_2} - \frac{M_z\hat{z} - M_o\hat{z}}{T_1}, \tag{2.24}$$

where M_o is the thermal equilibrium value for $\vec{M}$ in the presence of B_o only, T_1 is the relaxation time constant for the longitudinal magnetization to the return to equilibrium after an RF pulse, and T_2 is the relaxation time constant in the presence of a perfectly uniform external field $\overrightarrow{B_o}$ for the transverse magnetization to decay after an RF pulse. For explanation of the relaxation time constants see Section 2.3.

The Bloch equation during an RF pulse can take on a simpler form (ignoring the last two terms) because the duration of B_1 is much shorter than the relaxation times. During the RF pulse, the Bloch equation is simplified to

$$\frac{d\vec{M}}{dt} = \gamma\vec{M} \times \vec{B}\,. \tag{2.25}$$

By taking the first derivative of $\overrightarrow{M}$ with respect to time from Equation (2.21) in the rotating frame gives

$$\frac{d\vec{M}}{dt} = \hat{x}'\frac{dM_{x'}}{dt} + \hat{y}'\frac{dM_{y'}}{dt} + \hat{z}'\frac{dM_{z'}}{dt} + M_{x'}\frac{d\hat{x}'}{dt} + M_{y'}\frac{d\hat{y}'}{dt} + M_{z'}\frac{d\hat{z}'}{dt}$$

$$\Rightarrow \qquad \frac{d\vec{M}}{dt} = \left[\frac{d\vec{M}}{dt}\right]_{rot} + M_{x'}\frac{d\hat{x}'}{dt} + M_{y'}\frac{d\hat{y}'}{dt} + M_{z'}\frac{d\hat{z}'}{dt} \tag{2.26}$$

The time derivatives of the unit vectors can be written as:

$$\frac{d\hat{x}'}{dt} = \vec{\omega} \times \hat{x}'\,;\ \frac{d\hat{y}'}{dt} = \vec{\omega} \times \hat{y}'\,;\ \frac{d\hat{z}'}{dt} = \vec{\omega} \times \hat{z}' \tag{2.27}$$

where in this case, $\vec{\omega} = -\omega\hat{z}$.

Combining Equations (2.26) and (2.27), we get the following:

$$\left[\frac{d\vec{M}}{dt}\right]_{lab} = \left[\frac{d\vec{M}}{dt}\right]_{rot} + \vec{\omega} \times \vec{M}_{rot}. \tag{2.28}$$

Because $\vec{M}_{rot} = \vec{M}$, it can also be written as

$$\left[\frac{d\vec{M}}{dt}\right]_{lab} = \left[\frac{d\vec{M}}{dt}\right]_{rot} + \vec{\omega} \times \vec{M}. \tag{2.29}$$

Solving for the change of $\vec{M}$ in the rotating frame, or $\left[\frac{d\vec{M}}{dt}\right]_{rot}$, this becomes

$$\left[\frac{d\vec{M}}{dt}\right]_{rot} = \left[\frac{d\vec{M}}{dt}\right]_{lab} - \vec{\omega} \times \vec{M}. \tag{2.30}$$

By substituting Equation (2.25) into (2.30) gives

$$\left[\frac{d\vec{M}}{dt}\right]_{rot} = \gamma\vec{M} \times \left(\vec{B} + \frac{\vec{\omega}}{\gamma}\right). \tag{2.31}$$

The effective magnetic field the magnetization vector 'experiences' in the rotating frame is

$$\vec{B}_{eff} = \vec{B}_{rot} + \frac{\vec{\omega}}{\gamma} \tag{2.32}$$

Therefore if we let $\vec{B}_{rot} = B_o\hat{z}$ and $\vec{\omega} = -\gamma B_o\hat{z}$, then $\vec{B}_{eff} = B_{rot} - \frac{\gamma B_o\hat{z}}{\gamma} = B_o\hat{z} - B_o\hat{z} = \mathbf{0}$.

This shows that the apparent longitudinal field vanishes and $\vec{M}_{rot}$ appears to be stationary in the rotating frame. Therefore the full Bloch equation (Equation (2.24)) can be expressed in the rotating frame as

$$\frac{\partial\vec{M}_{rot}}{\partial t} = -\frac{M_x\hat{x} + M_y\hat{y}}{T_2} - \frac{M_z\hat{z} - M_o\hat{z}}{T_1} \tag{2.33}$$

because $\gamma\vec{M}_{rot} \times \vec{B}_{eff} = 0$.

2.2.4 Flip Angle

The angle that the magnetization vector $\vec{M}$ rotates through from the application of an RF pulse is called the flip or tip angle. It is defined as the angle between the $\vec{M}$ and the z-axis (see Figure 2.7). The equation for the flip angle is given as

$$\alpha = \int_0^{\tau} \gamma B_1^e(t)dt \tag{2.34}$$

where α is the flip angle, and $B_1^e(t)$ is the pulse envelope function.

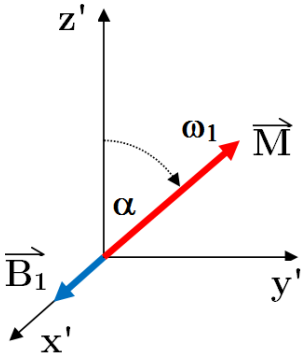

Figure 2.7: Flip angle. With an applied external magnetic field B_1, the net magnetization vector $\vec{M}$ flips through an angle α.

With an applied external magnetic field, $\vec{B}_1 = B_1\hat{x}'$, the magnetization vector $\vec{M}$ rotates through an angle of α and rotates in the y' and z' plane.

For a rectangular pulse of duration τ, this angle reduces to the following:

$$\alpha = \gamma B_1^e \tau \tag{2.35}$$

The flip angle depends on the pulse duration of τ and strength of the B_1 field. The frequency of B_1 is the same as the Larmor frequency which means that the pulse is on-resonance. Off-resonance pulses also exist in MR but are beyond the scope of this thesis.

An RF B_1 pulse that rotates the magnetization vector $\vec{M}$ through the angle α is referred to as an alpha-pulse. For example, rotating $\vec{M}$ by 90° is referred to as a 90°-pulse or $\frac{\pi}{2}$-pulse, and rotating $\vec{M}$ by 180° is referred to as a 180°-pulse or π-pulse. In general, the amount of transverse magnetization M_{xy} is given by:

$$M_{xy} = |\vec{M}| \cdot \sin(\alpha) \tag{2.36}$$

Using Equation (2.36), the 90^o-pulse results in the maximal signal at: $M_{xy} = M_o \sin(90^o) = M_o$, and the 180^o-pulse results in a minimal signal at: $M_{xy} = M_o \sin(180^o) = 0$, and is shown on Figure 2.8.

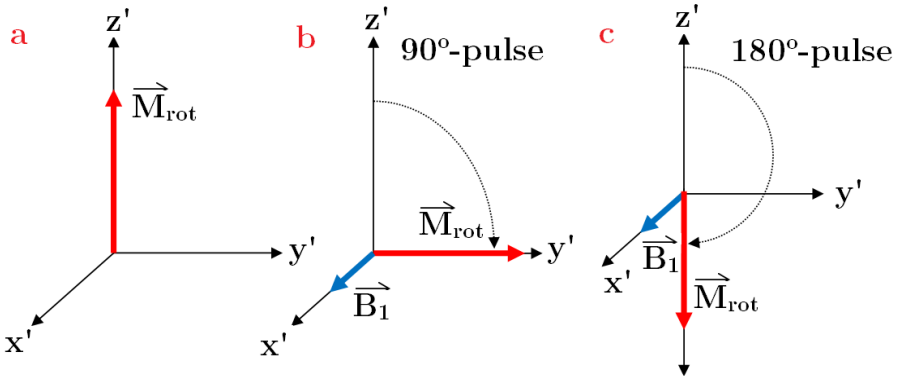

Figure 2.8: Net Magnetization vector $\vec{M}_{rot}$ in the rotating frame at: (a) equilibrium, (b) following a 90^o-pulse, and (c) following a 180^o-pulse.

2.3 Relaxation

As discussed in Section 2.2, in order to produce an MR signal the spin system needs to be perturbed using an external force, such as an RF-pulse. Once this RF-pulse is removed, the spin system will eventually return or recover to its initial equilibrium state via a process known as *spin-lattice* or *longitudinal relaxation*. Spin-lattice or longitudinal relaxation is the term given for the exponential growth of M_z, wherein the spin system exchanges energy with the lattice which consists of the molecular arrangement and structure of the object. Once in equilibrium, the magnetization has its maximum value of M_o and is aligned with the strong magnetic field taken in the z-direction (see Figure 2.9).

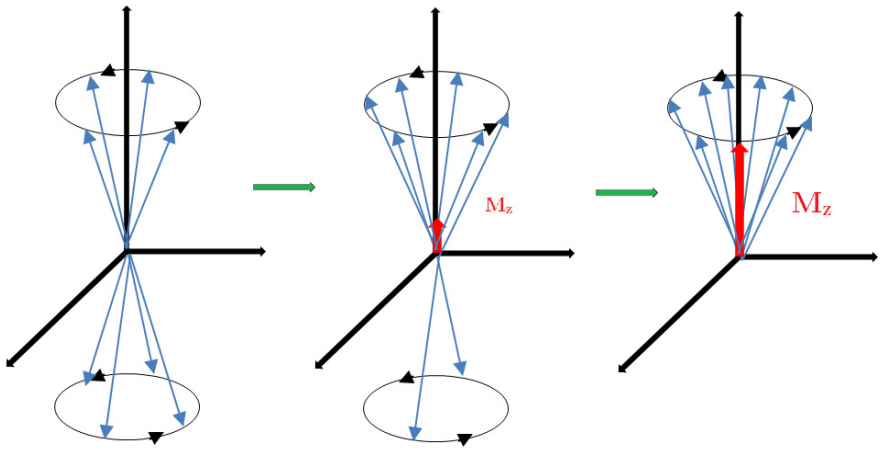

Figure 2.9: The magnetic moments will spontaneously return to a lower energy state (thermal equilibrium), and thus return the longitudinal magnetization M_z to its full value. The time constant for this is called T_1 (modified from [57]).

The effect of spin-lattice or longitudinal relaxation can be described using the Bloch equation as

$$\frac{dM_z}{dt} = \frac{M_o - M_z}{T_1} \tag{2.37}$$

where M_z is the longitudinal magnetization recovered after a time t in an object, and T_1 is the spin-lattice or longitudinal relaxation time. The solution to this differential Equation (2.37) is given as

$$M_z(t) = M_z(0) \cdot \mathrm{e}^{\left(-\frac{t}{T_1}\right)} + M_o\left[1 - \mathrm{e}^{\left(-\frac{t}{T_1}\right)}\right], \tag{2.38}$$

where M_o is the longitudinal magnetization at equilibrium, and $M_z(0)$ is the initial value after the completion of the RF-pulse. If a 90^o-pulse is applied, this sets $M_z(0) = 0$, which changes this equation to

$$M_z = M_o(1 - e^{-t/T_1}) \tag{2.39}$$

and is shown graphically in Figure 2.10.

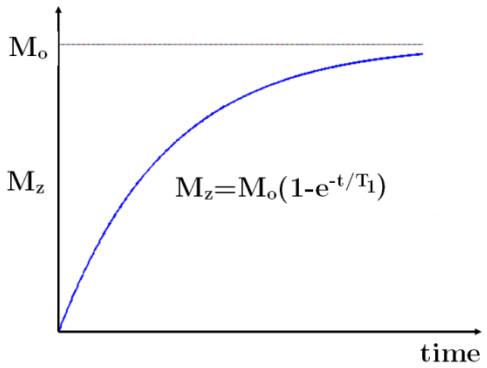

Figure 2.10: A T_1 curve, where $M_z(0) = 0$, which could happen after a 90°-pulse, for instance. The longitudinal magnetization becomes re-established in an exponential manner characterized by the time constant T_1.

The component of magnetization in the transverse plane goes to zero via a process called *spin-spin relaxation* or *transverse relaxation*. This spin-spin or transverse relaxation is the term given to represent the spin-spin interactions that cause the loss of phase coherence due the intrinsic magnetic properties of the object. In this process, spins exchange energy amongst themselves and become less ordered, which corresponds to an increase in the entropy of the system, shown in Figure 2.11.

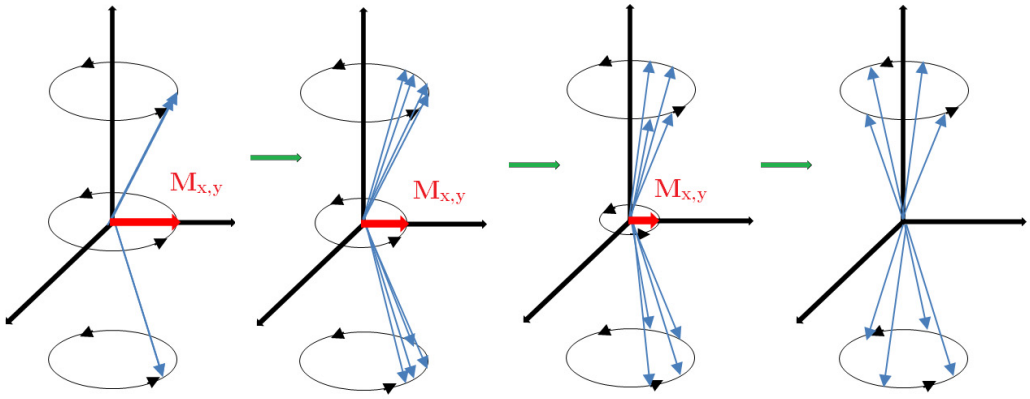

Figure 2.11: Spin-spin interactions cause the magnetic moments to dephase. The time constant for this is referred to as T_2^*. (modified from [57])

Similar to the equation for longitudinal magnetization (Equation (2.39)), the effect of spin-spin relaxation is described with the use of the Bloch equation as

$$\frac{dM_{xy}}{dt} = \frac{M_{xy}}{T_2} \tag{2.40}$$

where M_{xy} is the transverse component of magnetization (xy-plane) as a function of time after the RF pulse, and T_2 is the spin-spin relaxation time, or transverse relaxation time.

A solution to Equation (2.40) is given as

$$M_{xy}(t) = M_{xy}(0)\exp\left(-\frac{t}{T_2}\right), \tag{2.41}$$

and is graphically shown in Figure 2.12 for the case after a 90^o-pulse which sets $M_{xy}(0) = M_o$ and changes the equation to be

$$M_{xy}(t) = M_o e^{-t/T_2}. \tag{2.42}$$

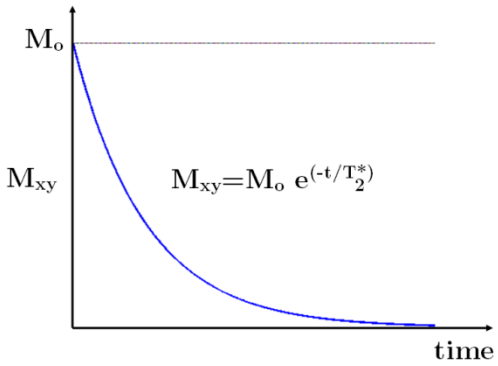

Figure 2.12: A T_2 decay curve for the magnetization after a 90°-pulse. The transverse magnetization decreases in an exponential manner characterized by the time constant T_2. It can also be caused by the inhomogeneities of the magnetic field, giving the time constant T_2^* as explained in Equation (2.42).

The T_2 decay mechanisms are determined by the molecular structure of the sample. If the main magnetic field is not homogeneous, the loss of phase coherence may occur more rapidly than the spin-spin interactions themselves. When B_o inhomogeneity is considered, the spin-spin decay constant, T_2, is changed to T_2^* to take into account the extra dephasing which occurs due to the field inhomogeneities [58]. This T_2^* is often defined as

$$\frac{1}{T_2^*} = \frac{1}{T_2} + \frac{1}{T_2'} \tag{2.43}$$

where T_2' represents factors such as local field inhomogeneities that cause magnetization to dephase faster. This equation is an approximation of the real interactions but will suffice for the descriptions in this thesis.

2.4 Signal Detection

MR detection is based on Faraday's law of electromagnetic induction where the voltage generated in a coil is proportional to the rate at which the magnetic flux through a coil changes. According to Faraday's law of induction and the principles of reciprocity, a time varying magnetization $\vec{M}(\vec{r}, t)$ will induce a voltage $V(t)$ in a receiver coil which is often regarded as the raw NMR signal [53] expressed as follows:

$$V(t) \propto -\frac{\partial}{\partial t}\int_{object} \vec{B}(\vec{r}) \cdot \vec{M}(\vec{r}, t)\, d\vec{r}, \tag{2.44}$$

where $\vec{B}(\vec{r})$ is the magnetic field at position $\vec{r}$.

To accommodate later signal processing stages as well as detect a more effective signal, quadrature detection is often used, in which two orthogonal receiver coils detect signal yielding a complex signal

$$S(t) = S_1(t) + i\, S_2(t) \tag{2.45}$$

with one output being treated as the real part (x-axis) and the other the imaginary part (y-axis).

If we assume that there is a homogeneous magnetic field in the receiver coil, the signal can be expressed as follows [53]:

$$S(t) \propto \int_{object} M_{xy}(\vec{r}, 0) e^{i\omega(\vec{r})t}\, d\vec{r}, \tag{2.46}$$

where $\omega(\vec{r})$ is the frequency of the rotating frame. Assuming that the spatial density of hydrogen nuclei, $\rho(\vec{r})$ is proportional to the longitudinal magnetization at thermal equilibrium:

$$\rho(\vec{r}) \propto M_o(\vec{r}), \tag{2.47}$$

And the transverse magnetization after an $\frac{\pi}{2}$-pulse becomes

$$M_{xy}(\vec{r}, 0) \propto \rho(\vec{r}). \tag{2.48}$$

Then the signal is related to the spatial distribution of ^{1}H nuclei and their frequencies (using Equation (2.46)) and is expressed as

$$S(t) \propto \int \rho(\vec{r}) e^{-i\omega(\vec{r})t} d\vec{r}, \tag{2.49}$$

where this shows that $S(t)$ and $\rho(\vec{r})$ are Fourier transform pairs.

2.5 Free Induction Decay

As the transverse magnetization M_{xy} rotates at Larmor frequency after excitation from a RF-pulse, it induces a damped sinusoidal voltage known as the free induction decay (FID) as shown in Figure 2.13. The magnitude of this FID signal depends on the flip angle (Equation (2.36)), the total number of spins in the sample, as well as the strength of the magnetic field (Equation (2.14)). The signal decays as a result of the loss of phase coherence between the individual magnetic moments due to the inhomogeneity of the field, which is characterized by the T_2^* decay (described in Section (2.3)). The FID signal is expressed as

$$S(t) \propto \sin(\alpha) \int_{-\infty}^{\infty} \rho(\vec{r}) e^{-\frac{t}{T_2(\vec{r})}} e^{-i\omega(\vec{r})t} \, d\vec{r} \; ; \; t > 0 \,, \tag{2.50}$$

where $\rho(\vec{r})$ is the spectral density function which determines the characteristics of an FID signal. After a $\frac{\pi}{2}$-pulse, a homogeneous sample with a single resonant frequency ω_o, will reduce to

$$S(t) \propto M_o e^{-\frac{t}{T_2}} e^{-i\omega_o t} \; . \tag{2.51}$$

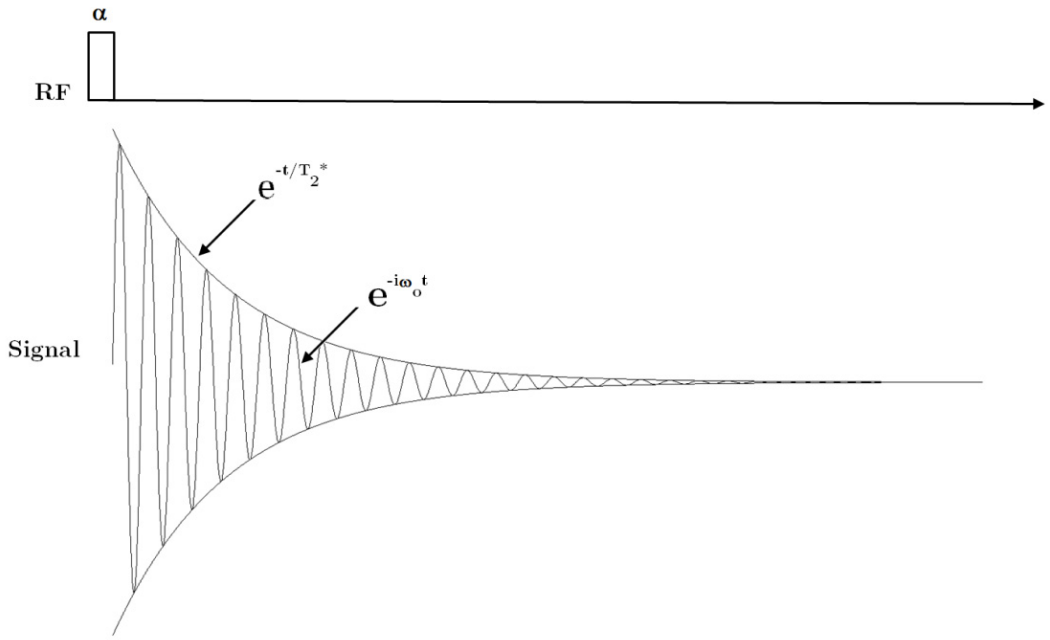

Figure 2.13: The FID signal after an α-pulse. Due to the local field inhomogeneities, the exponential decay is approximated by the time constant, T_2^* in the presence of local field inhomogeneities. In this figure, ω_o, is small for visual clarity.

2.6 Pulse Sequences

The spin density and relaxation constants T_1 and T_2 are all fundamental properties of tissues which can be exploited by MRI [53,58,59]. The T_1- and T_2- relaxation times are determined by the molecular structure of the tissues [59,60]. The type of structure of the molecules in the tissue influences how protons give off or absorb the energy into the surrounding molecular structure, as well determines how fast the magnetic moments in the tissue will dephase. Energy transfer occurs most efficiently when the natural motional frequencies (translation, rotation and vibration) ω, of the protons are at Larmor frequency, ω_o (Equation (2.4)). The natural motional frequency of hydrogen depends on the physical

state of the tissue, and is influenced by the atoms to which they are attached or are proximal. Atoms which are spaced further apart from one another produce higher natural motional frequencies and have less spin-spin interaction between the atoms which causes slower dephasing and therefore gives the tissue a long T_1 and long T_2. Alternatively, atoms which are spaced closer together have lower natural motional frequencies, and dephasing occurs more rapidly due to more spin-spin interaction, producing a short T_1 and short T_2.

Fluids, such as water (H_2O), have hydrogen protons that are spaced further apart from one another and produce natural motional frequencies much faster than the Larmor frequency for hydrogen, i.e. $\omega(H_2O) \gg \omega_o$, which results in a long T_1. Also this distance between the protons causes slower dephasing, which produces a long T_2. Solids, on the other hand have the opposite effect, as the molecular structure is very compact this creates greater spin-spin interaction causing dephasing to occur more rapidly, producing a short T_2. It also has lower natural motional frequencies which are slower than the Larmor frequency for hydrogen, $\omega(solids) < \omega_o$, which produces a short T_1. Intermediate molecules, such as fat, have natural motional frequencies that are close to the Larmor frequencies used for MRI, $\omega(fat) \approx \omega_o$, which produces short T_1 and T_2.

Creating pulse sequences that emphasize these differences in tissues aids in the contrast sensitivity of MR image. The two pulse sequences that will be discussed in this thesis are the spin echo and the gradient echo which are used to generate an echo. This echo is a

form of magnetic resonance signal that is produced from the refocusing of the transverse magnetization. The spin echo is an echo signal that is generated by multiple RF pulses, whereas a gradient echo is generated by magnetic field gradients.

The spin echo uses a RF excitation pulse that rotates the longitudinal magnetization (M_z) into the xy-plane, producing the maximal transverse magnetization (M_{xy}) which has the spins in phase coherence. Dephasing of the spins occurs and a FID signal emerges from this dephasing. In order to put the spins back into coherence, another RF pulse is applied along the transverse direction, inverting the phases of the spin system causing the spins to rephase, which produces the signal or 'echo'.

Unlike the spin echo, the gradient echo uses a pair of magnetic field gradients to induce the formation of an echo in lieu of a refocusing RF pulse. The gradient changes the local magnetic field which in turn causes the spins to precess at slightly higher or lower frequencies along the direction of the applied gradient. The formation of an echo is achieved by dephasing the spins with a negatively pulsed gradient before they are rephased by a gradient with opposite polarity to generate an echo.

Spin echoes and gradient echoes will be explained in Sections 2.6.1 and 2.7

2.6.1 Spin Echo

The spin echo pulse sequence is a commonly used sequence in MRI. An initial 90° RF-pulse is applied at time, t=0, which flips the spins into the xy-plane, producing the maximal transverse magnetization M_{xy} and places the spins in phase coherence as shown in Figure 2.14(a). The FID signal appears and exponentially decays with T_2^* relaxation due to the magnetic field inhomogeneity, in turn causing the spins to be out of phase. Typically this FID is ignored and each spin will acquire a different phase based on its surrounding magnetic field inhomogeneities, as shown in Figure 2.14(b).

After a time delay, τ, a 180° RF pulse (known as the *refocusing pulse*) is applied along a transverse direction such as $\hat{x}'$ which inverts the phases of the spin system, as shown in Figure 2.14(c). During the next time period, τ, the spins rephase. This 180°-pulse eliminates the dephasing that was caused by the T_2^* effect from the first RF pulse. The spins are rephased and produce a measureable signal at a time equal to the time of echo (TE), so named because of the "echo" signal (Figure 2.14(d)). The echo at time TE is at lower amplitude than the FID because of the T_2 relaxation.

Digital sampling and acquisition of the signal occurs, just before and after the peak amplitude of the echo (centred at the time TE). At a time TR, or repetition time, after the 90°-pulse, another 90°-pulse is applied, and the sequence repeated to acquire more signal, as shown in Figure 2.14.

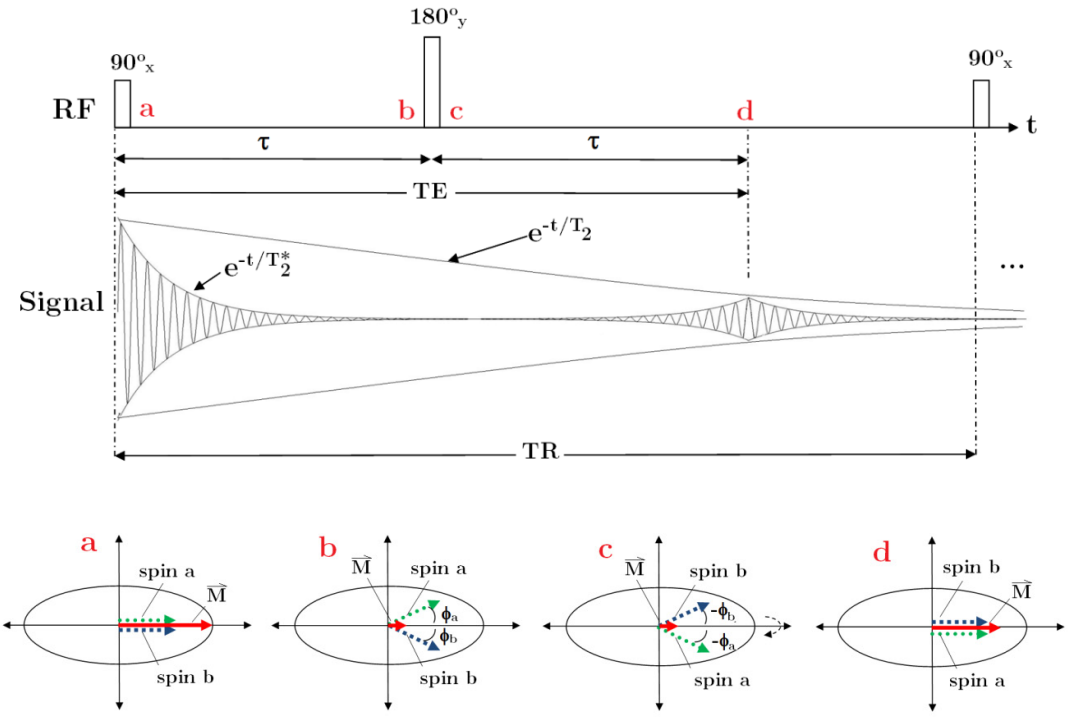

Figure 2.14: Spin echo sequence. After a 90°-pulse the 'spin a' will precess faster than $\vec{M}$ and 'spin b' will precess slower than $\vec{M}$ which results in a T_2^* decay (shown in part b). At $t = \tau$, a 180°-pulse flips the spins in the opposite planes (shown in part c), which causes both the 'spin a' and 'spin b' precess towards $\vec{M}$, resulting in a growth in T_2^*. The spins rephase at $t = 2\tau = TE$ with a signal amplitude weighted by the T_2 constant (shown in part d). The magnitude $\vec{M}$ at this stage is much smaller than it was prior to the 90°-pulse.

Typically a few dummy scans (or pulse sequences where signals were not acquired) are used to get the system in a form of steady state before signal is acquired. For spin echo sequences, the parameters of interest are TR and TE. It can be shown that the signal in the spin echo sequence is given by [61]

$$S(t) \propto M_{xy}(t) = M_{xy}(0)\left\{1 - 2 \cdot e^{\left[\frac{-\left(TR-\frac{TE}{2}\right)}{T_1}\right]} + e^{-\left(\frac{TR}{T_1}\right)}\right\} \times e^{\frac{-TE}{T_2}}. \qquad (2.52)$$

From Equation (2.52), it is shown that TE influences the T_2-weighting of the image, and TR influences the T_1-weighting of the image. The effects of TE and TR on image contrast are summarized in Table 2.3 and will be derived in Sections 2.6.2 - 2.6.4.

Table 2.3: The effect of TR and TE for a spin echo image.

	TE short	TE long
TR short	T_1-weighted	Not used
TR long	PD-weighted	T_2-weighted

2.6.2 T_1-Weighting

A T_1-weighted sequence is designed to produce contrast in an image based on the T_1 characteristics of tissues and the de-emphasizing of T_2 contributions [60]. To achieve T_1-weighting using a spin echo sequence as shown in Figure 2.14, a short TE is used to minimize the T_2 dependency during signal acquisition; this short TE also preserves the T_1 signal differences with minimal transverse decay. From Equation (2.52), a short TE in a spin echo sequence, will cause $\exp\left(\frac{TE}{T_2}\right) \approx 1$ so that the signal is dependent on T_1 and not T_2 and therefore giving the signal

$$S(t) = M_o\left[1 - e^{-\left(\frac{TR}{T_1}\right)}\right]. \tag{2.53}$$

In a T_1-weighted image of the brain at 7T, fat is the most intense signal, at shortest T_1; white and grey matter have intermediate intensities, at intermediate T_1 values; and

cerebrospinal fluid (CSF), has the lowest intensity signal, at longest T_1. Rooney et al. [62] measured T_1 value of CSF to be at 4425±137 ms. Guilfoyle et al. [63] measured T_1 values for white and grey matter, with 1503±56 ms for white matter (corpus callosum), and 1632±52 /1767±70 ms for grey matter (retrosplenial granular cortex/hippocampus, respectively). Ren et al. [64] measured T_1 values for fat in the range of 320±0.05 to 1160±0.04 ms in human subcutaneous tissue and tibial marrow. The choice of TR is based on the desired image contrast. For example, if the desire is to have CSF and brain tissue to have the largest contrast, then a TR value between the T_1 values of CSF and brain should be chosen.

2.6.3 T_2-Weighting

To minimize the T_1 differences in the tissues, and accentuate the T_2 differences in a spin echo image [60] (Figure 2.14), a relatively long TR is used. This allows for a significant longitudinal recovery so that the transverse magnetization differences are those mainly resulting from variations in the T_2 values of tissues with a long TR. By using a long TR, Equation (2.52) reduces to

$$S(t) = M_o e^{-\left(\frac{TE}{T_2}\right)}. \tag{2.54}$$

A T_2-weighted signal from the spin echo sequence is the second echo (produced by the 180° pulse) of a long TR spin echo pulse sequence. In T_2-weighted images of the brain at 7T, CSF appears brightest at the longest T_2, than fat which the shortest T_2. Grey and white matter have intermediate T_2 values, with grey matter having a larger T_2 than white matter. Crémillieux, et al. [65] measured T_2 values of CSF and fat with values of 125.1±9.2 ms and 27.4±1.3 ms, respectively. Guilfoyle et al. [63], measured T_2 values of grey and white matter, with 41±3/38±2 ms for grey matter (hippocampus/cortex), and 37±2 ms for white matter (corpus callosum). The value of TE is chosen to optimize differences between tissue types. For example, if the desire is to have the largest contrast between fat and brain tissue, then a TE value between the T_2 values of fat and brain should be chosen.

2.6.4 Proton Density Weighting

Proton density (PD) weighted images minimize both the T_1 and T_2 characteristics, by producing a short TE and a long TR in a spin echo [59,60]. The contrast provided in the images arises from primarily the density of the protons that is being imaged in a volume. The signal on the PD-weighted image is brighter with a higher number of protons in a given unit of tissue, as this then produces a greater transverse magnetization. Conversely, having a lower number of protons in a given unit of tissue produces less transverse magnetization and thus produces a darker the signal on the PD image.

2.7 Gradients

Signals produced by a spin echo sequence as described above do not provide any spatial information. To provide this spatial information and thus create an image, gradient coils are used to produce another set of magnetic fields that can alter the B_o field. This causes the magnetic field strengths to vary linearly with position along a particular axis in order to make the Larmor frequency depend on position within the magnet. The application of gradient fields for spatial localization in MRI was first outlined by Lauterbur in 1973 [66].

The gradient field $\overrightarrow{B_G}$ is a linear, position dependent, inhomogeneous field whose z-component varies linearly along a specific direction, causing the protons to alter their precessional frequency corresponding to their position along the applied gradient field in a known and predictable way. The gradient system consists of the three gradient coils, referred to as the x-, y- and z-gradient coils which would ideally produce their respective gradient fields. These gradients are

$$\begin{aligned} G_x &= \frac{\partial B_{G,z}}{\partial x}\ , \\ G_y &= \frac{\partial B_{G,z}}{\partial y}\ , \\ G_z &= \frac{\partial B_{G,z}}{\partial z}\ . \end{aligned} \tag{2.55}$$

It is important to note that for each case, the magnetic field produced by the gradient coil has components in the x-direction $(B_{G,x})$ and y-direction $(B_{G,y})$, but these components are ignored because the B_o field is very strong in the z-direction, and therefore $B_{G,z}$ is often used interchangeably with B_G.

The total magnetic field in the presence of a gradient field is given by

$$\vec{B}_z = \left(B_o + B_{G,z}\right)\hat{z} \ , \tag{2.56}$$

and in the case where all three gradient coils are turned on simultaneously, the total gradient field is given by

$$B_{G,z} = G_x x + G_y y + G_z z \ . \tag{2.57}$$

Alternatively, these gradient coils can be turned on individually as in the Equations (2.55).

The three gradients are grouped into a gradient vector:

$$\vec{G} = \left(G_x, G_y, G_z\right) = G_x\hat{x} + G_y\hat{y} + G_z\hat{z} \tag{2.58}$$

The direction of $\vec{G}$ is called the *gradient direction* of $\vec{B}_{G,z}$ (or $\overrightarrow{B_G}$). Because the gradient is linear and position-dependent magnetic field, it can be written as

$$\vec{B}_z = \vec{G} \cdot \vec{r} \tag{2.59}$$

In MRI the most common approach to generate a single slice or 2D image is to only excite protons lying in the desired image plane, as shown in Figure (2.15). This is done with a magnetic gradient and a shaped RF pulse. Figure 2.15 shows there are three cases where slice selection excites slices along the x-, y-, and z-axes and the corresponding slice equations are given, respectively, by

$$
\begin{aligned}
|x - x_o| &\leq \frac{\Delta x}{2}, \\
|y - y_o| &\leq \frac{\Delta}{2}, \\
|z - z_o| &\leq \frac{\Delta z}{2}.
\end{aligned}
\tag{5.60}
$$

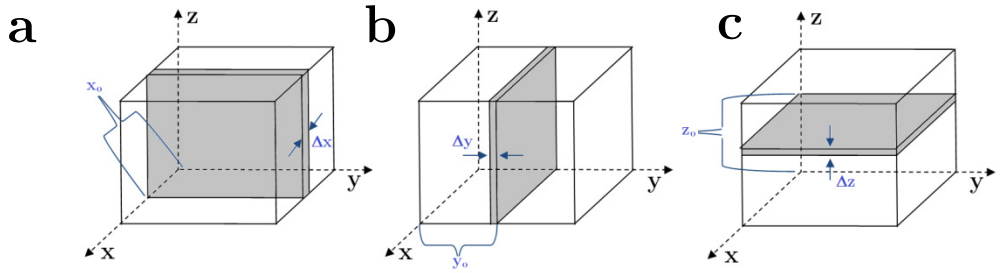

Figure 2.15: Parameters characterizing a slice in the special case where the image is perpendicular to the (a) x-axis, (b) y-axis, and (c) z-axis. The slice equations are given respectively in Equation (5.60). (modified from [53])

2.7.1 Slice Selective Gradients

Slice selective gradients make the resonant frequency dependent on position by specifically varying linearly along the slice select direction ($\vec{\mu}_s$). For simplicity and by convention, the slice selection direction will be taken as the z-direction. To excite a slice along the z-axis during an RF pulse, a linear gradient field needs to be applied along the z-axis

$$
\overrightarrow{G_{ss}} = (0,0,G_z) = G_z\hat{z}\ . \tag{2.61}
$$

This RF pulse is called a slice selective RF pulse. This changes the varying Larmor frequency of the spins so that it varies linearly with position along the z-axis:

$$
\omega(z) = \omega_o + \gamma G_z z \tag{2.62}
$$

or $$f(z) = f_o + \bar{\gamma} G_z z \tag{2.63}$$

Ideally, a rectangular slice profile is desired in the image plane. In the frequency domain, the sinc RF pulse (Equation (2.28)), after a Fourier transform yields a rectangular pulse

$$p(f) = \prod \left(\frac{f - f_c}{\Delta f} \right) e^{i2\pi(f - f_c)\tau_p/2} \tag{2.64}$$

where $\prod \left(\frac{f - f_c}{\Delta f} \right)$ is the boxcar function, with a frequency bandwidth, Δf centred on the Larmor frequency, f_c. The frequency bandwidth Δf determines the slice thickness, and f_c determines the slice selection, defined as follows:

$$\Delta f = \bar{\gamma} G_z \Delta z, \tag{2.65}$$

$$f_c = f_o + \bar{\gamma} G_z z_o \tag{2.66}$$

Equation (2.64) can be rewritten with Equations (2.65) and (2.66) to be defined along the z-direction, with a slice of thickness Δz that is centred at $z = z_o$:

$$p_s(z) = \prod \left(\frac{z - z_o}{\Delta z} \right) e^{i\gamma G_z (z - z_o)\tau_p/2} \tag{2.67}$$

Using these equations, changing the bandwidth (Figure 2.16) or the gradient strength (Figure 2.17) can adjust the slice thickness. For example, we can decrease the slice thickness by decreasing the bandwidth or increasing the gradient strength. And increasing the slice thickness can be done by increasing the bandwidth or decreasing the gradient strength. With a chosen slice width, changing the gradient strength changes the bandwidth (Figure 2.18).

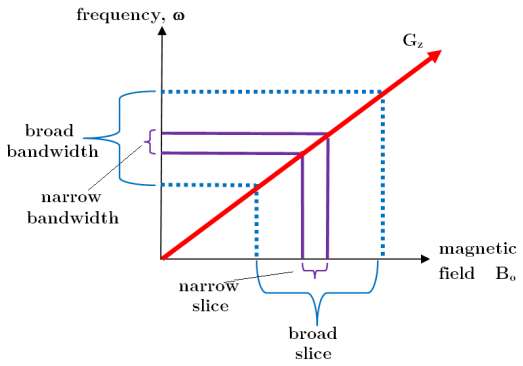

Figure 2.16: For a given gradient field strength: an RF pulse with a narrow bandwidth excites protons over a narrower slice of tissue, and a broad bandwidth excites a thicker slice.

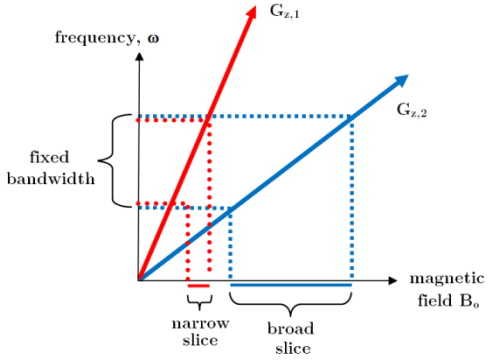

Figure 2.17: For a fixed bandwidth, the magnitude of the gradient strength (slope) determines the slice thickness. Decreasing the gradient strength ($G_{z,2}$) results in a wider slice thickness.

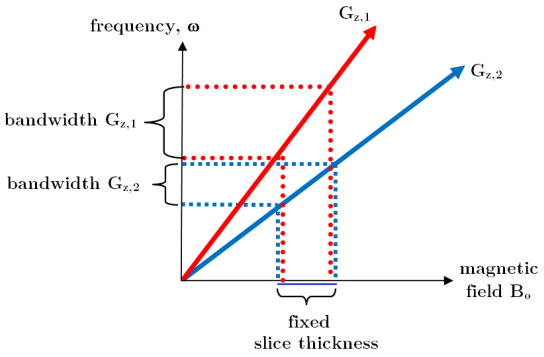

Figure 2.18: For a fixed slice thickness, the magnitude of the gradient strength (slope) increases with an increased bandwidth. The larger gradient strength, $G_{z,1}$ produces an increased bandwidth, when compared to the bandwidth of $G_{z,2}$ at a lower gradient strength.

After a slice select 90°-pulse and gradient, the phases of the spins will depend on position because their frequency depends on position; this is given in the equation below in the rotating frame:

$$\omega = \gamma G_z z \tag{2.68}$$

The slice selective gradient pulse duration is the same as the 90°-pulse duration, t_{90}. During half this time, as shown in Figure 2.19, the spins acquire a phase dependent on positions, according to

$$\Delta\phi = \omega\Delta t = \gamma G_z z \cdot \frac{t_{90}}{2} \,. \tag{2.69}$$

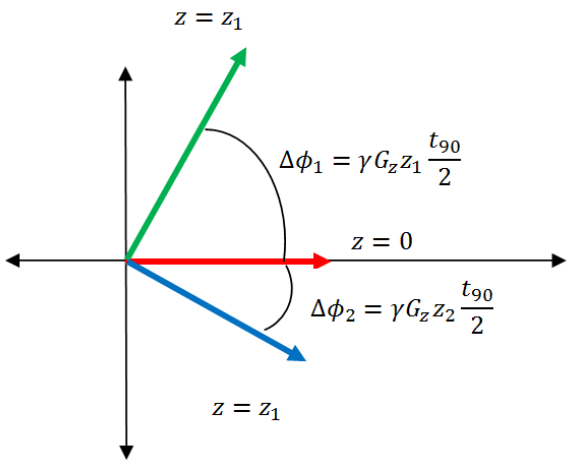

Figure 2.19: The slice selective gradient pulse, during half the time of the 90°-pulse duration, the spins acquire a phase that is dependent on positions. In this figure, $z_1 > 0 > z_2,\ \Delta\phi_1 > 0 > \Delta\phi_2$.

To regain phase coherence, a slice refocusing gradient is added after the completion of the RF pulse as shown in Figure (2.20). The gradient has opposite sign, and its duration is

half that of the slice select gradient. Thus the phase added during the refocusing pulse is given as

$$\Delta\phi = \omega\Delta t = -\gamma G_z z \cdot \frac{t_{90}}{2}\,, \tag{2.70}$$

and therefore the net phase is given by the Equations (2.69) and (2.70) is zero.

In summary, the slice select gradient applied during RF pulse results in a proton excitation in a single phase, localizing the signal in the dimension orthogonal to the gradient. It is the first of the three gradients applied to the volume in question to create an image.

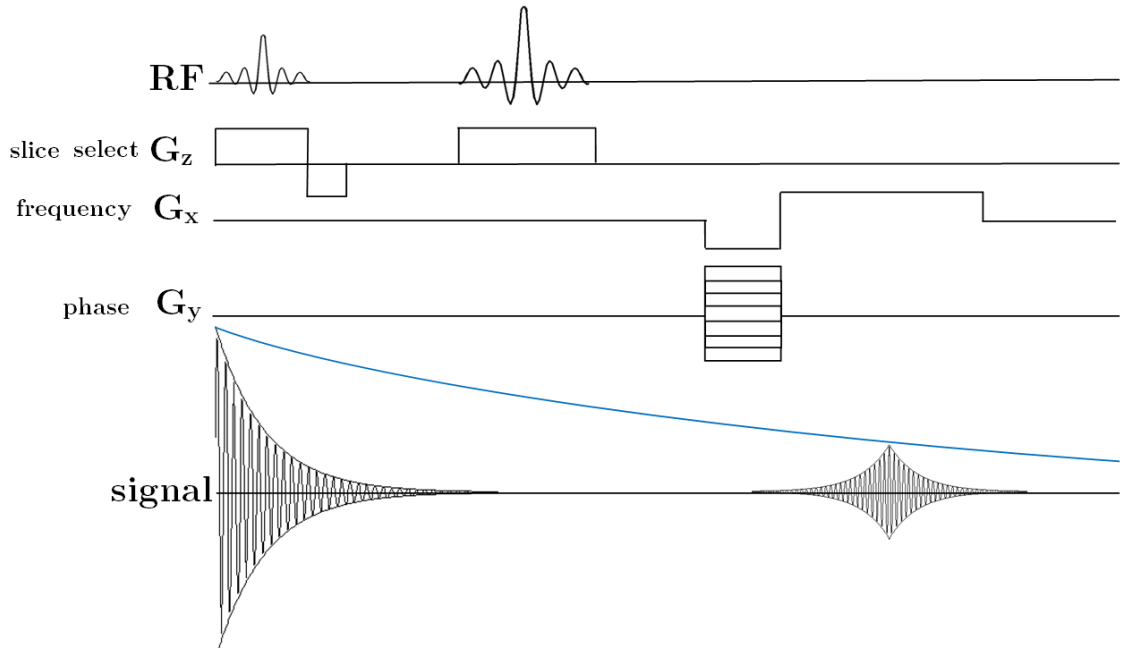

Figure 2.20: Image gradients for slice select, frequency-encoding and phase-encoding. The slice selective gradient pulse for the 180°-pulse refocuses itself.

2.7.2 Phase Encoding Gradients

The phase encoding gradient is applied between the 90° and 180° pulses, or after the 180-pulse before the echo. It shifts the frequency of the spins for a time, T_{PE}, so that the phase acquired in this time depends on position. For simplicity, if we assume the phase encoding is in the y -direction, spins at different y -positions accumulate different phase angles after a time interval, T_{PE}. Therefore, the signal collected afterward will have an initial phase angle given by

$$\phi(y) = (\omega_o + \gamma G_y y)T_{PE} \,, \tag{2.71}$$

$$\phi(y') = -\gamma G_{y'} y' \, T_{PE} \tag{2.72}$$

where $G_y y$ is the phase encoding gradient, and Equations (2.71) and (2.72) represent the phase in the laboratory frame and rotating frame respectively. Because $\phi(y)$ is linearly related to the signal location y, the signal is phase encoded. The received signal is the sum of all local phase encoded signals:

$$S(t) = \int_{object} dS(\vec{r}, t) = \left[\int_{object} \rho(y) e^{-i\gamma G_{PE} \cdot y \cdot T_{PE}} \, d\vec{r}\right] \cdot e^{-i\omega_o t} \tag{2.73}$$

where the carrier signal ($e^{-i\omega_o t}$) is removed after demodulation. Thus phase encoding is done by pre-frequency encoding the signal for a short time interval. Based on the equation above, this signal has the form of a non-encoded signal with a position-dependent initial phase angle, which can be adjusted with a variable phase encoding gradient strength or phase encoding interval.

2.7.3 Frequency Encoding Gradients

After the magnetic moments have been excited by a slice selective RF pulse, spatial information can be encoded into the signal during the free procession period. A gradient called the frequency encoding gradient (or readout gradient), is applied in one of the in-plane directions perpendicular to the slice gradient direction. By convention, and for ease of explanation, the frequency encoding direction will be taken as x -direction. This makes the oscillation frequency of the MR signal linearly dependent on its x –position, and it can be throughout the formation and decay of the spin echo signals as shown in Figure (2.20).

Consider an idealized one-dimensional object with spin distribution $p(x)$, if the magnetic field that the object experiences after an excitation is

$$B(x) = B_o + G_x x\,, \tag{2.74}$$

then the Larmor frequency at position x is

$$\omega(x) = \omega_o + \gamma G_x x\,. \tag{2.75}$$

As a result, he FID signal generated locally from the spins is

$$dS(x,t) = \rho(x)dx \cdot e^{-i\gamma(B_o+G_x x)t} \tag{2.76}$$

This signal is frequency encoded because its oscillation frequency $\omega(x) = \gamma(B_o + G_x x)$ is linearly related to spatial location, where G_x is the frequency encoding gradient. The signal received from the object in the presence of the gradient is

$$S(t) = \int_{object} dS(x,t) \propto \left[\int_{-\infty}^{\infty} \rho(x) e^{-i\gamma G_x x t} dx \right] e^{-i\omega_o t} \quad . \tag{2.77}$$

After demodulation, or the removal of the carrier signal $e^{-i\omega_o t}$, the signal is reduced to

$$S(t) = \int_{-\infty}^{\infty} \rho(x) e^{-i\gamma G_x x t} dx \quad . \tag{2.78}$$

The frequency encoding gradient field causes the magnetic moments to lose phase coherence because each spin has a different frequency based on position. The gradient is applied for a given time T_{FE}, thus the phase acquired by a given spin at position x during this time is

$$\phi(x) = (\omega_o + \gamma G_x x) T_{FE} \tag{2.79}$$

$$\phi(x') = -\gamma G_{x'} x' T_{FE} \tag{2.80}$$

where Equation (2.78) and (2.79) are in the laboratory frame and rotating frame respectively.

To make the net phase zero at the centre of the frequency encoding gradient, i.e. $t = \frac{T_{FE}}{2}$ when the echo is produced, a read dephaser pulse is typically added before the readout pulse, and this pulse has half the duration and negative amplitude of the frequency encoding pulse (see Figure 2.20). This also means that the line of k-space is collected from $-k_{max}$ to $+k_{max}$.

2.8 k-space Data Acquisition and Image Reconstruction

In 1983 Ljunggenen [67] and Tweig [68] independently introduced k-space formalism. They showed that the demodulated MR signal $S(t)$ generated by freely precessing nuclear spins in the presence of a linear magnetic field gradient $\vec{G}$ equals the Fourier Transform of the effective spin density.

In the rotating frame, the Larmor frequency can be written as a function of position vector $\vec{r}$ and the gradient vector $\vec{G}$ (Equation (2.58)):

$$\omega(\vec{r}) = \vec{G} \cdot \vec{r} \tag{2.81}$$

Using Equation (2.49), this produces the signal in the form of a Fourier transform

$$S(t) \propto \int \rho(\vec{r}) e^{-i\gamma G_{PE} \cdot \vec{r} t} d\vec{r} \tag{2.82}$$

A reciprocal space vector can be defined as

$$\vec{k} = \frac{\gamma \vec{G} t}{2\pi} \tag{2.83}$$

Using this definition of $\vec{k}$, the signal can be rewritten as

$$S(\vec{k}) \propto \int \rho(\vec{r}) e^{-i2\pi \vec{k} \cdot \vec{r}} d\vec{r} \tag{2.84}$$

where $\rho(\vec{r})$ and $S(\vec{k})$ are Fourier Transform pairs and therefore can be written as

$$\rho(\vec{r}) \propto \int S(\vec{k}) e^{-i2\pi \vec{k} \cdot \vec{r}} d\vec{k}. \tag{2.85}$$

The signal $S(\vec{k})$ detected in the domain of the Fourier transform into the spatial domain function, $\rho(\vec{r})$. In 2-dimensions [53], $\rho(\vec{r})$ become $\rho(x, y)$ and $S(\vec{k})$ and is expressed as

$$S(k_x, k_y) \propto \iint_{-\infty}^{\infty} \rho(x,y) e^{-2\pi(k_x x + k_y y)}\, dxdy \tag{2.86}$$

where $k_x,\ k_y$ are defined in Equation (2.87). The reciprocal space or k-space can be transversed by varying $\vec{G}$ or t with the direction of the transverse set by the sign of $\vec{G}$.

Prior to image reconstruction for 2D planar imaging, the raw data acquired from the pulse sequences are stored in a 2-dimensional matrix called the k-space matrix, with k defined in Equation (2.83). Continuing with the previous convention, the x-direction is taken as the frequency encoding direction, and y-direction as the phase encoding direction. The z-direction is the slice direction with this definition the components of the vector k can be written as the equations:

$$k_x = \frac{\gamma}{2\pi} G_x t \quad \text{and} \quad k_y = \frac{\gamma}{2\pi} G_y t \tag{2.87}$$

The data acquired at different phase and frequency values are placed into the matrix in a location based on k-values. A line of data in k-space is directly related to the gradient across the object being imaged. When the frequency encoding gradient is switched on during acquisition, a series of points are acquired corresponding to the various frequencies present at a particular phase value k_y and slice position, z, creating a horizontal line of voxels in k-space along the k_x-axis. As the values of k_y change, the k-space data populates the matrix k_x-line by k_x-line. Every point in k-space contains part of the information for the complete image.

Figure 2.21 shows how the lines of data in k-space are related to the gradients. In this simple spin echo pulse sequence, the phase-encoding and frequency dephaser gradients are

switched on at the same time. The frequency dephaser gradient (Figure 2.21(i))is in the negative direction and therefore moves the k_x value to the left of centre. The first phase gradient is applied at the maximum negative value so that it moves to the lowest k_y value (Figure 2.21(a)). This is followed the frequency-encoding gradient (Figure 2.21(ii)) with twice the area as the frequency dephaser gradient (Figure 2.21(i)) and in the positive direction. This causes a gradient echo to occur which samples a line of k-space. A crusher gradient is then used to eliminate any unwanted signal (such as from the FID) before the next acquisition occurs. For each line of k-space, the phase-encoding gradient increases by Δk_y and this is sequence is repeated until all lines of k-space are acquired (Figure 2.21(b-d)).

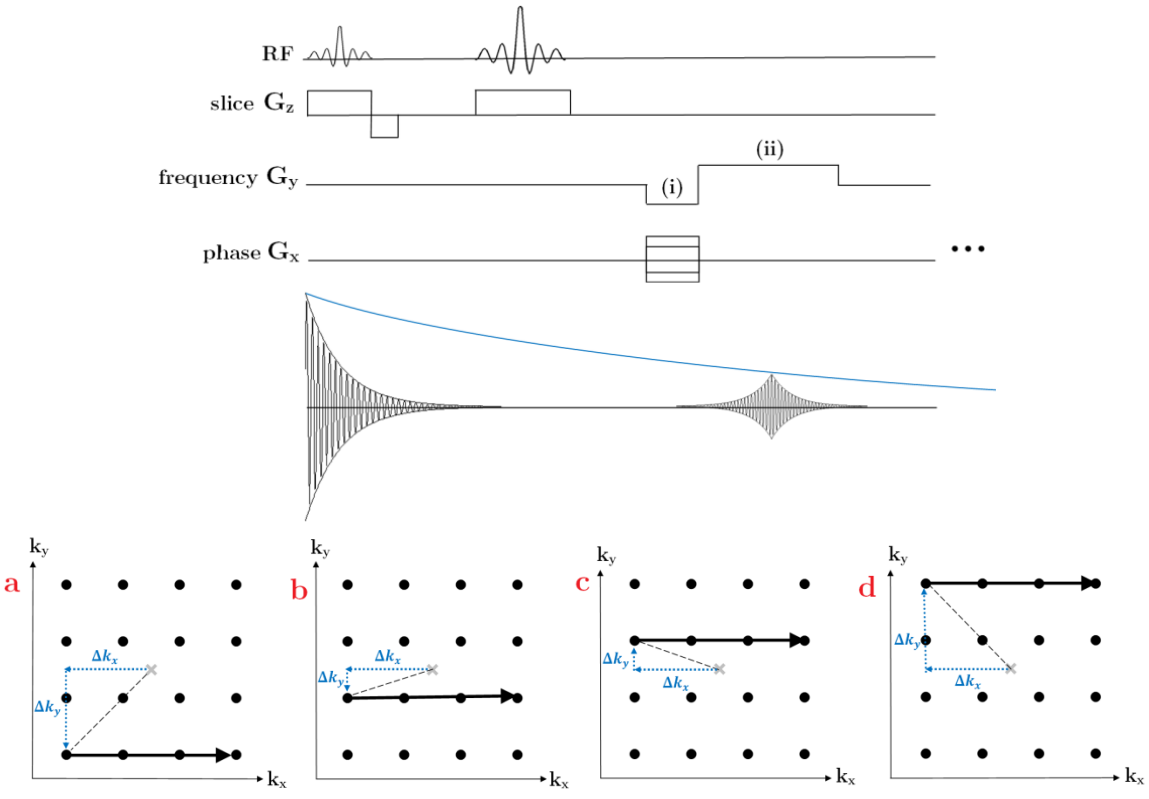

Figure 2.21: Shows how the lines of data in k-space are related to the gradients

In k-space, the outer rows of the matrix correspond to the higher spatial frequencies, which provide information regarding the borders and contours of the image, whereas the lower spatial frequencies are found closer to the centre of the matrix, and represent the general contrast of the image. For a choice of field of view (FOV), the read and phase gradient strength and pulse times are defined by the following relationships [60,69,70]:

$$\text{and} \quad \begin{aligned} FOV_x &= \frac{1}{\Delta k_x} = \frac{2\pi}{\gamma G_x \Delta t}, \\ FOV_y &= \frac{1}{\Delta k_y} = \frac{2\pi}{\gamma G_y \Delta t}. \end{aligned} \tag{2.88}$$

The maximum value of k, or equivalently, the number of phase and frequency encoding steps sampled determines the resolution:

$$\text{Resolution}_x = \Delta x = \frac{1}{|k_{x_{max}}|} = \frac{1}{N_x \Delta k_x} \tag{2.89}$$

$$\text{Resolution}_y = \Delta y = \frac{1}{|k_{y_{max}}|} = \frac{1}{N_y \Delta k_y} \tag{2.90}$$

The proton density $\rho(\vec{r})$, weighted by T_1, T_2, can be mapped by measuring the NMR signal, $S(\vec{k})$, over all k-space and taking the Fourier transform. In other words, as time progresses the signal traces out a trajectory in k-space so that the $S(\vec{k})$ can be measured. The spin density $\rho(\vec{r})$ weighted for the effects of T_1 preparation, T_2 decay, dephasing due to field inhomogeneity, etc, and any other phenomena that affect the amount of transverse magnetization available to induce signal in the RF pulse can be calculated from the Fourier transform of $S(\vec{k})$ to make an image.

2.9 Magnetic Resonance Spectroscopy

Magnetic resonance spectroscopy (MRS), like MRI, requires a magnetic field and RF pulses that are applied at a particular frequency to observe the signal of specific nuclei in the region of interest. The application of these pulses produces a spectrum of peaks with a frequency axis measured in parts per million (ppm) whose relative area measures the relative concentration of the metabolite being observed (Figure 2.22).

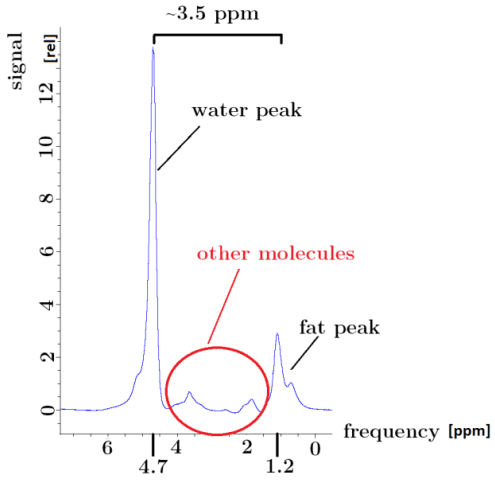

Figure 2.22: Spectra of lipid and water. Peaks correspond to different metabolites, identified primarily by their frequencies. This frequency is expressed as a frequency shift relative to a reference frequency, this shows H_2O at ~4.7 parts per million (ppm), so it is referenced to a free ^1H, and the fat peak at ~1.2 ppm.

Each metabolite is found on a specific position along the frequency axis (x-axis), and has a characteristic signature determined by the type of configuration of the protons and electrons and their chemical bonds. How these different frequencies arise is described in Section 2.9.1. The peak amplitude (or area) and line width (or spectral resolution) is

directly related to the concentration the metabolite and is displaced along the y-axis. The width of the peak, describes the mobility of the molecules, where small unbound molecules give rise to very sharp peaks, whereas, immobilized small molecules produce broader peaks. The y-axis has no absolute scale, and therefore a ratio is needed in order to find an objective quantification of the concentration of the metabolite in question.

2.9.1 Chemical Shift

Chemical shift mathematically explains how the chemical bonds in a compound result in a change in the resonance frequency of the nuclei within the molecules. In these chemical bonds, the current generated from the electrons orbiting around the nucleus induce their own weak magnetic field which then alters the B_o magnetic field that the nucleus would normally experience. The magnetic field experienced by a nucleus is expressed as follows:

$$\hat{B}_o = B_o(1 - \sigma), \tag{2.91}$$

where σ is the shielding constant which takes on either a positive or a negative value. Based on the Larmor relationship (Equation (2.4)), the resonance frequency for the nucleus is given as

$$\widehat{\omega}_o = \omega_o - \Delta\omega = \omega_o(1 - \sigma). \tag{2.92}$$

This equation indicates that spins in different chemical environments will have shield shifts in their resonance frequencies when B_o is perfectly homogeneous. The frequency shift $\Delta\omega$, is dependent on both the strength of the external field B_o and the shielding constant σ. The value of the shielding constant is very small (on the order of ppm) and is dependent on the local chemical environment in which the nucleus is situated.

To remove the dependence on the chemical shift on the magnetic field strength, the chemical shift is usually expressed in parts per million, relative to a standard measured along with the sample and is defined as

$$ppm = \frac{(\nu_r - \nu_s)}{\nu_s} \times 10^6 \tag{2.93}$$

where ν_r is the resonance frequency of interest (or the resonant frequency of chemical compound being measured), and ν_s is the standard or reference resonance frequency (for ^{1}H spectroscopy, this is usually H_2O, or a free ^{1}H nucleus). The ppm scale describes the resonance frequency of a chemical. The positions of resonance peaks are measured relative to the standard. A standard metabolite is chosen that is also a compound present in the sample as it will also experience the magnetic environment that should be identical to that of the other substances giving rise to signals.

2.9.2 Chemical Shift Artefacts in Imaging

The Larmor frequency of fat protons is different to that of water by 3.5 ppm. Because of this difference, fat and water protons that are located in the same spatial position during the imaging process will be shifted from each other in the frequency-encode direction, as can been seen in Figure 2.23.

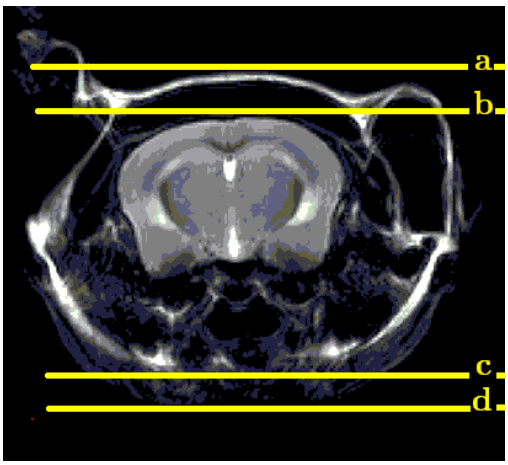

Figure 2.23: MR Image of a mouse brain without fat suppression, the fat shift is observed (highlighted in blue). The following areas are labeled as: (a) top edge of fat in the head, (b) top edge of head, (c) bottom edge of fat in the head, (d) bottom edge of muscles of the head.

Water is located at 4.7 ppm from a free ^{1}H, and fat is 1.2 ppm from a free ^{1}H. Therefore the fat shift relative to water is at 3.5 ppm. The chemical shift of fat, ω_f, at 7T (or $\omega_o = 300$ MHz (Larmor frequency)) at 3.5 ppm is $\omega_f = (3.5 \times 10^{-6}) \cdot \omega_o = 1050$ Hz. Therefore, at 7T (300MHz) protons in fat will have a resonant frequency approximately 1050 Hz higher than protons in water.

Given a frequency encoding bandwidth of 20,000 Hz, and the frequency matrix of 256 pixels, the frequency range per pixel would be $\Delta\omega = \frac{20000}{256} = 78.125 \frac{Hz}{pixels}$. From this, the expected number of pixels for fat shift is $\frac{\omega_f}{\Delta\omega} = \frac{1050}{78.125} = 13.44$ pixels. To represent this graphically (Figure 2.24), changing the frequency matrix to 16 pixels, gives the change in frequency/pixel as $\Delta\omega = \frac{20,000}{16} = 1250 \frac{Hz}{pixels}$. This in turn gives the expected number of pixels for fat shift to be: $\frac{\omega_f}{\Delta\omega} = \frac{1050}{1250} = 0.84 \approx 1$ pixel.

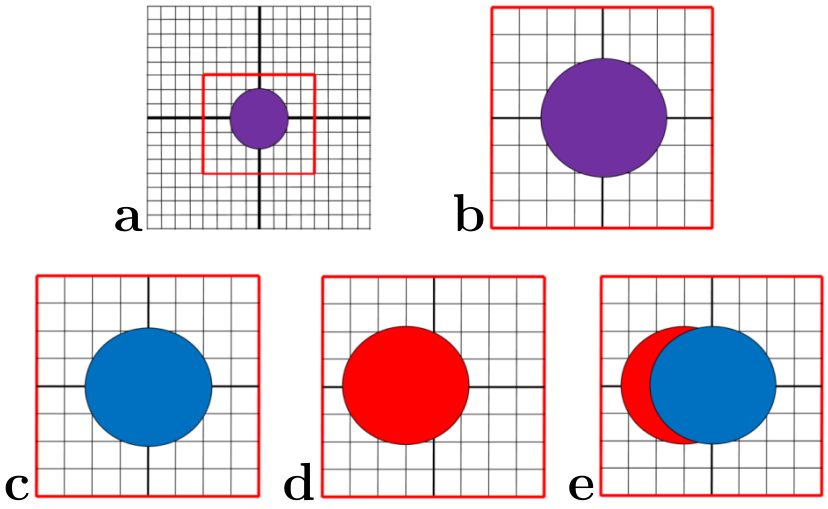

Figure 2.24 : Chemical shift in imaging. (a) original image at 16 × 16 matrix, (b) original image zoomed in at area indicated by red box, (c) image of water only, (d) image of fat only, (e) chemical shift of fat of 1 pixel from water.

2.9.3 Requirements for MRS

MRS can use the same apparatus as MRI, therefore for good quality spectra, the following properties are required [71]:

(1) *A strong and homogeneous magnetic field.* A heterogeneous magnetic field affects the spectral peak sharpness or line width which causes a dispersion of resonance frequencies. This causes the peaks to spread out or disappear into background noise. To create a more homogenous magnetic field, the magnetic field can be optimized over the sampled volume that is being measured by 'shimming' or the process of adjusting the DC currents in the shim coils.

(2) *Large or high signal-to-noise ratio (SNR).* The height of the peak in relation to background noise determines SNR. The quality of spectra can be improved with a high SNR, therefore SNR can be increased by also increasing the number of acquisitions (this is because SNR is proportional to the square root of the number of acquisitions). SNR can also be increased by increasing the region of interest (ROI) because more signal can be obtained with a larger sample, however this in turn sacrifices the spatial resolution which makes the ability to determine the presence of chemicals more difficult. Therefore there must be a balance between the sizes of the ROI and the SNR.

(3) *Specific sequences for spectroscopic signal resolution.* Sequences designed for spectroscopy are made to optimize the signal, spatial resolution and peak width. One type of sequence is single-voxel-spectroscopy which only receives the spectrum from a single

voxel. This type of sequence is a localization technique that involves three orthogonal slice selective gradients (x-, y- and z-axis) that are applied to select a single voxel for sampling, and generates a cubic or rectangular volume of the sample. Examples of this type of sequence are the point resolved spectroscopy (PRESS) and the stimulated echo acquisition mode (STEAM)[72,73] (which is described in Section 10.2.1).

(4) *Selecting appropriate parameters for the acquisition of MR spectra.* Factors such as T_1 and T_2 effects, spectral resolution and coil sensitivity, can make the interpretation of the data difficult. T_1 and T_2 relaxation times can affect how accurate the peak areas define the amount of metabolite concentration. To allow for the differentiation of spectral tissues, a sufficient amount of spectral resolution is needed. Spectral resolution is determined by line width, and therefore increasing line width corresponds to a reduced spectral resolution which in turn increases the overlap between the peaks with less different features

(5) *Water suppression.* The signal from water is dominant in a spectrum, this is because the concentration of water is greater than the rest of the other metabolites. Because water is the dominant peak, visualizing metabolites of interest makes it difficult because the water peak overlaps with the adjacent and much smaller peaks from other chemicals. In order to remedy this, water suppression is needed, and can be done by applying a bandwidth filter, and allows the residual signal of the other metabolites to be more readily detected. Limitations to this water suppression exists, because it does not only suppress

the signal from the water, but it also suppresses the signals from the other metabolites in question. One example of a sequence used for suppression is the Chemical Shift Selective (CHESS) pulse sequence [74,75]. This technique uses a frequency-selective 90^{o} RF pulse to selectively excite the unwanted signal that is to be suppressed (such as water). It is then followed by a spoiler gradient that dephases the resulting magnetization. The bandwidth of the RF pulses is narrow and centred on the resonance frequency of the water peak to saturate its signal and preserve the signal from the other metabolites being measured.

2.9.4 MRS in the Liver

^{1}H MRS has been shown to be effective for quantifying liver fat [73,76]. The fat or lipid (triglyceride) spectrum consists of multiple peaks. In the liver, the dominant lipid peaks are caused by the resonance of methyl (CH_3)- and methylene (~CH_2)-protons in the triglyceride molecule found respectively at 0.9 - 1.1 ppm and 1.3-1.6 ppm along the frequency domain. The size of the lipid peaks relative to that of water increases with the amount of fat molecules within a voxel. Measurement of the total lipids commonly includes only the peaks attributed to CH_2 and CH_3, because the peak attributed to CH (5.3 ppm) overlaps with the water peak. The ratio of the total lipid peak area to the water peak area is calculated by using total lipid measurement from the suppressed water sequence and the water measurement from the unsuppressed water sequence.

2.10 Pulse Sequences Used For This Project

The two main pulse sequences used in this project were STEAM and rapid acquisition with relaxation enhancement (RARE). STEAM was used to acquire spectra for the percentage of fat contained in the excised livers. RARE was used to acquire T_2-weighted brain images for both *in vivo* and *ex vivo* experiments. The pulse sequences will be described in Sections 2.10.1 and 2.10.2.

2.10.1 Stimulated Echo Acquisition Mode (STEAM)

STEAM is a localization technique that is commonly used for voxel selection. In STEAM, three orthogonal slice-selective 90° pulses are applied to the sample being measured. Only spins that experience all three 90°-pulses will be the ones that will be selected as the volume of interest (VOI) which is either cubic or rectangular in shape. The use of 90° pulses creates a well-defined voxel within the sample, and minimizes contamination of the signal from sources outside the VOI. The pulses are spaced so that the chosen echo time (TE) coincides with the peak of the resultant stimulated echo. An important advantage to STEAM is its ability to acquire spectra at a quite short echo times (~30 ms). A disadvantage would be the relatively low signal-to-noise.

The general pulse sequence for STEAM [73-75] as shown in Figure (2.25) and described as

$$90° \rightarrow \tau_1 \rightarrow 90° \rightarrow (\tau_2 + \tau_3) \rightarrow 90° \rightarrow \tau_4 \rightarrow STE \qquad (2.94)$$

where τ_1 is the time interval between the first and second RF pulses, $\tau_2 + \tau_3$ is the time between the second and third RF pulses (also referred to as the mixing time TM), τ_4 is the time period after the third RF pulse, and $\tau_1 = \frac{TE}{2} = \tau_4$ (thus $\tau_1 + \tau_4 = TE$).

The three $90°$ RF pulses produce FIDs, multiple spin echoes (SE), and a stimulated echo (STE) (Figure 2.25). The first RF pulse produces an FID, which is then refocused by the second RF pulse, and produces a spin echo [SE(1,2)] that occurs at $2\tau_1$. This second RF pulse also produces a FID, which is then refocused by the third RF pulse, which in turn produces another spin echo [SE(2,3)] that occurs at $\tau_1 + 2(TM)$. The STE that is generated then occurs at $2\tau_1 + TM$. Another spin echo occurs at [SE(1,3)] which comes from the refocusing of the FID from the first RF pulse by the third RF pulse at time $2(\tau_1 + TM)$. During the first 90^o RF-pulse only half of the transverse magnetization is transformed into longitudinal magnetization by the second $90°$ pulse. During the mixing period TM, longitudinal magnetization decays with T_1 rather than T_2. The third $90°$ pulse transforms the longitudinal magnetization stored by the second RF pulse back into the transverse plane to form the stimulated echo STE. In this pulse sequence diagram, a CHESS pulse (as explained in Section 2.9.3) was used for water suppression before the first 90^o-pulse. Circles in the diagram represent the duration of the slice select gradients that are needed for selecting the VOI (Figure 2.25, parts (a - c)). The other gradients (crusher

gradients) on the diagram are used to dephase the spins from the CHESS pulse, and to suppress all other spin echoes and FIDs to leave only the STE.

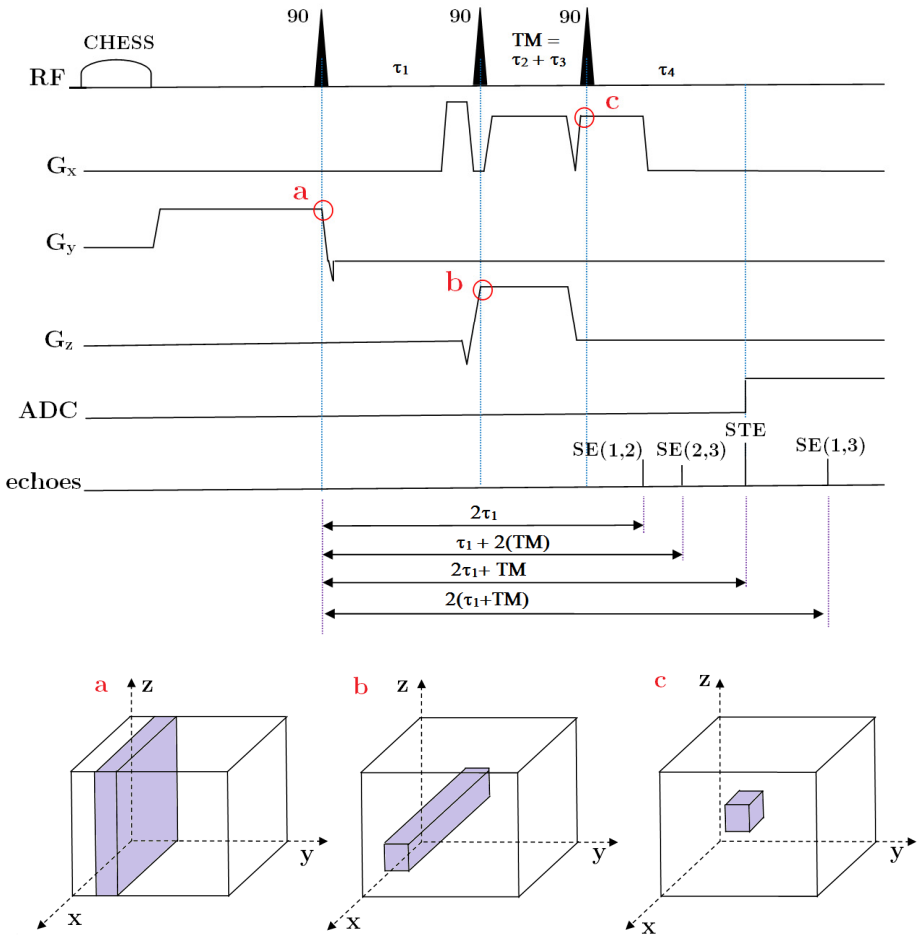

Figure 2.25: Pulse sequence diagram of STEAM sequence where CHESS was used for water suppression. (modified from [75])

2.10.2 Rapid Acquisition with Relaxation Enhancement (RARE)

Rapid Acquisition with Relaxation Enhancement (RARE) is a fast imaging sequence that employs an RF excitation pulse followed by a train of refocusing pulses to produce

multiple spin echoes. It is an extension of the one dimensional profile measurement first proposed by Henning et al. in (1986)[77], as shown in Figure 2.26.

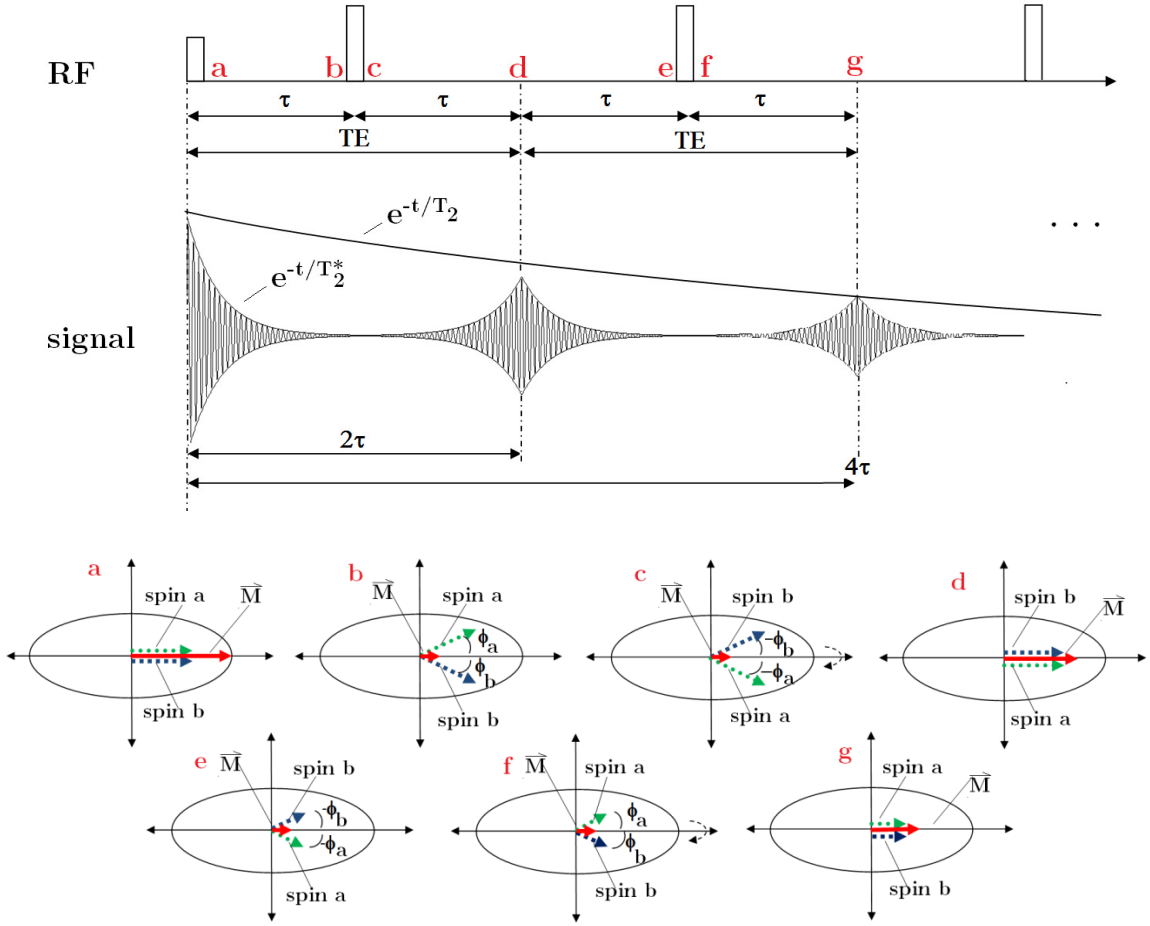

Figure 2.26 The RARE pulse sequence.

The reduction of scan time compared to conventional spin echoes is this the primary advantage of the RARE pulse, especially for T_2-weighted imaging [61]. The reduction in total imaging time occurs because each echo in this pulse sequence are spatially encoded such that that multiple k-space lines (or trajectories) can be sampled following each excitation pulse. For example, 16 echoes are phase-encoded in RARE, this decreases the

total acquisition time by a factor of 16 compared to that of a single-echo spin sequence with otherwise identical parameters. RARE images also are advantageous because they are less sensitive to off-resonance effects, such as B_o field inhomogeneity and tissue magnetic susceptibility variation. Disadvantages to RARE [61] include increased RF power deposition, blurring, edge-enhancement, ghosting, altered image contrast due to increased lipid signal intensities and magnetization transfer effects, and signal loss from magnetic susceptibility affects. In the experiments performed in this thesis, the advantages, especially the faster image acquisition time for the *in vivo* study, outweighed the disadvantages.

The RARE factor or echo train length (ETL) is the number of primary spin echoes (i.e. spin echoes associated with each refocusing pulse) produced by a RARE sequence, and generally is the same as the total number of RF refocusing pulses. The RARE factor equals the number of k-space lines acquired in a single TR interval if all echoes distinctively phase encoded. This RARE factor is an important parameter of RARE pulse sequences because it directly determines the scan-time reduction factor compared to conventional spin echo sequences, therefore, a higher RARE factor creates more reduction in scan-time. The maximal RARE factor that is affected by two factors: (1) tissue T_2 relaxation times (the lifetime of the transverse magnetization), and (2) the echo spacing (ESP) which are the intervals between the peaks of two consecutive spin echoes. RARE pulse sequences uses evenly spaced refocusing echoes with the time of echo spacing, t_{ESP} which is equal to 2τ and is the time between 180°-pulses.

The timings of the additional refocusing pulses of the RARE sequence are shown in Figure 2.26. After the initial acquisition of the spin echo (Section 2.6.1 continuing from Figure 2.14), another 180° refocusing pulse is applied at a time 3τ , where τ is the time interval between 90° and 180° pulse. Then the dephased magnetization vectors are pancake-flipped about the axis of the 180° pulse (Figure 2.26(f)) leading to another spin echo at 4τ as shown in Figure 2.26(g). This echo can be used to sample a second view from k-space. Usually the second view provides another phase-encoded line in Fourier imaging (as shown in Figure 2.26), but it can also be used for a second frequency-encoded radial line in a projection acquisition, a second interleaf in a spiral scan, or an additional trajectory in k-space sampling schemes. As long as the transverse magnetization does not substantially decay by T_2 relaxation, additional 180°-refocusing pulses can be applied at odd multiples of τ to form a train of spin echoes at even multiples of τ. The echo train generated after a single excitation of the magnetization can thus sample multiple k-space lines.

3 Methods

3.1 Animal Covert Stroke Model

This model incorporated several key clinical neuropathological features of covert stroke, namely white matter damage and small lacunar infarcts. Additionally, common clinical co-morbidities including age, hypertension and diet were also modeled, but most importantly, this model needed to exhibit a progressive loss of cognitive function created by all of the other factors. Ischemic covert stroke produces white matter damage and small lacunar infarcts that frequently arise in midline thalamic nuclei. The location of the brain at which these are found may interrupt connections of the prefrontal cortex which then contributes to the development of executive cognitive dysfunction. To mimic these features of ischemic covert stroke, the rats were subjected to mild hypoperfusion (reduction in blood flow to the brain) and the induction of lacunar infarcts in the mediodorsal nucleus of the thalamus.

The rodent model was developed at Memorial University (MUN) where male Sprague-Dawley rats were raised and maintained on either a control diet (REG) or a diet rich in fat, sugar, cholesterol and salt (HFSCS) as described in Section 3.2. After 6 months on each diet, these rats had surgeries performed. These surgeries were performed at this time because rats at this age were supposed to mimic middle age in humans for rats of this particular strain [78]. The first surgery the rats received was to reduce their overall blood

flow to the brain to simulate clogged arteries attributed to hypertension. This was done by using a bilateral or 2-vessel occlusion (2-VO) of the common carotid arteries to induce mild hypoperfusion as described in Section 3.1.1. Lacunar infarcts were also induced in some groups of rats, and were created by unilateral injections of the vasoconstrictor Endothelin-1 (ET-1) in the mediodorsal nucleus of the thalamus (MD) as described in Section 3.1.2. This ET-1 injection was performed in conjunction with the 2-VO surgery. Age matched controls that have same dietary history (HFSCS or REG diet) were given sham surgeries instead of 2-VO, wherein the carotid arteries were exposed but not occluded and saline (instead of ET-1) was injected in the MD. All of the surgeries took place in MUN and were performed by the Corbett group at MUN. The experimental protocol was approved by MUN's Institutional Animal Care Committee (IACC) and Animal Care Services, and adhered to the guidelines and principles created by the Canadian Council on Animal Care.

For the *in vivo* study, there were 2 sets of rats, in which each set contained combinations of the diet and surgeries. One set of rats remained at MUN for behavioural testing, and the other set was sent to the University of Manitoba (UM) for MR imaging. Table 3.1 explains how the rats were designated into six groups, and the number or rats assigned to each group.

Table 3.1: *In vivo* study - Group designations. HFSCS = diet high in fat, salt, cholesterol, and sugar. REG = normal diet. 2VO = occlusion of the carotid arteries reducing blood flow to the brain. MD = induced stroke in the mediodorsal thalamic nucleus with an injection ET-1. SHAM = surgery where carotid arteries were only exposed (not occluded), and injected with saline instead of ET-1. The * indicates a control group.

Group	**Number per group**	**Diet and Surgery**	**Description**
I-1	11	HFSCS - 2VO	HFSCS diet, and had 2-VO surgery
I-2	6	HFSCS - MD	HFSCS diet, and MD stroke was induced
I-3	14	HFSCS - 2VO+MD	HFSCS diet, and had both 2-VO and MD surgeries
* I-4	13	HFSCS - SHAM	HFSCS diet, and had the SHAM surgery
I-5	6	REG - MD	Normal (REG) diet, and MD stroke was induced
* I-6	12	REG - SHAM	Normal (REG) diet , and had the SHAM surgery

The *in vivo* study was performed blind and the numbers of the rats were not provided until after analysis was completed. The reasons for the variation in the number of rats per group for both the *in vivo* and *ex vivo* studies and also for why not all rat groups were represented in this experiment was dependent on what was received from the Corbett group at MUN, and for the fact that there was a high mortality rate for these rats due to the type of surgeries performed and also because they were required to travel to Winnipeg from Newfoundland for the MR analysis.

The *ex vivo* study was conducted because the first batch of rats to arrive at UM for the *in vivo* study had microchips inserted that were not MRI compatible and therefore only *ex vivo* imaging could be performed. This group of rats (separate from the *in vivo* study) were imaged at UM for any abnormalities in the brains and livers. This group of rats contained combinations of diet and surgeries and were divided into five groups as given in Table 3.2.

Table 3.2: *Ex vivo* study - Group designations. HFSCS = diet high in fat, salt, cholesterol, and sugar. REG = normal diet. 2VO = occlusion of the carotid arteries reducing blood flow to the brain. MD = induced stroke in the mediodorsal thalamic nucleus with an injection ET-1. SHAM = surgery where carotid arteries were only exposed (not occluded), and injected with saline instead of ET-1. The * indicates a control group.

Group	Number per group	Diet and Surgery	Description
E-1	3	HFSCS - 2VO	HFSCS diet, and had 2VO surgery
E-2	4	HFSCS - 2VO+MD	HFSCS diet, and had both 2VO and MD surgery
* E-3	2	HFSCS - SHAM	HFSCS diet, and had SHAM surgery
E-4	1	REG-2VO	Normal (REG) diet, and had 2VO surgery
* E-5	4	REG - SHAM	Normal (REG) diet, and SHAM surgery

The timeline for when the rats began their diets, received their surgeries, and were assessed with behavioural testing or MR imaging is shown in Figure 3.1.

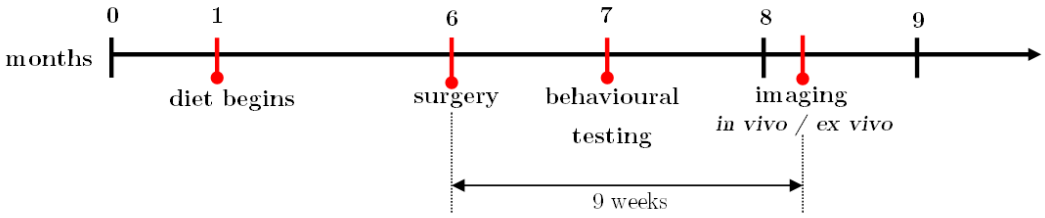

Figure 3.1: Timeline for diet, surgery, behavioural testing and imaging.

3.1.1 2-VO

At the age of 6 months, rats were subjected to permanent bilateral occlusion (otherwise known as 2-vessel occlusion, 2-VO) of the carotid arteries while under 1.5 - 2.0% isoflurane anesthesia. This 2-vessel occlusion involved the carotid arteries being doubly ligated with nylon sutures to cause a reduction in the amount of blood flow to the brain, which in turn

created the white matter damage. The location of the common carotid arteries on the rat is shown in Figure 3.2. This surgery was performed to mimic hypoperfusion similar to what occurs with aging and the early stages of VCI. For the control rats (SHAM groups), the sham surgery was performed which consisted of only exposing the carotid arteries.

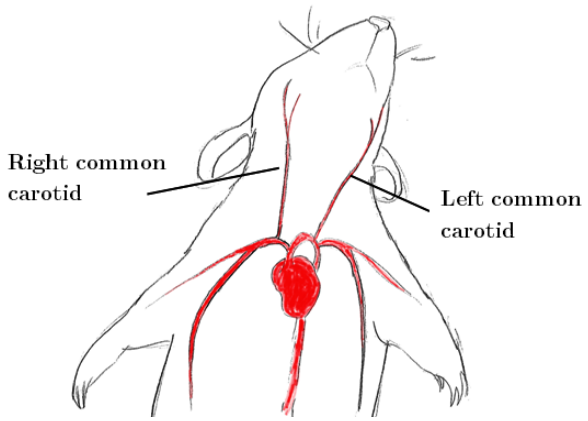

Figure 3.2: Diagram of the location of the common carotid arteries on the rat model where the 2-VO surgery was performed.

3.1.2 MD Stroke

Some groups of rats had small, unilateral lacunar infarcts (or strokes) induced in the mediodorsal (or midline) thalamic nucleus (MD) by using stereotaxic injections of 0.25 µl Endothelin-1 (ET-1, 400 pmol). Endothelin-1 was used because it is a vasoconstrictor composed of proteins that constrict blood vessels and raise the blood pressure, similar to that of patients who experience hypertension (high blood pressure) and heart disease. The rat is placed in a stereotaxic apparatus, and a midline incision is made into the scalp (1.5 – 2 cm. The needle is placed in the desired location, which has been prepared and marked

using standard coordinates from a rat atlas, in the rat's striatum, and the ET-1 solution is injected. This surgical procedure was performed at the same time as the 2-VO surgery, and for the control rats (SHAM groups), where for the sham surgery, the rats received saline injections instead of ET-1. In this thesis, this type of surgery was classifed or referred to as either MD or MD stroke.

3.2 Diet

The diet that was high in fat, sugar, cholesterol, and salt (HFSCS) was used in order to create the co-morbidity factors (such as hypertension) that predispose humans to small vessel disease. Rats were reared from weaning (~1 month of age), on either the HFSCS diet, or a normal (REG) diet. This diet was first introduced to the rats five months prior to the surgeries and was maintained for the duration of the study. The HFSCS diet is high in saturated and monosaturated fat (~39% energy), high in sugar (sucrose, ~40% energy) and ~3.0% sodium. The REG diet is low in sodium (0.4 %), saturated fat (~13% energy) and high in carbohydrates (starch, 59% energy). A supply of each diet was provided to the lab at UM for the maintenance of rats shipped from the MUN lab.

3.3 Behavioural Analysis

Attention and executive function were assessed at MUN to capture the most common deficits associated with VCI in humans. Rats that had sufficient sensory-motor and visual functions were chosen to participate in this study. Four weeks after the surgeries were performed; testing started using an attentional set-shifting paradigm to assess executive function. This type of test was performed with the specific goal of identifying when the executive deficits first emerge after the surgeries. These surgeries were performed to mimic the ischemic covert stroke, by producing white matter damage and small lacunar infarcts which frequently arises in midline thalamic nuclei that may interrupt connections of the prefrontal cortex and contribute to the development of executive cognitive dysfunction. The prefrontal cortex is the area of the brain that mediates the shifts in attention between perceptual dimensions (or features) of complex stimuli. When attending to a perceptual dimension of a stimulus (e.g. colour), learning to discriminate between a new stimulus of the same perceptual dimension is referred to as an intradimensional shift (ID), because the new learning requires shifting attention to the new stimulus but the same perceptual dimension is still relevant. In an extradimensional shift (ED), a new discrimination requires that attention be directed to a different perceptual dimension of a stimulus (e.g. shape) and the previously attended dimension (colour) must be disregarded. When lesions occur in the prefrontal cortex, this impairs the ability to shift the attention from one perceptual dimension of a stimulus to another in the ED shift.

3.3.1 Attentional Set-Shifting Tests

Impairments in executive function were assessed using a rodent attention set-shifting test which generally followed procedures outlined in Birrel and Brown [8] with mildly food restricted rats (fed 15-20 g vs 30 g of food per day). For this test, the rats learned several two-choice discrimination problems between two pairs of stimuli that differed in three sensory dimensions. The rats were trained to obtain the food reward placed into one of two bowls, with the reward indicating the relevant stimulus. The digging bowls that were used in this test were ceramic pots, and the food reward used was a piece of fruit loop cereal. The three sensory dimensions in this experiment were: external texture of the digging bowl, type of digging medium, and scent of digging medium [Figure 3.3].

Figure 3.3: Attentional set shifting task. (a) Test entails the discrimination of a stimulus dimensions paired with a buried food reward. (b) Sample stimulus set that differs in the stimulus dimensions: external texture, digging medium and odor. (c) Attention shifts are made so that the new stimulus set is in the same or different in stimulus dimension [80].

The test apparatus was designed to separate the two digging bowls used in the test, as well as have a removable divider that separated the rat from the bowls until the rat was

given access. This divider also enabled the experimenter to block access to the bowl, particularly after an error which indicated when the rat does not find the food reward. Each test was performed for several trials, where the first 4 trials were discovery trials allowing the rat to dig into both bowls to find the food reward. On subsequent trials, if the rat started to dig into the unbaited bowl, an error was recorded and the trial terminated. Testing continued until the rat reached a criterion level of performance of six consecutive correct trials. In this test, the reward was consistently associated with one element of a single dimension, where in a single test session the rats performed a series of discriminations, which consisted of either: simple discrimination (SD), a compound discrimination (CD), reversals (REV), ID shift, or the ED shift.

In the simple discrimination (SD), the bowls differed along one of the 3 dimensions. For example, the scent of the digging medium would differ between the bowls, nutmeg vs. lavender, with the nutmeg odour being the relevant stimulus. For the compound discrimination (CD), a second dimension was introduced, but the correct and incorrect exemplars from the SD remained constant. An example of this would be having the type of digging medium differ (beads vs. sawdust) however the relevant stimulus would still be the nutmeg odour from the SD. For the reversals (REV), the exemplars of the relevant dimensions were unchanged, but the rat had to learn that the previously correct stimulus were now incorrect. For example, if the relevant odour was nutmeg, the reversal would now have lavender be the relevant odour. For both the ID and ED shifts, new exemplars of both the relevant and irrelevant dimensions would be introduced, however in the ED

shift, the previously relevant dimension would now be the irrelevant dimension. Example of an ID shift would be to introduce all new digging mediums and odours, with odour still being the relevant dimension (as previous), and the digging medium still being irrelevant. The ED shift would however have the previously irrelevant stimulus (digging medium) now be relevant, instead of the odours. To further explain what occurred in this experiment, the following behavioural testing sequence performed at MUN is outlined in Table 3.3.

Table 3.3: Attention set shifting test is comprised of SD and CD and an attention shift to stimuli with same dimensions (e.g. odour), and an attention shift to a stimulus in a new direction (e.g. digging medium), reversals and learned irrelevance.

Test	**Stimulus Discrimination**	**Rewarded Stimulus**	**Irrelevant Discrimination**
1	Simple Discrimination (SD)	Nutmeg odor	
2	Compound Discrimination (CD)	Nutmeg odor	Digging medium & external texture
3	Intra-dimensional shift (ID)	Lavender odor	Digging medium and external texture
4	Reversal 1 (REV 1)	Orange odor	Digging medium and external texture
5	Extra-dimensional shift (ED)	Textured beads	Odour & external texture (flat)
6	Reversal 2 (REV 2)	Round beads	Odour & external texture (flat)

Test 1: In the SD, bowls differed along one of the three dimensions (e.g. nutmeg odor).

Test 2: In the compound discrimination (CD), a second dimension was introduced (e.g. digging medium), but the relevant stimulus (nutmeg odour) in SD would identify the correct bowl.

Test 3: An intra-dimensional (ID) shift is performed where two new odours (eg: lavender and orange odours) were presented where only one of these odours (lavender odour) would identify the baited bowl and the other stimulus (digging medium) would still be irrelevant.

Test 4: A reversal (REV1) where the rat had to learn that the previously correct stimulus (lavender odour) was now incorrect and the other odour (orange odour) would be correct with the second stimulus (digging medium) still being irrelevant.

Test 5: Following the reversal, the rats would then be required to perform an extra-dimensional (ED) shift, wherein the previously irrelevant stimulus (digging medium) would now be relevant, and one of the digging mediums (e.g. textured beads) would identify the baited bowl, while the odour would now be irrelevant.

Test 6: A second reversal (REV2) was introduced where the rat had to learn that the previously correct stimulus (textured beads) was now incorrect and the other digging medium (round beads) would be the correct stimulus.

3.4 *In Vivo* MRI

Following the surgeries, the rats were shipped to UM. MR images of the rats were obtained at 9 weeks post-surgery in order to assess for morphological changes such as the progression of lacunar infarcts/stroke and the development of white matter hyperintensities. These experiments were performed on a 7T/21cm Bruker Avance III MRI system with Paravision 5. Live brains were imaged for total brain volume, ventricle volume, and the volume of brain without the ventricles. The study was performed blind as to which rats were in what diet and surgery groups and their designations were revealed after analysis was performed. The experimental protocol was approved by the University of Manitoba Animal Care Committee who adhere to the guidelines and principles created by the Canadian Council on Animal Care.

3.4.1 *In Vivo* Imaging - Set Up

For each *in vivo* imaging study, the rat was anesthetized with isoflurane in O_2/N_2O (isoflurane 3-5% induction, 1.5-2.0% maintenance) with a nose cone placed inside the magnet. The rat was placed into a holder with the head positioned in a custom built 33 mm, 300 MHz quadrature volume coil (NRC Institute for Biodiagnostics, Winnipeg, MB, Canada) using an incisor bar to minimize its motion. Respiration and external body temperature were monitored during imaging using a MR-compatible small animal monitoring and gating system (SA Instruments, Inc. Stony Brook, NY), where a

temperature probe was placed under the rat. External temperature was maintained with a heating circulator bath (Thermo Scientific Haake, Karlsruhe, Germany) between 36 - 37°C, as the rat lay atop a heating pad. Lubricating drops were placed into the eyes to prevent from drying. Figure 3.4 shows the rat placed in the imaging apparatus (Figure 3.4(a)), and after the head is placed inside the volume coil (Figure 3.4(b)).

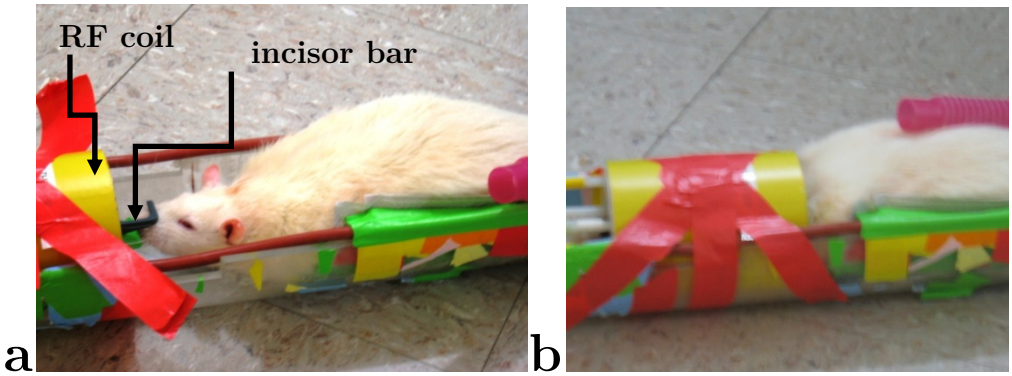

Figure 3.4: Placement of rat in imaging holder for *in vivo* study. (a) Rat placed in holder for *in vivo* study. The bite bar is used to restrict the rat's movement. (b) Head is placed into the RF coil, and the entire holder is placed into the magnet.

MRI begun once the rat was properly placed into the holder. The RF coil was tuned and matched and then shimming of the main magnetic field gradients was performed to adjust the homogeneity of the magnetic field B_o. Also, RF pulse amplitudes were calculated and the receiver gain was adjusted dependent on which pulse sequence was being used. A pilot scan was performed in order to ensure proper placement of the rat. This was followed by a series of spin-echo scout scans in order to select the region of interest (ROI) that was reproducible and consistently had the axial slices oriented relative to the centerline of the

brain. The scout scans required to select the ROI are shown in Appendix A.1. The single slices obtained per scout scan had the following parameters: 4.0 cm^2 FOV, 1 average, TR = 3000 ms, effective TE = 15 ms, 1.00 mm slice thickness, 0.3125×0.3125 mm^3 resolution, RARE factor 36, and acquisition time of 6 seconds.

The axes of the brain needed to be centred and aligned with the axes of the image. For reference, Figure 3.5 will be referred to in the alignment of the brain in both *in vivo* brain (Section 3.4.1) and *ex vivo* brain (Section 3.5.1) imaging. Using Figure 3.5 as a reference, Table 3.4 outlines how the axes of the brain are aligned with the axes of the image in the scout scans of Appendix A.1.

Table 3.4: Slice orientations (axial, coronal and sagittal) and their corresponding horizontal and vertical image axes aligned with the axes of the brain (medial-lateral, anterior-posterior, and head-foot).

Slice Orientation	**HORIZONTAL AXIS**	**VERTICAL AXIS**
AXIAL	Medial - Lateral	Anterior - Posterior
CORONAL	Medial - Lateral	Head - Foot
SAGITTAL	Anterior - Posterior	Head - Foot

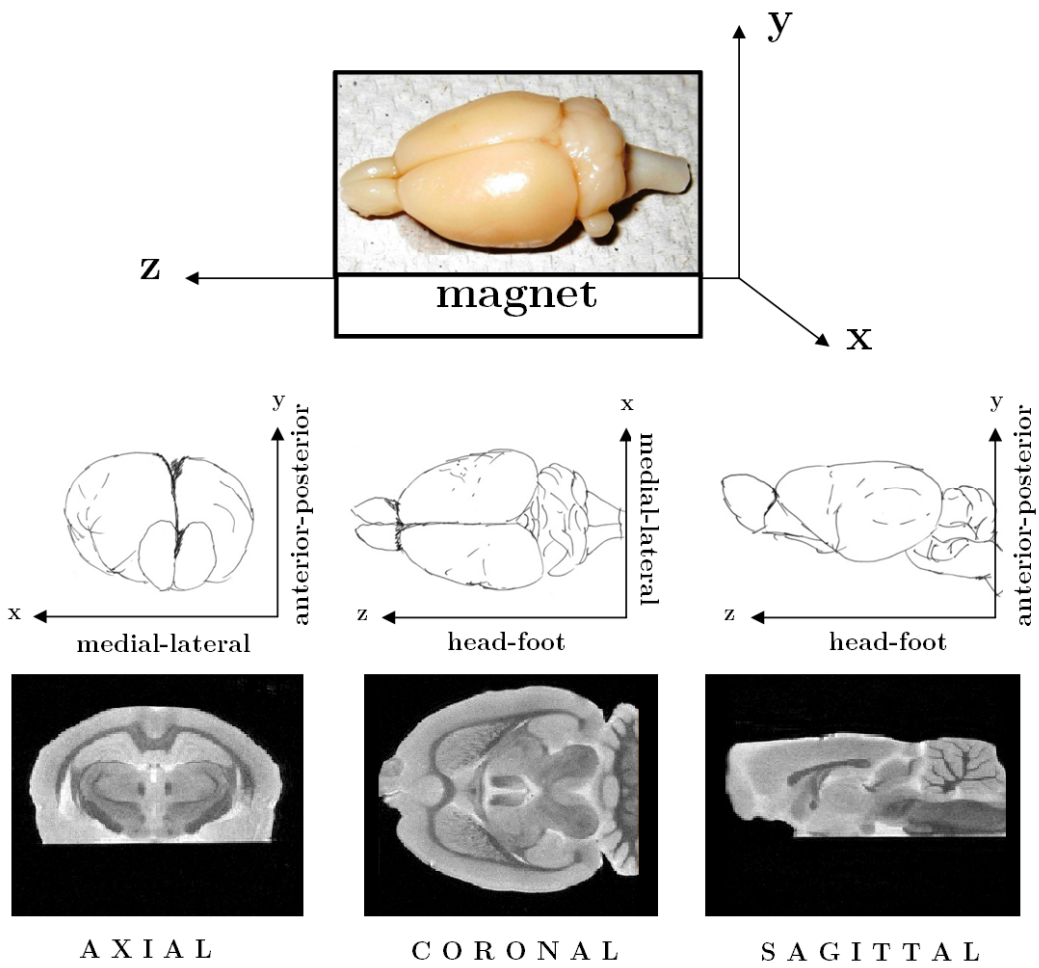

Figure 3.5: Orientation of brain according to body axes. Brain planes were named based on the body axes. Axial is in the xy-plane, coronal is in the xz-plane, and sagittal is in the yz-plane.

The slices were selected to encompass the region where the Endothelin-1 was injected into the mediodorsal thalamic nucleus to induce the stroke. To do this, the ROI was centred around the anterior commissure as shown in Figure 3.6. Figure 3.7 shows an axial slice of the brain taken from MRI, showing the region where the mediodorsal thalamic nucleus is found (circled). The use of a rat atlas [79] was required for verification to discern between

brain anatomy for more accurate location of this region. Figures 3.6 and 3.7 are high resolution MRI obtained from the *ex vivo* study, to show the anatomy of the brain.

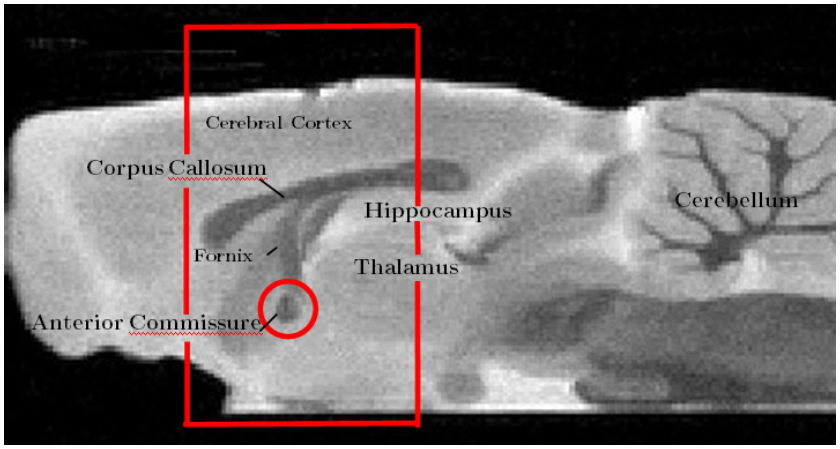

Figure 3.6: Sagittal slice obtained from MRI of a rat in the *ex vivo* study, shown for clarity of regions in the brain. The region of interest is highlighted (red box) and centred around the anterior commissure (circled), encompassing the ROI where the stroke was induced in the mediodorsal thalamic nucleus.

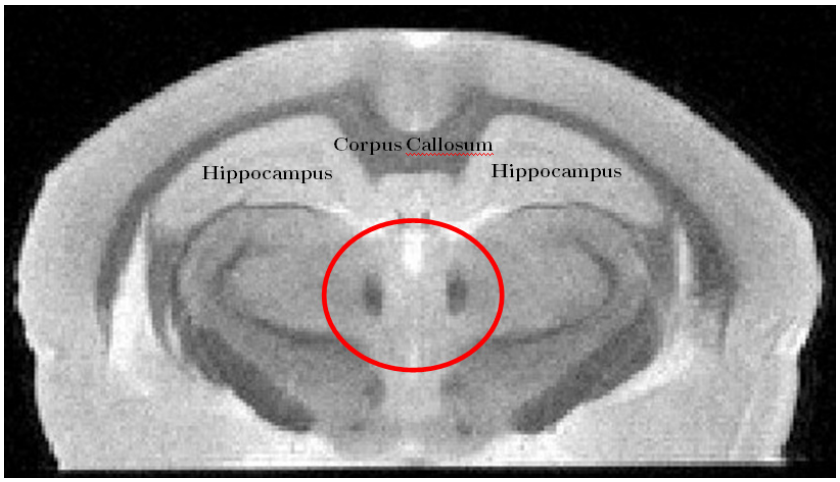

Figure 3.7: Axial slice obtained from MRI corresponding to slice #4, which is located at 2 mm from the anterior commissure. The area circled in red shows the region where the mediodorsal thalamic nucleus (MD) is located and verified with the use of a rat atlas [79].

3.4.2 *In Vivo* Imaging - Acquisition

Once the scout scans (from Appendix A.1) have centered the brain along the image axis as per Figure 3.5, image slices were then acquired for analysis. To select these slices, a RARE pulse sequence (as described in Section 2.10.2) was used to obtain seven axial slices with the following parameters: 3.0 cm^2 FOV, 12 averages, TR = 1640 ms, effective TE = 80 ms, slice thickness of 0.75 mm, interslice distance of 1.00 mm, 256 × 256 matrix, 0.117×0.117×0.750 mm^3 resolution, RARE factor 8, and acquisition time of 10.5 minutes.

The slice volume was placed horizontally on the centered sagittal image as obtained from the scout scan 3 (Appendix A.1 - Figure A.1.3). Slice #2 is centred on the anterior commissure, which places the slice of interest (middle slice #4) at 2 mm from the anterior commissure, as shown in Figure 3.8.

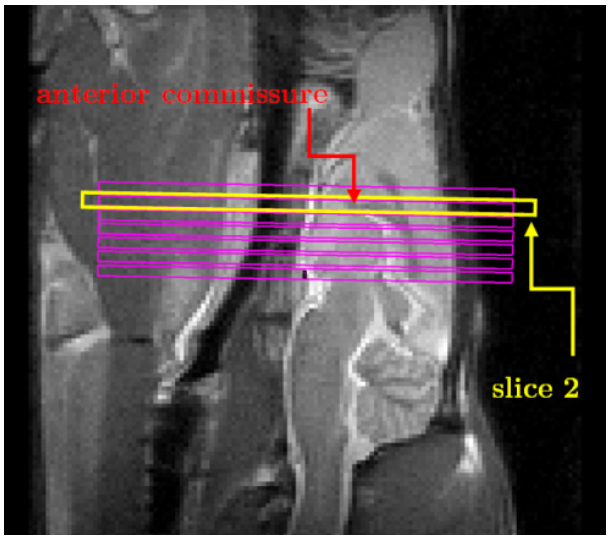

Figure 3.8: *In vivo* study - Image acquisition. Seven slices were obtained for 3D imaging. Slice #2 was centered at the anterior commissure allowing slice #4 to be in the middle of the ROI, which contains the mediodorsal thalamic nucleus, the site where the stroke was induced, and corresponds to the axial image slice of Figure 3.8.

3.5 *Ex Vivo* MRI

The first batch of rats to arrive at UM had microchips inserted in them that were not MRI compatible and therefore *in vivo* imaging could not be performed. Because this was the pilot study, a set method was not yet established and the microchips were put in by mistake. In order to use these rats, *ex vivo* imaging was performed instead on the livers and brains. These rats were perfused and organs that did not contain the microchips were removed so they could be imaged. The rats were perfused with 250 mL cold saline followed by 200 mL cold 4% paraformaldehyde (PFA). The brains and livers were quickly removed and then post-fixed in 50 mL cold 4% PFA and stored in specimen bottles in the fridge. After 24 hours of the post-fix, the PFA was poured off and replaced with cold 20% phosphate buffered saline (PBS) with sucrose. These brains and livers were then stored in the sucrose solution and put in the fridge and could be stored for extended periods (months).

T_2-weighted MR images were acquired on fixed brains and livers of these rats (control and experimental groups). Brains were imaged to determine if any abnormalities could be found, i.e. the presence of lacunar infarcts or white matter damage. Fixed livers were analyzed for fat content in order to assess how a HFSCS diet can affect the organs.

3.5.1 *Ex Vivo* Brain Imaging - Set Up

To prepare for image acquisition the rat brain was removed from the sucrose solution and placed on a histology slide, carefully removing any of excess liquid in which it was stored. Teflon tape was used to secure the brain in position and then the histology slide was placed into a 50 mL sample tube, containing room-temperature Fomblin® perfluoropolyether Y04 grade fluid (Solvay Solexis). A piece of styrofoam was placed on top of the slice to secure it into place and prevent it from moving during the experiment (Figure 3.9). The Fomblin® was used to eliminate the external proton signal and the susceptibility artifacts and also to maintain the moisture in the samples. Fomblin has magnetic susceptibility to that of tissue, has no hydrogen (^{1}H), and thus does not produce a MR signal.

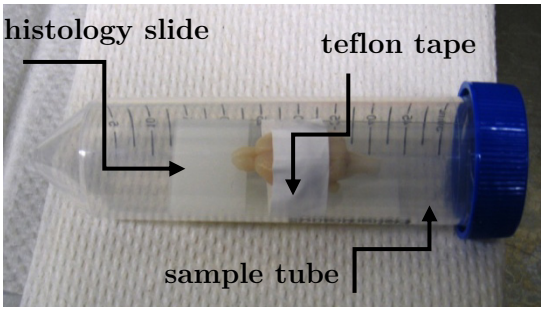

Figure 3.9: Placement of rat brain for *ex vivo* study. Excised brain on histology slide and in the sample tube.

The sample tube was then placed into a Bruker 35 mm volume coil, secured into place with the use of paper towels for stability. The volume coil was then placed at the centre of the magnet. MRI began once the brain was properly centred in the magnet with the

use of a pilot scan. Similar to *in vivo* imaging, the RF coil is tuned and matched, the magnetic field shimmed, RF pulse amplitudes calculated and the receiver gain adjusted based on pulse sequence used.

A series of spin-echo scout scans were then performed in order to select the ROI that was reproducible, and consistently had the slices being acquired oriented relative to the centerline of the brain. The scout scans required to select the ROI are shown in Appendix A.2. The slices were contiguous and selected to encompass the region where the Endothelin-1 was injected to induce the stroke (similar to *in vivo* imaging). Slices were centered around the anterior commissure and the first slice was placed at 2 mm above the anterior commissure for slices obtained in the axial orientation, whereas the fifth slice was centred on the anterior commissure for slices obtained in the coronal orientation.

3.5.2 *Ex Vivo* Brain Imaging - Acquisition

Acquisition of sagittal, axial and coronal oriented high resolution images are described in this section. For the excised brains, a RARE pulse sequence (as described in Section 2.10.2) was used to acquire the slices. Sagittal slices (9 in total) were first acquired and then used as a reference for the axial and coronal slices. Parameters for the sagittal slices are: 4 averages, 3.0 cm^2 FOV, TR 1500 ms, RARE factor 4, acquisition time of 6.4mins. Both the axial and coronal slices (two interleaved sets each having 15 slices) using the following parameters: 128 averages, 2.0 cm^2 FOV, TR 2500 ms, RARE factor 4, acquisition

time of 3.4 hours. The slice thickness for all slices was 0.25 mm, interslice distance was 0.50 mm, and effective TE 24 ms.

The pulse sequence that was used for the acquisition of these slices allowed for higher resolution images compared to the slices obtained for the *in vivo* images. Higher resolution images were acquired because extra time could be used for acquisition as *ex vivo* images do not have the time constraints that the *in vivo* images do. The two interleaved sets of 15 slices for both axial and coronal orientations were imaged in order to minimize interslice excitation and the slice orientation was based on how the brain was placed in the tube.

(i) High Resolution Sagittal slices: Using the centred axial slice obtained from the scout scans (Appendix A.2 - Figure A.2.7), a set of 9 slices were taken, each slice having a thickness of 0.75 mm, interslice distance of 1.00 mm, and 3.0 cm^2 FOV. The slice volume was aligned such that the middle slice (slice #5) was positioned to the midline of the axial image (Figure 3.10).

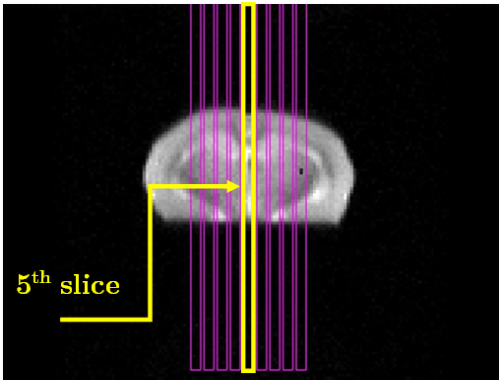

Figure 3.10: *Ex vivo* study - Selection of ROI for high resolution sagittal slice. Using the centred axial slice, 9 slices were acquired, with the middle (5th) slice positioned at the centreline of the brain.

An example of the high resolution sagittal image is shown in Figure 3.11. This sagittal slice orientation was used as a reference to acquire both the high resolution axial and coronal images.

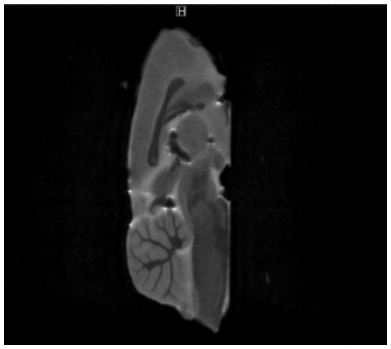

Figure 3.11: High resolution sagittal slice. This slice was used to determine slice position for the high resolution axial and coronal slices.

(ii) *High Resolution Axial Slices:* Two interleaved sets of axial images (15 slices each) were obtained (for a total of 30 axial slices). Each slice had a thickness of 0.25 mm, interslice distance of 0.50 mm, and 2.0 cm^2 FOV. Reference axial orientation images obtained from previous scout scans (Appendix A.2 - Figure A.2.7) were used to ensure that the FOV encompassed the entire brain.

Using the high resolution sagittal slice (Figure 3.11), the selected slices were aligned horizontally with respect to the bottom of the brain (Figure 3.12). The first set of axial slices were placed at 2mm above the top of anterior commissure (Figure 3.12(a)). The second set of axial slices were placed 0.25 mm below the previous slice set (Figure 3.12(b)). From this acquisition, an example of the high resolution axial slice is shown in Figure 3.13.

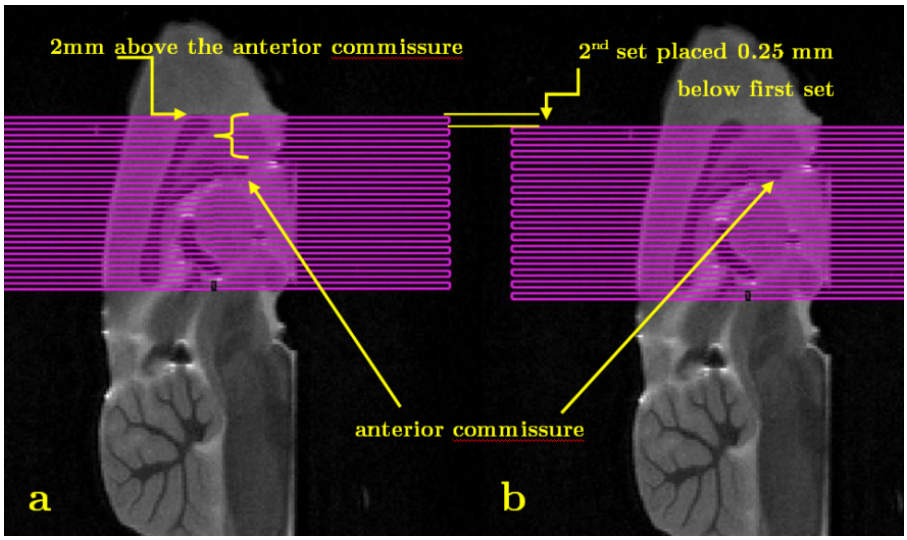

Figure 3.12: *Ex vivo* study - Selection of ROI of high resolution axial slices. (a) Set 1. The slice volume started at 2 mm above the top of the anterior commissure. (b) Set 2. The slice volume was set 0.25 mm below Set 1. This produced axial images that encompassed 1.5 mm of the brain.

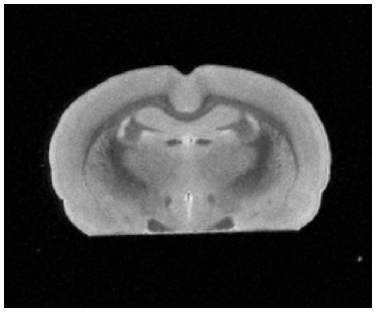

Figure 3.13: Example of a high resolution axial image.

(iii) *High Resolution Coronal Slices*: Two interleaved sets of coronal images (15 slices each) were obtained (for a total of 30 axial slices). Each slice having a thickness of 0.25 mm, interslice distance of 0.50 mm, and 2.0 cm^2 FOV. Reference coronal orientation images obtained from the scout scans (Appendix A.2 - Figure A.2.6) were used ensure that the alignment of the FOV encompassed most of the forebrain.

Using the high resolution sagittal slice (Figure 3.11), the slices selected were aligned vertically with respect to the bottom of the image (Figure 3.14). The first set of coronal images were aligned so that the 5th slice encompassed the anterior commissure (Figure 3.14(a)). The second set of slices were placed so that the slices were 0.25 mm left (or right) of the previous set (Figure 3.14(b)). An example slice in the coronal direction is shown in Figure 3.15.

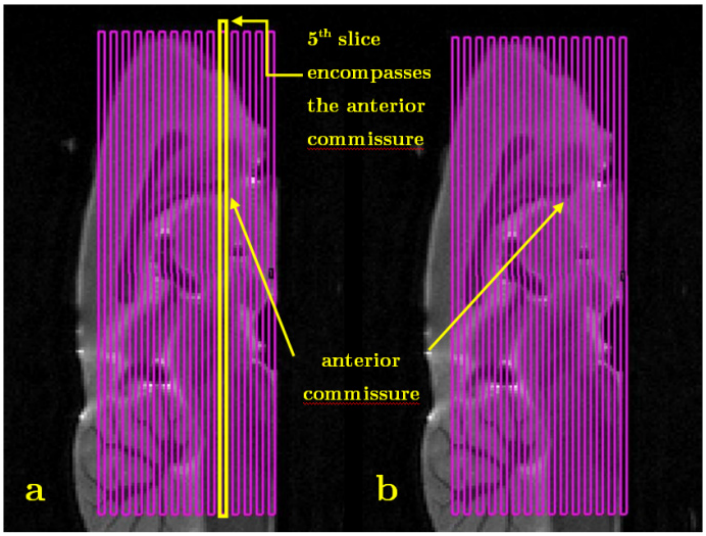

Figure 3.14: *Ex vivo* study - Selection of ROI of high resolution coronal slices. (a) Set 1: The 5th slice encompasses the anterior commissure. (b) Set 2: The slice volume is shifted 0.25 mm from the previous set. This produced coronal images that encompassed 1.5 mm of the brain.

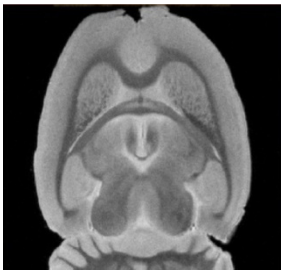

Figure 3.15: Example of a high resolution coronal image.

3.6 *Ex Vivo* MRS

Liver images and more importantly, spectroscopy of these livers were obtained to determine the percentage of fat contained in the liver, because comparisons could be made between the two diets that these rats consumed. Because of the large size of the livers (especially those from the HFSCS diet group), only the top lobe of the liver was used for analysis because the entire liver could not fit into the sample tube that was used. A comparison of the top lobes of livers from a HFSCS and REG diet are shown in Figure 3.16, which clearly shows the difference in both size and texture between the livers from the two diet groups.

Figure 3.16: Comparison of livers (top lobe only) from a HFSCS (left) and REG (right) diet. HFSCS liver is larger in comparison to the REG liver. The appearance of the HFSCS liver was lighter in color and appeared more dense and more prone to crumble, than the REG liver.

Similar to the excised brains (Section 3.5.1) preparation for the rat liver involved removing it from the sucrose solution in which it was stored. The top lobe was placed into a 50 mL sample tube containing Fomblin® and secured with a piece of styrofoam to restrict its movement because objects have a tendency to float within the Fomblin®. The sample

tube was then placed into the Bruker 35 mm quadrature volume coil and secured in place with the use of paper towels. The coil was then placed into the centre of the magnet.

3.6.1 *Ex Vivo* Liver Imaging - Set up

Prior to data image acquisition, setup scans were performed in order to centre the position of the rat liver/coil in the magnet. Once centred, the desired ROI was obtained using scout scans.

3.6.2 *Ex Vivo* Liver Imaging - Acquisition

Images for livers are not really important for analysis, but were obtained in order to place the ROIs for spectroscopy. These images also showed the physical differences between HFSCS diet and REG diet livers. The T_2-weighted images of the liver were obtained with the following parameters: one axial slice, slice thickness 0.75, 3.0 cm^2 FOV, 256×256 matrix size, effective TE = 24ms , TR = 2500 ms, 4 averages, and an acquisition time of 10 min 40 s.

The liver images were obtained and labelled as: 'cross' slices which were vertical with respect to the length of the sample tube, and 'top' slices which were horizontal with respect to the length of the sample tube (Figure 3.17). Images were acquired by adjusting

the FOV and the number of slices to encompass the entire liver (Figure 3.18) and an example images in both orientations is shown in Figure 3.19.

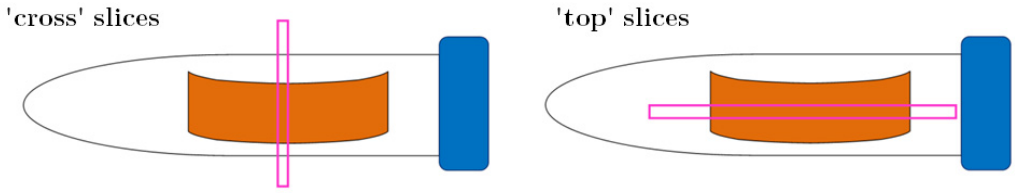

Figure 3.17: Orientation of slices selected for liver imaging. Only one slice (pink box) is shown for each orientation above, however the FOV has a number of slices that would encompass the entire liver as per Figure 3.17. These images will be used to determine the ROI for spectroscopy.

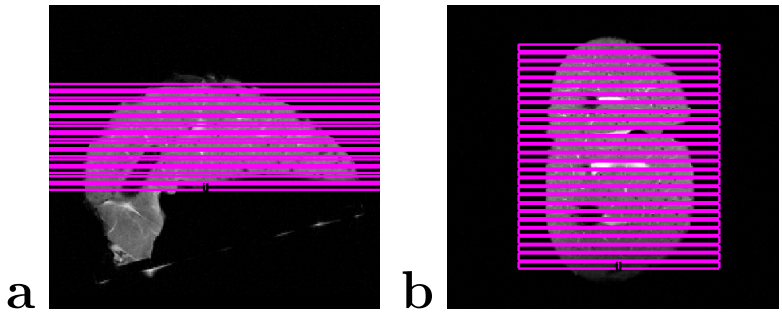

Figure 3.18: Selection of ROI for the 'cross' and 'top' orientations of liver imaging. Slices were chosen to encompass the entire liver in the (a) 'cross' and (b) 'top' orientations of the liver. The ROI for spectroscopy was obtained by using the images acquired.

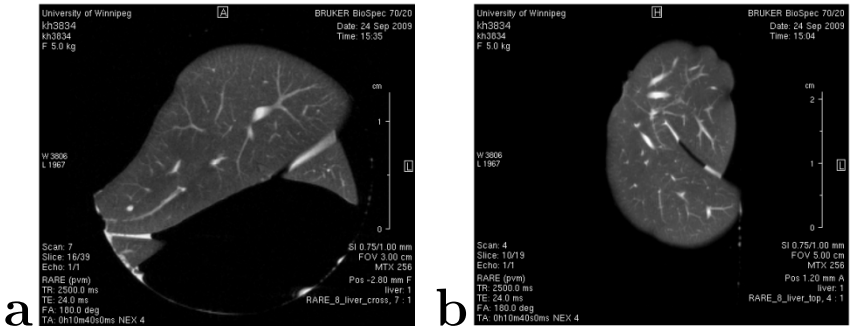

Figure 3.19: Examples of (a)'cross' and (b)'top' slice of a liver.

3.6.3 MR Spectroscopy

Fat content in the excised liver was calculated in two regions of interest; at the centre and at the edge of the lobe with a FOV of 4.0 mm^3 (Figure 3.20) by the integration of the areas under the fat peak and water peaks. The selection of the FOV needed to avoid large blood vessels or tracts and be placed close to the middle of the images acquired (in either the 'top' or 'cross' slices). In these spectra, the water peak is located at ~4.7 ppm, and the fat/CH2 peak at ~1.1 ppm.

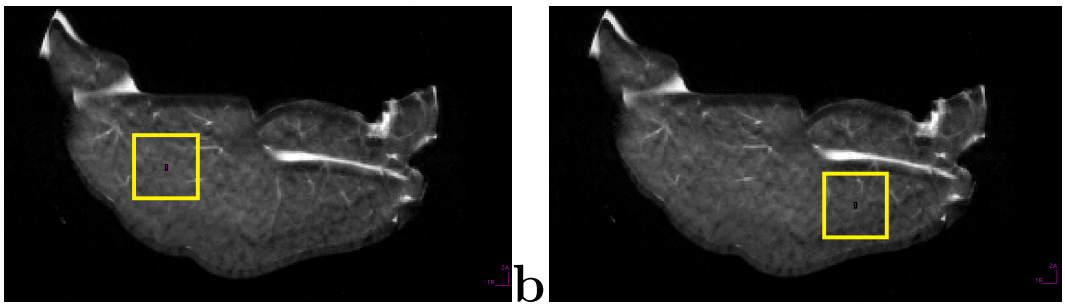

Figure 3.20: FOV of the liver was chosen (yellow box) at two ROIs: (a) at the centre, and (b) near the edge of the lobe. The FOV must avoid large blood vessels or tracts.

The spectra of the livers were collected using the STEAM spectroscopy method (as described in Section 2.10.1) with the following parameters: no water suppression, 512 averages, TE 30 ms, TR 1500 ms, and an acquisition time of 12.9 mins. While blinded to the study groups, the diet groups were easily distinguished by separating the higher fat content values obtained from those that had lower values, which corresponded to the HFSCS and REG diets respectively.

3.7 Segmentation

In order to determine if the surgeries and diet affected the volume sizes of the brain and ventricles, segmentation was performed on the images for the *in vivo* brain data. Manual segmentation and analysis for the *in vivo* brain data was performed with the use of AMIRA® software. Segmentation was performed using the Segmentation Editor in AMIRA® in the 'axial' plane view (xy-plane) slice by slice. This program was first used to segment the brain from the rest of the anatomy (Figure 3.21 (a-b)). Further manual segmentation was performed to select the hyperintense regions found within these brains because they correspond to the presence of cerebrospinal fluid in the ventricles of the brain and the lesions in the white matter (Figure 3.21 (c-d)). As previously mentioned for T_2-weighted image contrast, tissues with long T_2 gives higher signal intensities than short T_2 and therefore produce a brighter appearance.

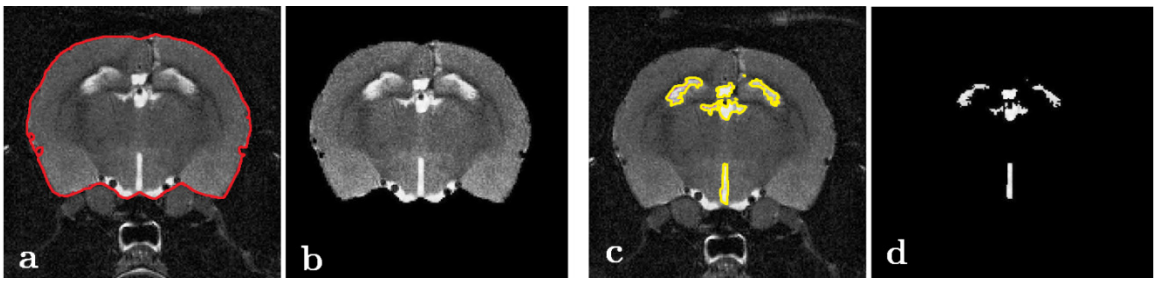

Figure 3.21: Manual segmentation of brain and ventricles using AMIRA. (a) Axial image of the brain with region highlighted (red) to segment the brain from the rest of the anatomy. (b) The mask of the brain segmented from the rest of anatomy. (c) Axial image with the region highlighting (yellow) the ventricles which were manually segmented. (d) The mask of the ventricles segmented from the rest of anatomy.

The threshold or border of the brain and the ventricles were visually determined for each slice of the brain with the aid of a rat brain atlas [79]. Each brain slice (7 per set) was manually segmented by hand using pixel selection. The ventricle regions that were segmented were the lateral ventricle (LV), dorsal third ventricle (D3V), and the third ventricle (3D), as shown in Figure 3.22, and these regions were evaluated as a whole.

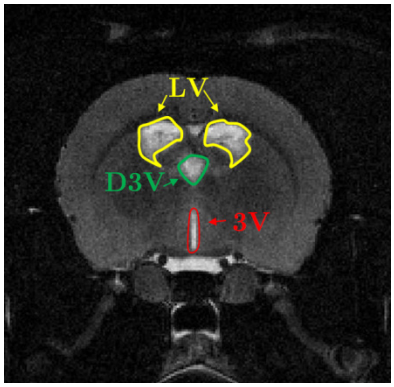

Figure 3.22: Segmented ventricle regions: the lateral ventricle (LV), dorsal third ventricle (D3V), and the third ventricle (3D).

Voxel counting of the masks obtained in segmentation was used to determine the volume sizes of the brain and the ventricles. The sum of each pixel selected was multiplied by the spatial resolution to obtain the volume. In the case for these brain images, the spatial resolution is 0.117 mm. The volume sizes that were obtained were: segmented brain volume (including ventricles), segmented ventricle volume, and segmented brain volume (not including ventricles). Note that the volume of brain without the ventricles was calculated from the subtraction of obtained volumes of the segmented brain from the segmented ventricles.

3.8 Statistical Analysis

In the *in vivo* study, seven image slices were obtained for each rat, with the exception of two rats where mistakenly only 6 image slices were obtained and will be explained in Section 4.1. To account for the error of these rats, the ventricle volume was calculated as a percentage of total brain volume. Statistics was performed on the *in vivo* brain data with the use of SAS® version 9.2. Analysis of variance (ANOVA) was run to test the effect of ventricle volume (as a percentage of total brain volume) on diet and surgery. Assuming that the data being analyzed was unbalanced, ANOVA was performed using the General Linear Model (GLM) procedure in SAS® as this procedure would work for both balanced and unbalanced data, as opposed to the ANOVA procedure in SAS which only works for balanced data. In this GLM procedure, for cases where the equality of variances cannot be assumed, corrected p-values were used.

ANOVA was run to test the differences in the following: diet and surgery combined (two-way ANOVA), diet only (one-way ANOVA), and surgery only (one-way ANOVA). If any significant differences between subjects from this analysis were found, Duncan's multiple range post-hoc tests were used to test for significance.

For the *ex vivo* livers, the means and standard deviations were calculated for the ratio of fat to water peak. Comparing the HFSCS and REG diets was done by performing independent sample t-tests.

4 Results

4.1 *In Vivo* Results

Example slices from each of the 6 rat groups are shown Figure 4.1 with the images of the original T_2-weighted image, segmented brain and ventricles, as well as the brain image without the ventricles. These images were obtained at 9 weeks post-surgery.

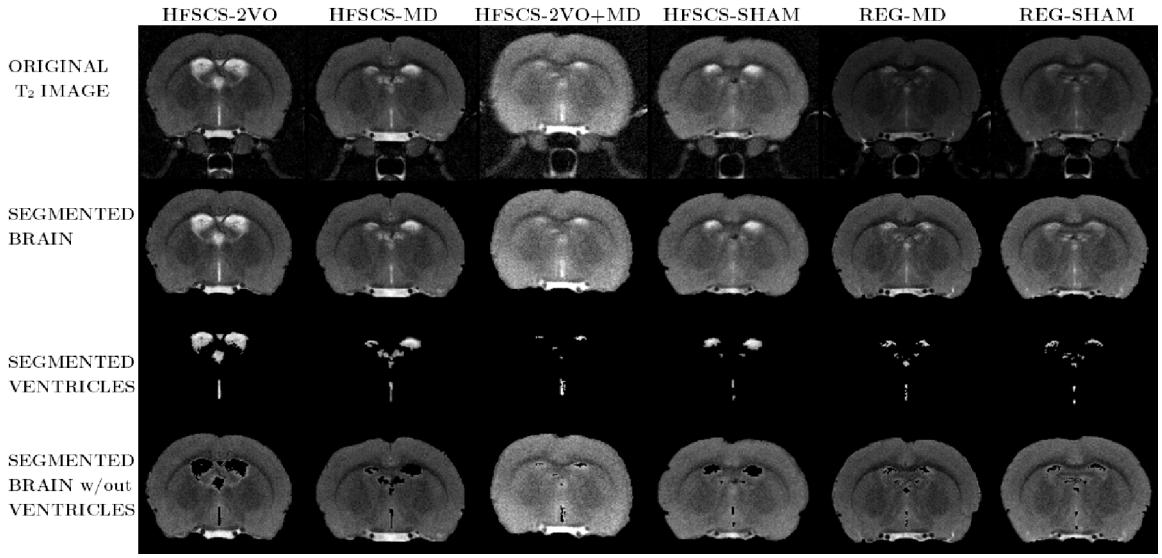

Figure 4.1: Representative T_2 image slice from each rat group, and the segmented masks (volumes) of the brain, ventricle, and brain without ventricles.

Based on the visual assessment of the *in vivo* images, there appeared to be no obvious differences between any of the diet and surgery groups. The only obvious differences were found in two cases (rats 4608 and 4629) which showed significant white matter damage and large ventricle volumes (Figure 4.2) that was not representative of the effects of covert stroke. Both of these rats were fed the HFSCS diet, where rat 4608 received only the MD

surgery (HFSCS-MD group), rat 4629 received only the 2-VO surgery (HFSCS-2VO group). These two cases were omitted from statistical analysis because they were obvious outliers and the abnormalities found in these rats could imply an actual stroke instead of a covert stroke. Because no imaging for any of the rats were taken pre-ischemia, comparison before and after surgery could not be performed to assess for any visual differences.

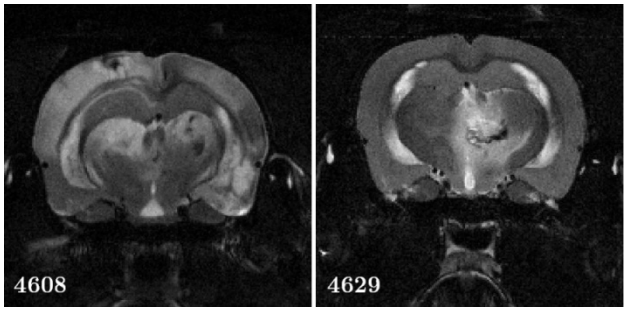

Figure 4.2: Two cases where significant brain damage was found. Rat 4608 belonged to the HFSCS-MD group, and rat 4629 belonged to the HFSCS-2VO group.

These ventricle volumes were studied in groups divided as diet with surgery (Section 4.1.1), diet only (Section 4.1.2), and surgery only (Section 4.1.3). Instead of using the total ventricle volumes as determined by pixel counting, ventricle volumes were calculated as a percentage of total brain volume as this was done in order to account for the mistake in two rats (one each from the REG-SHAM and REG-MD groups), where only 6 slices were imaged instead of the 7 slices that were acquired for all other rats. The reason for not taking the ventricle volumes as is for these two rats was because the slices were not lined up the same when compared to the rats that were imaged with 7 slices, and would mean that the slices that were selected would be different.

Table 4.1 shows the descriptive statistics for the rat groups on ventricle volume (as a percentage of brain volume) and are expressed in the form (mean ± standard deviation)%. The ventricle volume ranged from (0.68 to 4.65)% with an overall mean from all the rodent groups (diet & surgery combined) of (2 ± 1)%. When looking at surgery only, the ventricle volume of the surgeries were: 2VO (1.2 ± 0.3)%, 2VO+MD (2 ± 1)%, MD (2 ± 1)%, and SHAM (1 ± 1)%. When looking at diet only, the ventricle volumes were: HFSCS (2 ±1.1)%, and REG (1.3 ± 0.5)%.

Table 4.1: Descriptive statistics of ventricle and brain volume, and ventricle volume as a percentage of brain volume. Rats were grouped according to their type of diet and surgery. All values are listed as (mean ± SD), with the exception of minimum and maximum values. The * indicates that values in these two rat groups were skewed because one rat from these groups (REG-MD & REG-SHAM) were imaged taking only 6 slices instead of the 7 slices as for all other rats, and therefore only the percent volume was used in statistical analysis.

RAT GROUP	**NO. PER GROUP**	**SEGMENTED VENTRICLE (mm^3)**	**SEGMENTED BRAIN (mm^3)**	**VENTRICLE VOLUME (AS % OF BRAIN)**	**MIN (%)**	**MAX (%)**
HFSCS-2VO	11	9 ± 2	765 ± 25	1.2 ± 0.3	0.72	1.77
HFSCS-2VO+MD	6	15 ± 11	746 ± 15	2 ± 1	0.68	4.65
HFSCS-MD	14	15 ± 9	759 ± 29	2 ± 1	0.88	4.53
HFSCS-SHAM	13	12 ± 6	757 ± 19	2 ± 1	0.69	2.99
* REG-MD	6	10 ± 4	730 ± 48	1.4 ± 0.6	0.88	3.06
* REG-SHAM	12	10 ± 3	747 ± 58	1.3 ± 0.4	0.93	1.81
TOTAL	62	12 ± 7	752 ± 35	2 ± 1	0.68	4.65
Grouped by SURGERY						
2VO	11	9 ± 2	765 ± 25	1.2 ± 0.3	0.72	1.77
2VO+MD	6	15 ± 11	746 ± 15	2 ± 1	0.68	4.65
* MD	25	13 ± 8	745 ± 41	2 ± 1	0.88	5.70
* SHAM	19	11 ± 5	754 ± 35	1 ± 1	0.69	2.99
Grouped by DIET						
HFSCS	43	13 ± 8	758 ± 23	2 ± 1	0.68	5.70
* REG	18	10 ± 4	736 ± 51	1.3 ± 0.5	0.88	3.06

One-way and two-way analysis of variance (ANOVA) was conducted on how ventricle volume is affected by diet, surgery, and both combined. All values were compared to the threshold value of alpha 0.05, where any p-values less than 0.05 would be statistically significant.

4.1.1 Diet and Surgery

Two-way ANOVA showed that the overall effect on ventricle volume by diet, surgery and the interaction between diet and surgery were not statistically significant [$F(5, 56) = 2.3$, $p=0.06 > 0.05$], and shown in Figure 4.3. Furthermore, the effect due to the interaction between diet and surgery on ventricle volume was not statistically significant [$F(1,56)=0.3$, $p=0.6$], indicating that the effect of diet does not depend on the effect of surgery (or vice versa) in affecting the ventricle volumes. Testing on the individual effects on ventricle volume also show that the effect of diet alone was statistically non-significant [$F(1,56)=1.9$, $p=0.2 > 0.05$], however surgery alone was found to be statistically significant [$F(3,56)=2.9$, $p=0.04$]. Based on these results, the effects of diet and surgery on the ventricle volume were tested further using one-way ANOVA to determine if diet alone or surgery alone has an effect on ventricle volume.

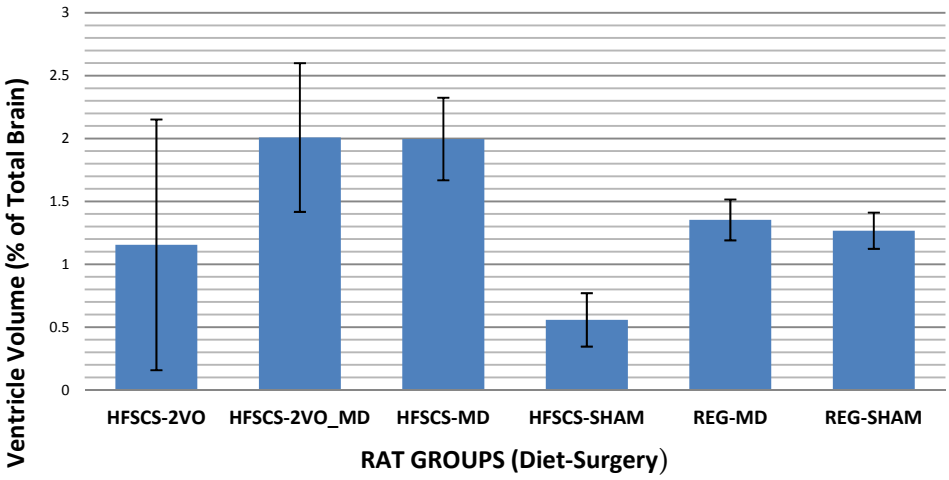

Figure 4.3: Histogram of mean ventricle volume (% brain volume) per rat group classified with both diet and surgery. Error bars are the standard error of the mean. All rat groups show overlap in the error bars to indicate statistical non-significance.

4.1.2 Diet

Although the results of Section 4.1.1 showed that diet analyzed alone was not statistically significant, one-way ANOVA was still performed on diet to not only verify this, but also to also see if there could be a potential difference between the HFSCS and REG diets. The one-way ANOVA conducted individually on HFSCS diet and on REG diet, showed there was a trend of larger ventricle volumes in HFSCS diets than REG diets (mean difference=0.4 $\pm$ 1.0 %). However, these results were non-significant as expected [$F(1,60)=2.2$, $p=0.2$]. One-way ANOVA conducted on diets separately also showed non-significance [HFSCS: $F(3, 39) = 1.9$, $p=0.2$; REG: $F(1,16) = 0.1$, $p=0.7$].

4.1.3 Surgery

The results from Section 4.1.1 as well as one-way ANOVA showed that the overall effect of surgery on ventricle volume was statistically significant [$F(3,58)=3.0$, $p=0.04$]. To further verify this, Duncan's multiple range post-hoc test also confirmed this statistical significance (with p-values <0.05) of the 2VO+MD surgeries between both 2VO and SHAM surgeries. This means that the rat group that received both surgeries (2VO and MD stroke) were statistically different from those rats that had only the 2VO surgery, as well as those rats that had the SHAM surgeries. All other comparisons of between surgeries however were not statistically significant, and this is shown in Figure 4.4 between the 2VO+MD surgery with 2VO as well as with SHAM surgery with the lack of overlap between the error bars (which represent the standard error of the mean). Overlaps exist between the MD surgery with the other three surgery groups.

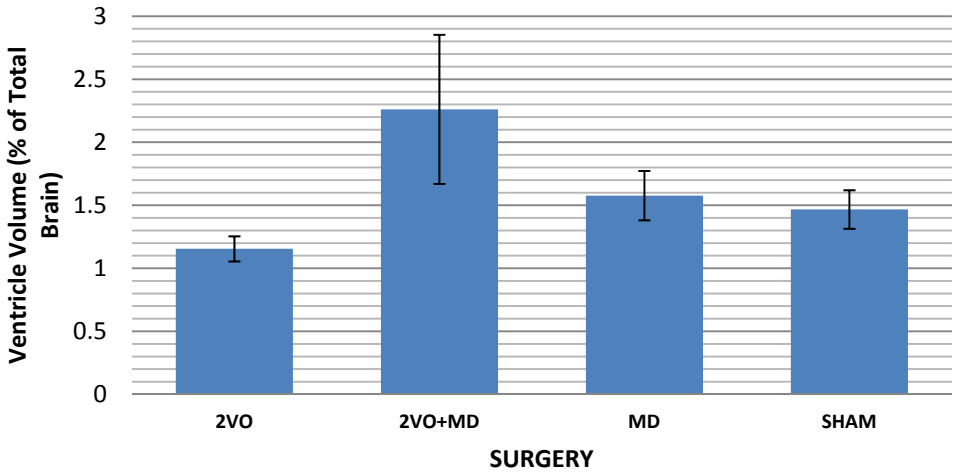

Figure 4.4: Histogram of mean ventricle volume (% brain volume) per rat group classified with surgery only. Error bars are standard error of the mean. Statistical significance is shown between 2VO+MD surgery with 2VO and SHAM surgery indicated by the lack of overlap of the error bars.

4.2 *Ex Vivo* Results

Table 4.2 shows the number of rats per group, where for each of these rats, the T_2-weighted axial image slices (30 slices for each rat) were visually assessed for possible abnormalities.

Table 4.2: *Ex vivo* rat groups and the number of rats assigned for each group.

RAT GROUP	N
HFSCS-2VO	3
HFSCS-2VO+MD	4
HFSCS-SHAM	2
REG-2VO	1
REG-SHAM	4
TOTAL	**14**

4.2.1 *Ex Vivo* Brains

Based on the *ex vivo* T_2-weighted brain images, abnormalities were found in some but not all of the rats. Only 3 slices of the total 420 slice images acquired (30 axial images for each of the 14 rats analyzed) corresponding to three different rats all belonging to the HFSCS-2VO+MD group are shown in Figure 4.5. This group of rats were fed the high fat, salt, sugar, and cholesterol diet and were subjected to both the bilateral vessel occlusion (which reduces blood flow) as well as the ET-1 injections which induced the stroke. These abnormalities were located in the medial aspect of the dorsal hippocampus (red circle) and mediodorsal thalamus (blue circle). It was expected that these would be the regions that would produce the abnormalities because this was the area where the

stroke were induced. Similar to the *in vivo* study, no imaging pre-ischemia was taken of these rats for the *ex vivo* study, therefore a comparison before and after surgery could not be performed to assess for any visual differences.

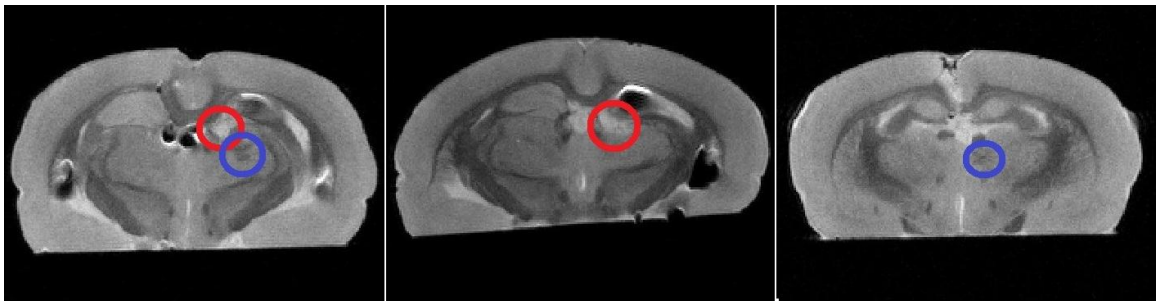

Figure 4.5: Abnormalities (circled) were detected in the medial aspect of the dorsal hippocampus (RED) and the mediodorsal thalamus (BLUE) on rats fed the HFSCS diet.

4.2.2 *Ex Vivo* Livers

Examples of image and spectra of the HFSCS diet and REG diet are shown in Figures 4.6 and 4.7. From these images, it was deduced that the liver on the HFSCS diet had higher fat content because the liver image shows more marbling and also the chemical shift artefact that can be seen along the top edge of the liver. The bright spots on the image are the bile ducts and blood vessels. The other peaks shown in the spectra between the water and fat peaks correspond to proteins in the brain.

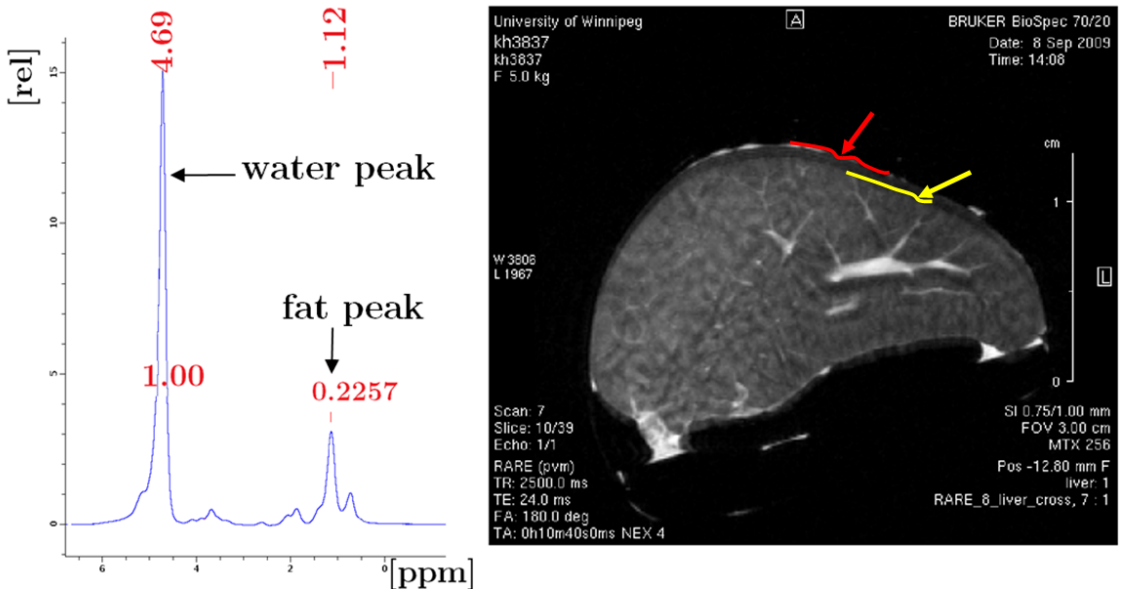

Figure 4.6: Image and spectra of liver from HFSCS diet group. A chemical shift artefact can be seen along the top edge of the liver. The red line indicates the top fat edge of the liver, and the yellow line shows the top water edge of the liver. Fat and water peaks are indicated by arrow. Horizontal values correspond to the percent area of the water and fat peaks. Vertical values correspond to the location of the water peak (~4.7 ppm) and fat/CH_2 peak (~ 1.1 ppm)

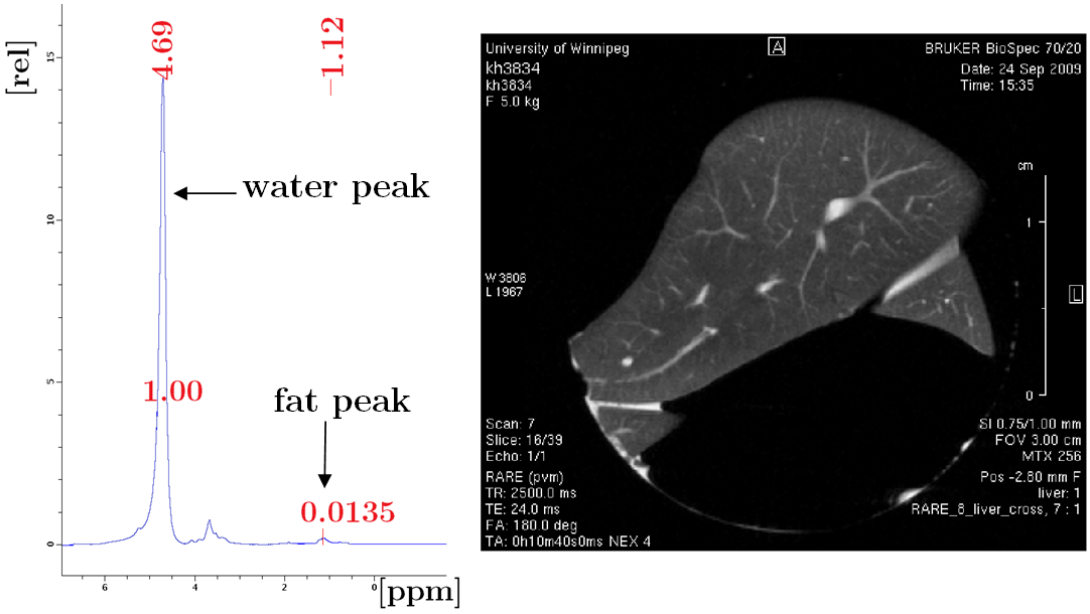

Figure 4.7: Image and spectra of liver from REG diet group. Fat and water peaks are indicated by arrow. Horizontal values correspond to the percent area of the water and fat peaks. Vertical values correspond to the location of the water peak (~4.7 ppm) and fat/CH_2 peak (~ 1.1 ppm).

Table 4.3 shows descriptive statistics on the HFSCS and REG diets where the ratio of fat to water peak (percent area) was calculated and expressed in the form of (mean ± standard deviation). The percent area integrated under the fat peak relative to water peak ranged from (0.5 to 26)% between both the diets in the two regions of interest. The spectra clearly showed an increase in fat content for rats fed on the HFSCS diet with noticeably higher fat peaks as can be seen in the spectra of Figures 4.6 and 4.7. The calculated average percent area of the HFSCS diet was (20 ± 4)%, and (2 ± 2)% for the normal diet, which is about a nine-fold difference.

Table 4.3: Descriptive statistics on the percent area of the fat peak relative to water peak as expressed in the form (mean ± SD) %.

DIET	ROI #1	ROI #2	AVERAGE OF ROI #1 & ROI #2	MIN	MAX
HFSCS	20 ± 4	20 ± 5	20 ± 4	12	26
REG	3 ± 3	2 ± 2	2 ± 2	0.5	9.4
OVERALL	9 ± 9	9 ± 9	9 ± 9	0.5	26

A two-tailed independent sample t-test was performed to compare the differences between the HFSCS and REG diets. The t-test showed that the mean difference was statistically significant ($t = 12$, with degree of freedom = 17, $p < 0.0001$), which indicates evidence exists that the percentage area for HFSCS diet is larger than the REG diet, with a mean difference of (18 ± 3)%.

4.3 Behavioural Testing

Behavioural testing was performed at Memorial University [80]. They determined that rats that received both the bilateral occlusion and the induction of the lacunar infarcts (2VO+MD group) and rats with the induced lacunar infarcts alone (MD group) exhibited a selective impairment in the ability to perform an extra-dimensional (ED) attention shift, but this effect was not observed in rats with 2-VO or sham surgery alone [80]. Furthermore, there were no differences in either the intra-dimensional (ID) attention set shift or the reversal tests among these groups which indicates a selective ED set-shifting deficit [80].

Aged rats on a HFSS diet with both the surgeries (HFSCS-2VO+MD) and rats with an MD stroke alone (HFSCS-MD) exhibited a selective impairment in the ability to perform an ED attention shift that required a response to a stimulus in a novel stimulus dimension. Young rats on a regular chow diet were similarly impaired on the ED shift following a bilateral medial prefrontal cortex stroke, however a bilateral MD stroke (2VO+MD group) did not produce an attention shift impairment [80].

5 Discussion

The aim of this thesis was to determine if MRI and MRS done both *in vivo* and *ex vivo* are sensitive enough of a modality to detect any changes in brain morphology, lesion development ultimately to confirm that this new rodent model will have the desired anatomical and behavioural effects usually shown in covert stroke models. With the use of MRI and MRS, we were able to assess the data obtained from the different diet and surgery groups of this rodent model. From the results of the *in vivo* T_2 –weighted brain image analysis, visual assessment could not conclude if there were any differences between these groups. One reason is due to the varying ventricle sizes, as evidenced by my own experiences in assessing these images, as well as shown in other studies [81-84]. Also, there were no images taken of these rodents pre-ischemia therefore tracking the change in brain and ventricle volumes could not be studied, because a baseline for each rat could not be set. Further analysis of these *in vivo* images involved developing a segmentation method that enabled the brain to be manually segmented from the rest of the anatomy, as well as further segmentation of the bright regions in the brains, corresponding to the presence of cerebral-spinal fluid (CSF) in the ventricles of the brain and lesions in the white matter. The reason for obtaining volumes of both the brain and ventricles was to assess or detect any changes in brain morphology; to determine if the brain volume decreased and ventricle volume increased for this rodent model. From the *ex vivo* T_2 –weighted brain images, abnormalities were detected for rats who had the 2-vessel occlusion and the lacunar

infarcts induced in the MD and also were fed the HFSCS diet (HFSCS-2VO+MD group). No other abnormalities were detected in the other rodent groups. This could be because the volume changes due to surgery and diet are smaller than the natural variations between animals. No pre-ischemia images were taken on these rodents that could be used to compare the brain before and after so an assessment could not be made. *Ex vivo* liver images and spectra were assessed and were able to detect the effects of diet on this rodent model.

5.1 *In Vivo* Study

In vivo images were acquired nine weeks after surgery. Based on the visual assessment of the images, no major differences were obvious between the groups, and changes within each animal could not be studied because images before the surgery were not acquired.

5.1.1 Ventricle Volumes

Further analysis was performed on these T_2 –weighted images by determining whether the ventricle volumes as a percentage of brain volume were affected by the different rat groups. Determining the brain and ventricle volumes is important because when a stroke occurs, brain tissue in the region of the stroke is said to atrophy or die, causing the ventricle region to appear as if it is expanding as it fills with CSF. Ventricle and lesion

size are important for the development of this model as it allows us to see if it properly mimics the effects of covert stroke.

Comparing the ventricle volumes between the groups showed that there was no significant difference between diet and surgery combined, as well as in diet only. There was however a significant difference in ventricle volumes between surgery and Duncan's post-hoc test showed significant difference between rats of the 2VO+MD group to both the MD and SHAM groups only. The significant effect of the surgery (white matter changes) is in agreement with prior studies [85]. Further comparison on the diets where one-way ANOVA was conducted individually on the diets showed a trend that there were larger ventricle volumes in HFSCS diets than REG diets.

The unexpected non-significance of the effects of diet on ventricle volume could be attributed to the small sample size, as well as the fact that MRIs were not taken of rats on REG diet from all surgery groups. The only MRIs taken of rats from with the REG diet were those with MD and SHAM surgeries. The variation in the number of rats per group was dependent on what was received from the Corbett group at MUN, and also for the fact there was a high mortality rate for these rats due to the type of surgeries performed, as well as they were required to travel to Winnipeg from Newfoundland for the MR analysis, and those rats were not imaged for the *in vivo* study. The small sample size could also explain why not all surgeries showed any significant differences. Increasing the number of rats per diet and surgery group could contribute to a more robust analysis.

Alternatively, this non-significance in our results could also be because our expected difference is not correct and therefore the model we are investigating may not be a suitable model for covert stroke.

Slice-by-slice image analysis could also be performed where slices need to be selected such that the region of interest is consistent for all images acquired. Continuing on that, it may be worthwhile to look at the ventricles separately (as per Figure 3.21) to see how the volumes for each can be affected by diet and surgery groups.

Another reason could be the variability of the manual segmentation that was performed on the brain and ventricles to obtain the volumes, which will be further discussed in Section 5.1.2. This could be a technical error, as manual segmentation was performed only once on each rat sample and therefore repeated measurements could improve the statistical results.

5.1.2 Segmentation

A segmentation method using AMIRA® and Matlab software was developed to determine the volumes of the brain and ventricles. This method allowed for the manual segmentation of the brain from the rest of the anatomy. Further segmentation was performed within these brain regions by selecting the bright regions which correspond ventricles in the brain. In these T_2 –weighted images, ventricles appear bright due to the

presence of cerebrospinal fluid (CSF), where a higher concentration of hydrogen nuclei exists. This manual segmentation allowed for the ventricle volumes to be calculated so that the effects of diet and surgery on ventricle volume could be assessed (Section 4.1, 5.1.1). Limitations to the manual segmentation are time, lack of familiarity with anatomy, as well as the limited resolution and contrast of the images obtained. Each of these limitations will be discussed.

Manual segmentation was performed slice-by-slice with a total of 7 slices for each of the groups for a total of 62 rats in this thesis. On average segmentation took about 45 minutes to perform per rat once a routine was established. Thus user exhaustion and lack of focus could have attributed to the errors in the calculation of the ventricle volumes.

The lack of familiarity of recognizing the ventricles in the brain even with the aid of a rat atlas could account for the relatively large standard deviations calculated for ventricle volumes. This can be remedied by having more familiarity with the anatomy of the brain, as well as having another person perform segmentation independently using a consistent segmentation technique to help with the human error.

The difficulty in distinguishing anatomy can be attributed to the limited resolution and the contrast of the images at the edges. Distinguishing parts of the brain from the ventricles can be hard to see visually. Also, pixels along the edges of the structure could be partially ventricle and partially brain tissue due to the partial volume effect, making assignment to a particular tissue type difficult.

Adjusting the parameters to obtain better resolution and contrast involves increasing the time needed for the animal to be in the scanner. Image resolution can be improved through collecting more averages for imaging but this would mean that imaging would take longer. Longer imaging times however can cause stress on the animal because it would require more time under anesthesia, making these long imaging sessions inhumane. This stress can also lead to premature death, increasing the number of animals needed in the study. Also imaging costs for long imaging sessions with so many animals prohibit these types of studies.

One solution to these limitations is to develop an automated segmentation method that can segment images of a certain resolution and contrast in an efficient time, and also have the ability to distinguish between the anatomy of the brain. Another solution is to develop more optimal image contrast.

5.2 Semi-automated Segmentation Method

Fully automated segmentation can be much faster and less user-biased than manual segmentation. Thus a method was developed which selected a certain threshold of percentage of maximum brightness in the brain in an attempt to increase the speed of data processing. Selection of the threshold was done per slice in the rat brain. Thresholds varied between slices because the relative intensity of the ventricles would change depending on where the image slice was taken. For example, fat has a high intensity or is

hyperintense in the images so slices with high fat content had ventricles that appeared less intense in comparison. Also, the threshold would vary because of the location of the ventricle corresponding to the partial-volume effects. A voxel containing part of the ventricle and part of the brain tissue would appear hypointense compared to a voxel containing only brain tissue, i.e. the less ventricle in the image implies a more hypointense voxel.

This threshold method was tested on the brain data of one rat, using three different cases: (1) using the original T_2 –weighted image of the brain as taken from the MRI, (2) using the brain data previously segmented manually, and (3) using the segmented brain data with further manual segmentation removing the optic tract. This threshold method was performed in three ways because simple threshold segmentation would include the brightness as ventricles both within the brain as well as in the surrounding anatomy. Selecting a particular threshold of brightness may result in the inclusion of areas surrounding the brain because some of the regions outside the brain, e.g. fat, are hyperintense in the original T_2 –weighted image. To improve this automated segmentation, the previously manually segmented brain data were used so that wrap-around artefacts and corresponding hyperintense non-brain regions of the original T_2–weighted image were eliminated and so that the threshold selected would not include this region as ventricles in the segmentation. Using the same reasoning, removing the optic tract which appears very bright in the images would also change the result.

5.2.1 Comparing Manual to Semi-automated Segmentation

Comparison of the semi-automated threshold method to the manual method was conducted using two methods. The first method examined the difference in intensity counts between the ventricle masks of manual versus semi-automated methods, and then the intensities for each pixel in the resulting difference image were summed. The second method used the kappa index [71,86-88].

5.2.2 Difference in Intensity Counts

Examples of an image showing the difference in intensity counts between the two segmentation methods is shown in Figures 5.1. This figure represents the case where the threshold segmentation was performed using the manually segmented brain.

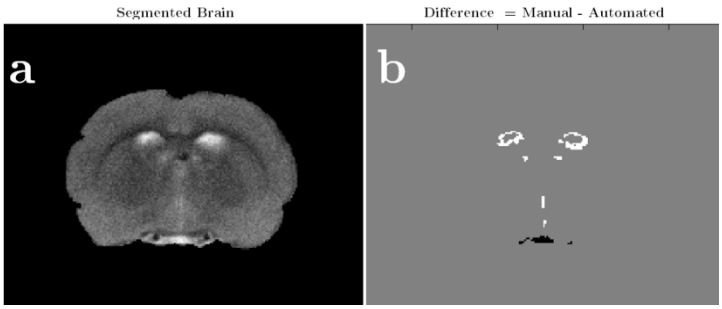

Figure 5.1: Difference in intensity counts between manual and automated segmentation methods. (a) Segmented brain mask used in the comparison of the manual and automated methods. (b) Difference image indicating overlap (grey regions) and no overlap (where black regions classified as ventricles in the automated method, and white regions classified as ventricles in the manual method).

The black region in this difference image indicates no overlap, i.e. what was included in the automated threshold image was not include in the manual method. In this particular figure, the black region in the difference image indicates that the threshold method selected the optic tract, which was not selected in the manual method.

The white region in the difference image also indicates no overlap, i.e. what was included in the manual method was not included in the automated threshold. Here, this figure shows that the manual method took more of the ventricle than the threshold method.

The grey region shows that an overlap exists between the two segmentation methods, i.e. both methods agreed as to the classification of the tissue. Table 5.1 summarizes the regions of the difference image as shown in (Figure 5.1 (b)).

Table 5.1: Description of the regions on the difference image comparing manual and automated segmentation methods.

Region	Description
Black	Shows voxels that were included as ventricles in the Automated method but not included in the Manual method.
White	Shows voxels that were included as ventricles in the Manual method but not included in the Automated method.
Grey	Shows both methods are in agreement as to the classification of a voxel.

The difference in intensity counts was tested on the three cases where the threshold method was used: original T_2 –weighted image (Figure 5.2), manually segmented brain image (Figure 5.3), and manually segmented brain image not including the optic tract

(Figure 5.4). All thresholds were set at 70% for these figures for consistency and also to show the differences between the three cases and the manually segmented ventricles.

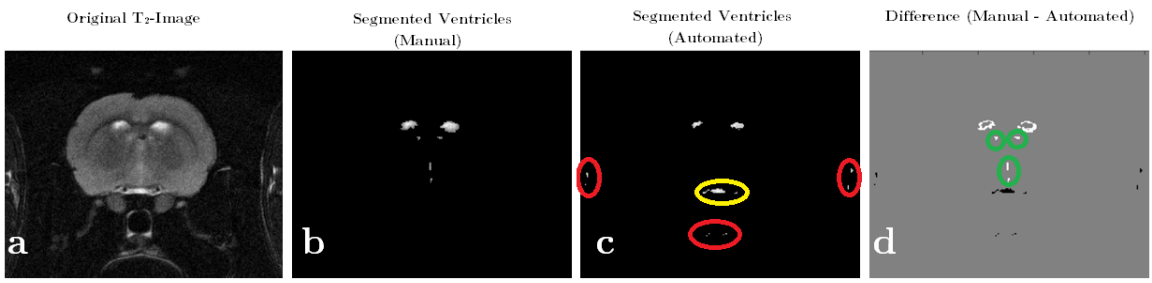

Figure 5.2: (a) Original T_2 –weighted image. (b) Manually segmented ventricles used for comparison between the segmentation methods. (c) Threshold segmentation set at 70%. (d) Difference image between the two segmentation methods. The areas circled show the regions that the automated segmentation included as ventricles.

Using the original T_2 –weighted image (Figure 5.2) the threshold method for segmenting the ventricles included some regions outside of the brain such as the wrap-around artefact on the left and right of the image (circled in red, Figure 5.2 c), as well as a portion of the optic tract (circled in yellow, Figure 5.2 c). The resulting difference image shows these regions in black (optic tract and non-brain regions). The threshold method also did not include the dorsal third ventricle and third ventricle which are shown in white on the difference image (circled in green, Figure 5.3 d). The grey areas show where the methods agreed as to the classification of tissues (Figure 5.3 d). To determine if removing the unwanted areas in the image would affect the threshold method in selecting ventricle regions, it was also applied to the other two cases: manually segmented brain, with and without the optic tract (Figures 5.3 and 5.4, respectively).

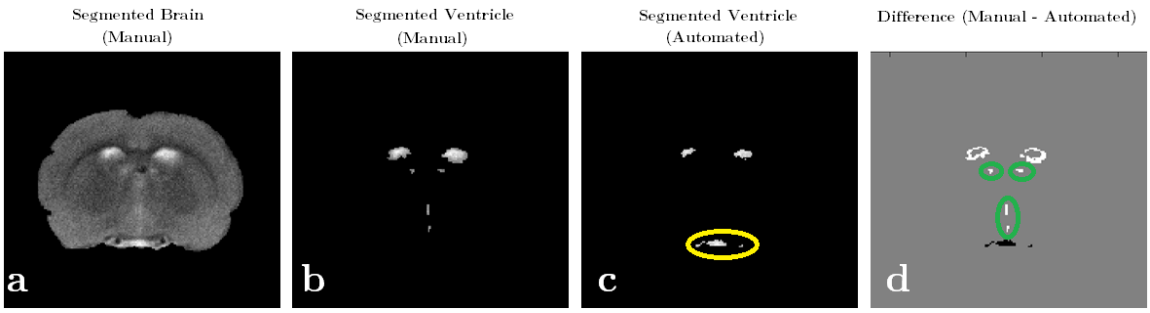

Figure 5.3: (a) Manually segmented brain image. (b) Manually segmented ventricles used for comparison between the segmentation methods. (c) Threshold segmentation set at 70%. (d) Difference image between the two segmentation methods. The areas circled show the regions where the segmentations method differed.

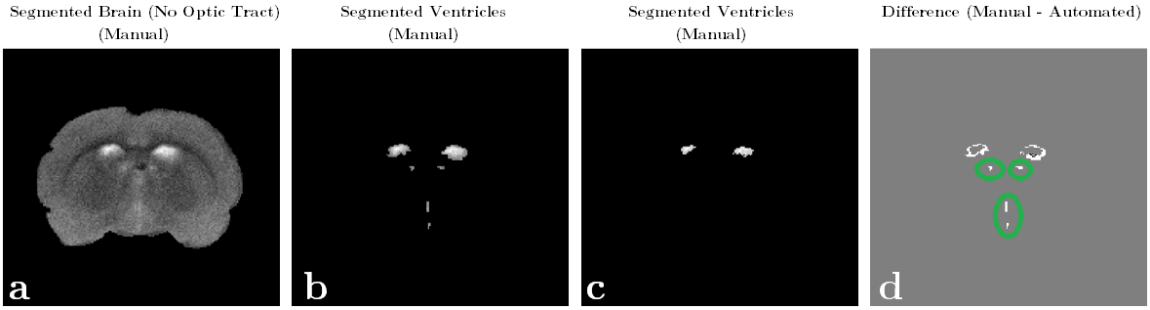

Figure 5.4: (a) Manually segmented brain image excluding the optic tract. (b) Manually segmented ventricles used for comparison between the segmentation methods. (c) Threshold segmentation set at 70%. (d) Difference image between the two segmentation methods. The areas circled show the regions where the segmentations method differed.

Similar to the results when using the original T_2 –weighted image, the threshold method also included regions that were not ventricle but rather a portion of the optic tract (circled in yellow, Figure 5.3 c), and excluded the dorsal third ventricle and third ventricle (circled in green, Figures 5.3 and 5.4, part d). Using the same threshold value of 70% for all three cases shows that adjustments to this value need to be made in order to select the desired

regions of interest. Also, threshold values will need to be adjusted slice-by-slice because ventricles in the T_2 –weighted image vary in relative brightness.

Evaluating one slice at a time, multiple threshold values were tested. The best threshold value was chosen as the one that segmented most of the ventricle region even if other regions were also segmented. The decision to accept this threshold value was made to ensure that the ventricles were included, instead of choosing a higher threshold value that not only omitted regions outside of interest but also omitted regions of the ventricle that were required. For example, using the image of a segmented brain (Figure 5.3 a), the following thresholds were obtained for this slice (Figure 5.5). These threshold values were then compared to the manually segmented ventricles.

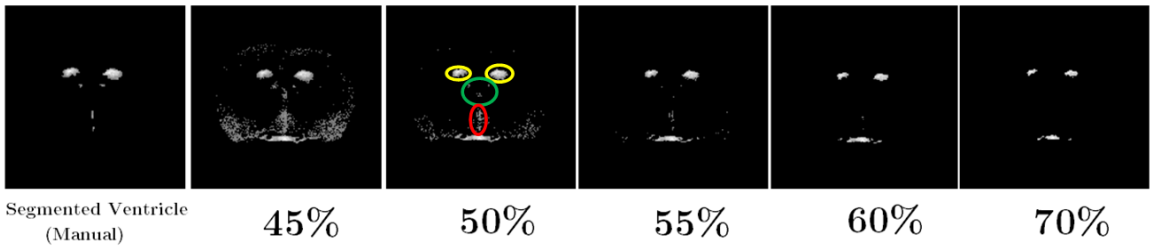

Figure 5.5: Manually segmented ventricle and the thresholds at 45, 50, 55, 60 and 70%. Increasing the threshold value removes the undesired regions of the brain, but also removes ventricle the higher the threshold gets.

From Figure 5.5, the threshold of 50 % was selected to be the visual 'best' of the other thresholds. Although this threshold selected more of the other regions that were not required (e.g. optic tract), it also did select more of the ventricles, i.e. the lateral ventricles (yellow circles), dorsal third ventricle (green circle), and third ventricle (red circle). This

threshold was chosen over the threshold of 70% because even though 70% did select less of the optic tract, it also selected less of the ventricle.

When comparing this automated method to the manual method, it was more time consuming to look at increments of threshold values, determining which of these values selected most of the ventricles, as well as removing the regions outside of the brain to reduce the chance of these thresholds values would include it as ventricle. Therefore a more automated approach to selecting threshold was desired.

5.2.3 Kappa Index

The kappa index represents the ratio of the number of overlapping voxels between the manual and semi-automated segmentation to the total number of voxels from both methods, and is given as

$$\mathrm{K} = \frac{2\,(V_A \cap V_M)}{V_A + V_M} \quad , \tag{5.95}$$

where V_A is the volume of the automated method and V_M is the volume of the manual method [71,86-88]. An explanation of how the kappa index is obtained can be shown in Figure 5.6.

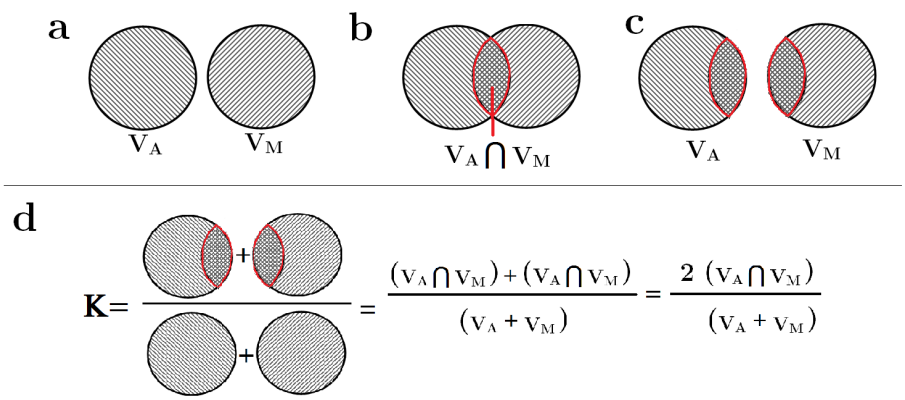

Figure 5.6: Kappa index. (a) V_A and V_M are the volumes of the automated and manual methods, respectively. (b) The highlighted region in red shows the intersection of both methods, i.e. $V_A \cap V_M$. (c) V_A and V_M will each contain $(V_A \cap V_M)$ pixels. (d) Kappa index is the sum of the intersected volumes for V_A and V_M (from c), divided by the total volumes of V_A and V_M.

Using the kappa index, values greater than 0.7 would indicate an accurate automated segmentation [71,86-88]. An index of 1.0 would indicate full overlap of the two images whereas an index of 0.0 would indicate no overlap.

As discussed in Section 5.2.2, the semi-automated segmentation method selected a specific threshold value for each slice in image set, wherein the 'best' threshold per slice was used. The best threshold was determined visually with the difference images, however another way that was used in determining which threshold selected most of the ventricle was to take the threshold value which had the highest kappa value when compared to the manually segmented ventricle slice per each slice. This was done assuming that the higher kappa value implied that the threshold selected would be more accurate, than one with a lower kappa value.

These two methods of selecting the best threshold values were then compared by again using the kappa value to determine which method of selection would have a higher kappa value. Table 5.2 outlines the thresholds obtained for these two methods on all three cases of images used. Threshold values that were determined to be the "best" in selecting ventricles in each method are listed, along with the kappa values collected when comparing the two methods with the manual segmented method.

Table 5.2: Comparison of the selected threshold values using the kappa index. The threshold values determined as 'best' per slice are listed under the image used in the segmentation. The threshold is determined by the best (a) kappa values and (b) difference images.

Image Used	**Kappa Values**							
	Slice 1	**Slice 2**	**Slice 3**	**Slice 4**	**Slice 5**	**Slice 6**	**Slice 7**	**TOTAL**
Original T2 image								
(a) {0.58, 0.54, 0.66, 0.65, 0.55, 0.48, 0.49}	0.19	0.56	0.41	0.13	0.53	0.49	0.35	0.38
(b) {0.58, 0.58, 0.57, 0.57, 0.53, 0.41, 0.49}	0.19	0.54	0.31	0.08	0.50	0.29	0.35	0.29
Segmented Brain								
(a) {0.58, 0.54, 0.79, 0.65, 0.55, 0.61, 0.66}	0.21	0.60	0.58	0.16	0.59	0.60	0.47	0.43
(b) {0.57, 0.54, 0.70, 0.57, 0.49, 0.52, 0.67}	0.19	0.60	0.44	0.09	0.45	0.33	0.47	0.33
Segmented Brain w/out Optic Tract								
(a) {0.66, 0.64, 0.75, 0.80, 0.57, 0.66, 0.71}	0.27	0.76	0.74	0.22	0.77	0.77	0.59	0.60
(b) {0.61, 0.67, 0.76, 0.67, 0.52, 0.56, 0.68}	0.25	0.73	0.72	0.11	0.62	0.38	0.58	0.39

The total kappa indices in Table 5.2 ranged between 0.29 to 0.60, which corresponds to some or to no overlap between the manual and semi-automated segmentation methods. This could be attributed to limitations of the manual segmentation of the ventricles, as discussed in 5.1.2, but another reason could be that the threshold values selected were not specific enough in segmenting the ventricles. Possibly varying thresholds in different areas in the image would successfully segment the ventricles. The brightness varies depending

on how much of the ventricle is included in the volume being imaged, and similar to the reasoning for the limitations to the manual segmentation, user familiarity of the anatomy, resolution and contrast between the anatomy of the brain need to improve in order to use this automated method.

The reason for testing out this 'automatic' method was to find an easier way to segment the images without having to do each slice separately as well as reduce human error by removing user bias. However in order for this method to work in obtaining the thresholds, manual selection needed to be done, and in the case of the kappa index, full manual segmentation needed to be done. This also proved to be time consuming as each threshold would need to be evaluated, both with the use of difference images and kappa values, in increments of 10% and in some cases in increments of 1%.

5.3 *Ex Vivo* Study

Ex vivo images were acquired on the excised brains and livers. Brain imaging showed some abnormalities were found only rats from the HFSCS-2VO+MD group, and located at the site where induction of the stroke took place. Liver imaging showed the difference between the HFSCS and REG livers. Images showed chemical shift, for those rats fed an HFSCS diet. Spectra obtained showed fat-to-water peaks significantly higher in HFSCS rats than REG rats. Integration of the areas under the fat peak relative to the water peak

showed an 9-fold difference between the two diets. Statistical analysis confirmed this difference significantly.

5.3.1 *Ex Vivo* Brain

Based on the *ex vivo* brain images, abnormalities were found in some, but not all rats from the HFSCS-2VO+MD group, which were the rats that were fed a diet high fat, salt, sugar, and cholesterol and were subjected to both the bilateral vessel occlusion (which reduces blood flow) as well as the ET-1 injections (which induced the stroke). These abnormalities were found in the region where the stroke was induced; in the medial aspect of the dorsal hippocampus and mediodorsal thalamus, which are two regions in the brain that are both important for learning and memory.

5.3.2 *Ex Vivo* Liver

MR Spectroscopy measurements showed a nine-fold increase in fat content in the livers of rats fed the HFSCS diet when compared to those on the REG diet. These results corresponded to the visual assessment of the liver images where the HFSCS diet had the appearance of marbling, compared to the livers of rats on a REG diet. Based on statistical analysis, there is strong evidence that exists that the livers of rats fed the HFSCS diet have significantly larger fat to water ratio than the livers of rats fed the REG diet.

5.4 Behavioural Analysis

Behavioural analysis indicated more significant differences than the MRI in anatomical detected differences. More sophisticated MRI techniques, or pre- and post-surgery imaging are needed to increase the sensitivity of MRI. These results indicate that age and diet play an instrumental role in the development of executive dysfunction following covert stroke. These effects reflect several key neurobiological features of covert stroke including diet-induced hypertension and are consistent with a selective attention set-shifting impairment in humans in an analogous cognitive test. They demonstrate for the first time the feasibility of an animal model that accurately reflects the neurobiological and clinical features of covert stroke. The areas of abnormalities see in the *ex vivo* MRI images correspond to the areas of the brain that are thought to be affected by performance in these tests.

6 Conclusions

Although MRI is effective in viewing the brain, it is limited in the resolution and in the contrast of the image. Adjusting the parameters to obtain better resolution and contrast would increase the time that a living subject would need to be in the scanner causing more discomfort to the subject and in the case of infants and animals, causing an increase in anesthesia time. Small sample size, imaging performed at different stages of diet and surgery, lack of familiarity of recognizing the ventricles in the brain even with the aid of a rat atlas were all compound factors in the analysis and conclusions which could be drawn from the data. Rodents exhibited a selective impairment in attention set shifting that is consistent with cognitive impairments in humans following covert stroke. In addition, rodents exhibited diet-induced hypertension that is commonly associated with covert stroke. These results demonstrate for the first time the feasibility of an animal model that accurately reflects the clinical and neurobiological features of covert stroke.

Higher resolution anatomical images, slice-by-slice image analysis as well as a measure of blood flow can also be studied for more detailed anatomical information. Nonetheless, these results show that applying MRI and MRS is important in the development of this covert stroke rodent model and with more refinement of MRI techniques more information can be obtained. The custom diet results in the development of cardiovascular disease risk factors in rats and thereby provides a better approximation of human disease.

7 Future Studies

Higher resolution anatomical images, slice-by-slice image analysis as well as a measure of blood flow can also be studied for more detailed anatomical information. No pre-ischemia images were obtained for this data set because the rats were shipped to Winnipeg only for imaging post-surgery and therefore ventricle volumes could not be compared between pre- and post-surgery. This is a design flaw, because baselines could not be determined. Rat ventricle volumes vary considerably between animals so the percentage change in ventricle volume might have been a useful measure. Future experiments would involve rats being housed in Winnipeg for the entire study for surgery, behavioural analysis and imaging, so that any natural variations in ventricle sizes could be ascertained in advance.

An automated segmentation method could be created which would allow for accurate segmentation of the bright regions, as well as decrease the amount of time needed to perform segmentation on each rat being studied. This would require more sophisticated methods than used in this study. For example, the segmentation could be done by registering each image to an atlas and assigning regions based on the atlas. It would have also been useful to compare the left and right sides of the brain because a comparison could be done on the location of the induced stroke and to see how much brain tissue is affected.

List of Acronyms

2-VO	2-vessel occlusion/ bilateral occlusion
ANOVA	analysis of variance
CD	compound discrimination
CHESS	chemical shift selective
CNS	Central Nervous system
CSF	cerebrospinal fluid
ED	extra-dimensional
ET-1	Endothelin-1
ETL	echo train length
FID	Free Induction Decay
FOV	Field of view
^{1}H	Hydrogen atom
HFSCS	high in fat, salt, cholesterol and sugar diet
ID	intra-dimensional shift
LI	learned irrelevance
MD	mediodorsal thalamus
MRI	Magnetic Resonance Imaging
MRS	Magnetic Resonance Spectroscopy
M_z	Longitudinal magnetization
M_{xy}	Transverse magnetization
NMR	Nuclear Magnetic Resonance
PBS	Phosphate-buffered saline
PD	proton density

PFA	Paraformalydehyde
PRESS	point resolved spectroscopy
RARE	Rapid Acquisition with relaxation enhancement
REG	normal, control diet
REV	reversal
RF	radio-frequency
ROI	Region of Interest
SD	simple discrimination
SHAM	sham surgery
SNR	signal-to-noise ratio
STE	stimulated echo
STEAM	stimulated echo acquisition mode
$\mathbf{T_1}$	longitudinal relaxation time
$\mathbf{T_2}$	transverse relaxation time
TE	echo time
TM	mixing period
$\mathbf{V_A}$	volume of automated method
$\mathbf{V_M}$	volume of manual method
VCI	Vascular Cognitive Impairment

References

[1] Heart and Stroke Foundation of Canada. (2012) *Statistics.* Retrieved August, 2012from: http://www.heartandstroke.com/site/c.ikIQLcMWJtE/b.3483991/k.34A8/Statistics.htm

[2] Schmidt, W-P., Roesler, A., Kretzschmar, K, Ladwig, K-H., Junker, R., Berger, K. (2004) Functional and Cognitive Consequences of Silent Stroke Discovered Using Brain Magnetic Resonance Imaging in an Elderly Population. *Journal of the American Geriatrics.*52:1045–1050

[3] Fujishima, M., Yao, H., Terashi, A., Tagawa, K., Matsumoto, M. Hara, H., Akiguchi, I., Suzuki, K., Nishimaru, K., Udaka, F., Gyoten, T., Takeuchi, J., Hamada, R., Yoshida, Y., Ibayashi, S. (2000) Deep White Matter Lesions on MRI, and not silent brain infarcts are related to headache and dizziness of non-specific cause in non-stroke japanese subjects. *Internal Medicine* 39(9): 727-731

[4] Vermeer, S.E., Longstreth, W.T., Koudstaal, P.J. (2007) Silent brain infarcts: a systematic review. *Lancet neurology.* 6(7):611-619.

[5] Vermeer, S.E., Prins, N.D., den Heijer, T., Hofman, A., Koudstaal, P.J., Bretler, M.M. (2003) Silent brain infarcts and the risk of Dementia and cognitive decline. *N Engl J Med.* 348(13):1215-1222.

[6] Longstreth, W.T., Bernick, C., Manolio, T.A., Bryan, N., Jungreis, C.A., Price, T.R. (1998) Lacunar infarcts defined by magnetic resonance imaging of 3660 people: the Cardiovascular Health Study. *Arch Neurol.* 55(9):1217-25.

[7] Smith, E.E., Egorova, S., Blacker, D., Killiany, R.J., Muzikansky, A., Dickerson, B.C., Tanzi, R.E., Albert, M.S., Greenberg, S.M., Guttmann, C.R. (2008) Magnetic resonance imaging white matter hyperintensities and brain volume in the prediction of mild cognitive impairment and dementia. *Arch Neurol.*65(1): 94-100.

[8] Birrell, J.M., Brown,V.J. (2000) Medial Frontal Cortex Mediates Perceptual Attentional Set Shifting in the Rat. *J Neurosci.* 20(11):4320-4324.

[9] Stuss, D.T., Alexander, M.P. (2007) Is there a dysexecutive syndrome? *Philosophical transactions of the Royal Society of London.* **362**(1481):901-915.

[10] Fisher, C.M. (1982) Lacunar strokes and infarcts: a review. *Neurology* 32(8):871-876.

[11] Fisher, C.M. (1965) Lacunes: Small, deep infarcts. *Neurology.* 15:774-784

[12] Roman, G.C., Erkinjuntti, T., Wallin, A., Patoni, L., Chui, H.C. (2002) Subcortical ischaemic vascular dementia. *Lancet neurology.* 1(7): 426-36.

[13] Iadecola, C., Davisson, R.L. (2008) Hypertension and cerebrovascular dysfunction. *Cell metabolism.* 7(6): 476-84

[14] Hsu, Y.Y., Du, A.T., Schuff, N., Weiner, M. (2001) Magnetic Resonance Imaging and Magnetic Resonance Spectroscopy in Dementias. J Geriatr Psychiatry Neurol. 14:145-166.

[15] Heart and Stroke Foundation - Centre for Stroke Recovery. (2011) Scientific Bulletin August 2011. Retrieved August, 2012 from: http://centreforstrokerecovery.ca/wp-content/uploads/2011/09/Scientific-Bulletin-Aug-2012-Final.pdf

[16] Jokinen, H., Kalska, H., Mäntylä, R., Pohjasvaara, T., Ylikoski, R., Hietanen, M., Salonen, O., Kaste, M., Erkinjuntti, T. (2006) Cognitive profile of subcortical ischaemic vascular disease. *J NeurolNeurosurg Psychiatry*77(1):28-33.

[17] Debette, S., Bombois, S., Bruandet, A., Delbeuck, X., Lepoittevin, S., Delmaire, C., Leys, D., Pasquier, F. (2007) Subcortical hyperintensities are associated with cognitive decline in patients with mild cognitive impairment. *Stroke.* 38(11):2924-30.

[18] Masuda, J., Nabika, T., Notsu, Y. (2001) Silent Stroke: pathogenesis, genetic factors and clinical implications as a risk factor. *Current Opinions in Neurology.* 14:77-82.

[19] Hachinski, V. (2007) The 2005 Thomas Willis lecture: Stroke and vascular cognitive impairment: a transdisciplinary, translational and transactional approach. *Stroke*. 38(1):1396.

[20] Moorhouse, P., Rockwood, K. (2008) Vascular cognitive impairment: current concepts and clinical developments. *Lance Neurol.* 7(3):246-255.

[21] O'Brien, J.T., Erkinjuntti, T., Reisberg, B., et al. (2003) Vascular cognitive impairment. *Lancet Neurol.* 2(2):89-98.

[22] Erkinjuntti, T., Gauthier, S. (2009) The concept of vascular cognitive impairment. *Front Neurol Neurosci*. 24:79-85.

[23] Black, S., Iadecola, C. (2009) Vascular cognitive impairment: small vessels, big toll: introduction. *Stroke*. 40(3 Suppl):S38-9.

[24] DeCarli, C., Massaro, J., Harvey, D., et al. (2005) Measures of brain morphology and infarction in the Framingham Heart Study: establishing what is normal. *Neurobiol Aging*. 26(4):491-510.

[25] Longstreth, W.T.Jr, Manolio, T.A., Arnold, A., et al. (1996) Clinical correlates of white matter findings on cranial magnetic resonance imaging of 3301 elderly people: the Cardiovascular Health Study. *Stroke*. 27(8):1274-1282.

[26] Au, R., Massaro, J.M., Wolf, P.A., et al. (2006) Association of white matter hyperintensity volume with decreased cognitive functioning: the Framingham Heart Study. *Arch Neurol*. 63(2):246-250.

[27] de Groot, J.C., de Leeuw, F.E., Oudkerk, M., et al. (2000) Cerebral white matter lesions and cognitive function: the Rotterdam Scan Study. *Ann Neurol*. 47(2):145-151.

[28] Longstreth, W.T.Jr, Arnold, A.M., Beauchamp, N.J.Jr, et al. (2005) Incidence, manifestations, and predictors of worsening white matter on serial cranial magnetic resonance imaging in the elderly: the Cardiovascular Health Study. *Stroke*. 36(1):56-61.

[29] Schmidt, R., Ropele, S., Enzinger, C., et al. (2005) White matter lesion progression, brain atrophy, and cognitive decline: the Austrian Stroke Prevention study. *Ann Neurol*. 58(4):610-616.

[30] Hainsworth, A.H., Markus, H.S. (2008) Do in vivo experimental models reflect human cerebral small vessel disease? A systematic review.*J Cereb Blood Flow Metab*. 28(12):1877-1891.

[31] Yanagisawa, M., Kurihara, H., Kimura, S., Goto, K., Masaki, T. (1988) A novel peptide vasoconstrictor, endothelin, is produced by vascular endothelium and modulates smooth muscle Ca2+ channels. *J Hypertens Suppl.* 6(4):S188-91.

[32] Corbett, D., Harley, C., Moody-Corbett, F., et al. (2006) *Neurosci. Abst.*582.6 (2006).

[33] Sekhon, L.H., Morgan, M.K., Spence, I., Weber, N.C. (1994) Chronic cerebral hypoperfusion and impaired neuronal function in rats. *Stroke*. 25(5):1022-7

[34] Pappas, B.A., de la Torre, J.C., Davidson, C.M., Keyes, M.T., Fortin, T. (1996) Chronic reduction of cerebral blood flow in the adult rat: late-emerging CA1 cell loss and memory dysfunction. *Brain Res*. 708(1-2):50-8.

[35] de la Torre, J.C., Fortin, T., Park, G.A., Butler, K.S., Kozlowski, P., Pappas, B.A., de Socarraz, H., Saunders, J.K., Richard, M.T. (1992) Chronic cerebrovascular insufficiency induces dementia-like deficits in aged rats. *Brain Res*. 582(2):186-95.

[36] Knopman, D., Boland, L.L., Mosley, T., Howard, G., Liao, D., Szklo, M., McGovern, P., Folsom, A.R. (2001) Cardiovascular risk factors and cognitive decline in middle-aged adults. *Neurology.* 56(1):42-8.

[37] Weiss, U., Bacher, H., Vonbank, H., Kemmler, G., Lingg, A., Marksteiner, J. (2003) Cognitive Impairment: Assessment with Brain Magnetic Resonance Imaging and Proton Magnetic Resonance Spectroscopy. J Clin Psychiatry. 64:235-242

[38] Sachdev, P., Wen, W., Chen, X., Brodaty, H. (2007) Progression of white matter hyperintensities in elderly individuals over 3 years. Neurology. 68(3): 214-222

[39] Felber, S.R. (2002) Magnetic Resonance in differential diagnosis of dementia. J Neural Trans. 109(7-8):1045-1051

[40] Alberts, M.J., Faulstich, M.E., Gray, L. (1992) Stroke with negative brain magnetic resonance imaging.*Stroke.* 23(5):663-7.

[41] Moseley, M.E., Cohen, Y., Mintorovitch, J., Chileuitt, L., Shimizu, H., Kucharaczyk, J., Wendland, M.F., Weinstein, P.R. (1990) Early detection of regional cerebral-ischemia in cats - comparison of diffusion-weighted and T2-weighted MRI and spectroscopy. Magn. Reson. Med. 14:330-346

[42] Yuh, W.T., Crain, M.R., Loes, D.J., et al. (1991) MR imaging of cerebral ischemia: findings in the first 24 hours. *AJNR.* 12:621-629.

[43] Sen, S. (March 29, 2011) *Magnetic Resonace Imaging in Acute Stroke.* Retrieved September, 2012 from http://emedicine.medscape.com/article/1155506-overview#aw2aab6c11

[44] Neuffer, F. (n.d) *Introduction to Neuro MR.* Retrieved September, 2012 from http:// radiology.med.sc.edu/neuro%20no%20audio.ppt

[45] Rajeshkannan R, Moorthy S, Sreekumar KP, Rupa R, Prabhu NK. (2006) Clinical applications of diffusion weighted MR imaging: A review. *Indian J Radiol Imaging* 16:705-710

[46] Augustin, M., Bammer, R., Simbrunner, J., Stolberger, Ro., Hartung, H.-P., Fazekas, F. (2000) Diffusion-weighted Imaging of Patients with Subacute Cerebral Ischemia: Comparison of Conventional and Contrast-enhanced MR Imaging. *Ann J Neuroradiol.* 21:1596-1602.

[47] Thurnher, M. (April 30, 2008) Brain Ischemia – Imaging in Acute Stroke. Retrieved September 8, 2012 from http://www.radiologyassistant/nl/en/483910a4b6f14

[48] Lutsep, H.L., Albers, G.W., DeCrespigny, A., Kamar, G.N., Marks, M.P., Moseley, M.E. (1997) Clinical Utility of Diffusion-weighted Magnetic Resonance Imaging in the Assessment of Ischemic Stroke. *Ann Neurol.* 41:574-580.

[49] Schaefer, P., Grant, P.E., Gonzales, R.G. (2000) Diffusion-weighted MR Imaging of the Brain. *Radiology.* 217:331-345.

[50] Schlaug, G., Siewert, B., Benfield, A., Edelman, R., Warach, S. (1997) Time course of the apparent diffusion coefficient (ADC) abnormality in human stroke. *Neurology.* 49:113-119.

[51] Purcell, E.M., Torrey, H. C., Pound, R. V. (1946) Resonance Absorption by Nuclear Magnetic Moments in a Solid. *Physical Review.* 69 (1,2): 37-38

[52] Bloch, F., Hansen, W.W., Packard, M. (1946) The Nuclear Induction Experiment. *Physical Review.* 70: 474-485

[53] Liang, Z.-P., Laurterbur, P. C. (2000) *Principles of Magnetic Resonance Imaging.* New Jersey. Wiley-IEEE Press

[54] Puddephat, M. (2010). *Principles of Magnetic Resonance Imaging.* Retrieved June 2012 from: http://www.mikepuddephat.com/Page/1603/Principles-of-magnetic-resonance-imaging

[55] Hanson, L.G., (2008) Is Quantum Mechanics Necessary for Understanding Magnetic Resonance? *Concepts in Magnetic Resonance.*32A(5): 329-340

[56] Clare, S. (2006) *Functional MRI: Methods and Applications - Chapter 2.* Retrieved June 2012 from: http://users.fmrib.ox.ac.uk/~stuart/thesis/chapter_2/chapter2.html

[57] Maher, K. (2006). *Basic Physics of Nuclear Medicine - MRI & Nuclear Medicine.* Retrieved June 2012 from: http://en.wikibooks.org/wiki/Basic_Physics_of_Nuclear_Medicine/MRI_%26_Nuclear_Medicine

[58] Callaghan, P.T., (1991) Principles of Nuclear Magnetic Resonance Microscopy. Oxford Science Publications.

[59] Hashemi, Ray H., Bradley, William G. Jr., Lisanti, Christopher J. (2010) *MRI: The Basics (3rd Edition).* Pennsylvania. Lippincott Williams & Wilkins.

[60] Bushberg, Jerrod, Siebert, J. Anthony, Leidholdt, Edwin M., Boone, John M. (2001) *The Essential Physics of Imaging.* Pennsylvania. Lippincott Williams & Wilkins; 2 edition. Pp 373-467

[61] Berstein, Matt A., King, Kevin F., Zhou, Xiaohong Joe. (2004) *Handbook of MRI Pulse Sequences*.- Academic Press. Pp 683, 774-784

[62] Rooney, W.D., Johnson, G., Li, X., Cohen, E.R., Kim, S-G., Ugurbil, K., Springer, C.S. Jr. (2007) Magnetic Field and Tissue Dependencies of Human Brain Longitudinal $^{1}H_2O$ Relaxation in Vivo. *Magnetic Resonance in Medicine*. 57:308-318.

[63] Guilfoyle, D.N., Dyakin, V.V., Shea, J.O., Pell, G.S. and Helpern, J.A. (2003) Quantitative Measurements of Proton Spin-Lattice (T1) and Spin-Spin (T2) Relaxation Times in the Mouse Brain at 7.0T. *Magnetic Resonance in Medicine*. 49:576-580.

[64] Ren, J., Dimitrov, I., Sherry, A.D., Mallow, C.R. (2008) Composition of adipose tissue and marrow fat in humansby ^{1}H NMR at 7 Tesla. *Journal of Lipid Research*. 49:2055-2062.

[65] Crémillieux, Y., Ding, S., Dunn, J.F. (1998) High-Resolution In Vivo Measurements of Transverse Relaxation Times in Rats at 7 Tesla. *Magnetic Resonance in Medicine.* 39:285-290.

[66] Lauterbur, P. (1973) Image Formation by Induced Local Interactions Examples Employing Nuclear Magnetic Resonance. *Nature*. 242: 190-191

[67] Ljunggren, S. (1983) A Simple Graphical Representation of Fourier-Based Imaging Methods. *Journal of Magnetic Resonance*. 54: 338-343

[68] Twieg, D. B. (1983) .The k-trajectory formulation of the NMR Imaging Process with applications in analysis and synthesis of imaging Methods.*Med. Phys.* 10(5): 610-621

[69] Bitar, R., Leung, G., Perng, R., Tadros, S., Moody, A.R., Sarrazin, J., McGregor, C., Christakis, M., Symons, S., Nelson, A., and Roberts, T.P. (2006) MR Pulse Sequences: What every radiologist wants to know but is afraid to ask. *Radiographics*. 26(3): 513-37. http://www.ncbi.nlm.nih.gov/pubmed/16549614

[70] Plewes, Donald B., Kucharczyk, Walter. (2012) Physics of MRI: A Primer. *Journal of Magnetic Resonance Imaging*. 35: 1038-1054

[71] Zou, K.H., Warfield, S.K., Bharatha, A., Tempany, M.C., Kaus, M.R., Haker, S.J., Wells, W.M., Jolesz, F.A., Kikinis, R. (2004) Statistical Validation Image Segmentation Quality Based on a Spatial Overlap Index. *AcadRadiol*. 11:178-189.

[72] Frahm, J, Michaelis, T, Merboldt, K.D., Bruhn, H., Gyngell, M.L., Hanicke, W. (1990) Improvements in Localized Proton NMR Spectroscopy of Human Brain, Water Suppression, Short Echo Times, and 1 mL Resolution, *Journal of Magnetic Resonance*. 90(3): 464-473

[73] Hamilton, Gavin, Middleton, Michael S., Bydder, Mark, Yokoo, Takeshi, et al. (2009) The Effect of PRESS and STEAM Sequences on Magnetic Resonance Spectroscopic Liver Fat Quantification. *J MagnReson Imaging*. 30 (1): 145-152

[74] Haase, A., Frahm, J., Hanicke, W., Matthaei. (1985) ^{1}H NMR chemical shift selective (CHESS) imaging.*Phys. Med. Biol.* 30(4):341-344

[75] Drost, Dick J., Riddle, William R., Clarke, Geoffrey D. (2002) Proton magnetic resonance spectroscopy in the brain: Report of AAPM MR Task Group #9. *Medical Physics*. 29 (9): 2177-2197

[76] Qayyum, Aliya. (2009) MR Spectroscopy of the Liver: Principles and Clinical Applications. *RadioGraphics.*29: 1653-1664

[77] Hennig, J., Nauerth, A., Friedburg, H. (1986) RARE Imaging: A Fast Imaging Method for Clinical MR. *Magnetic Resonance in Medicine*. 3(6): 823-833

[78] Andreollo, N.A., dos Santos, E.F., Araujo, M.R., Lopes, L.R. (2012) Rat's Age versus Human's Age: What is the Relationship. *ABCD Arq Bras Cir Dig.* 25(1):49-51.

[79] Paxinos, G., Watson, C. (1997) *The Rat Brain in Stereotaxic Coordinates - 3rd Edition.* Academic Press

[80] Cordova, C., Jackson, D., Granter-Button, S., Hewlett, K., Langdon, K., Jeffers, M., Corbett, D. (2011) A rodent model of covert stroke: effects of chronic hypoperfusion and medial thalamic stroke on attention set shifting ability.*Canadian Stroke Congress*. Poster

[81] Pfefferbaum, A., Adalsteinsson, E., Sullivan, E.V. (2004) In vivo structural imaging of the rat brain with 3-T clinical human scanner. *Journal of Magnetic Resonance Imaging.* 20:779-785

[82] Carmelli, D., Swan, G.E., Reed, T. (2002) Quantitative genetic modeling of regional brain volumes and cognitive performance in order male twins. *Biol Psychol.* 61:139-155

[83] Pfefferbaum, A., Sullivan, E.V., Swan, G.E., Carmelli, D. (2000) Brain structure in men remains highly heritable in the seventh and eight decades of life. *Neurobiol Aging.* 21:63-74

[84] Sullivan, E.V., Pfefferbaum, A., Swan, G.E., Carmelli, D. (2001) Heritability of hippocampal size in elderly twin men: equivalent influence from genes and environment. *Hippocampus.* 11:754-762

[85] Longstreth, W.L. (2005) Brain Vascular Disease Overt and Covert. Stroke. 36:2062-2063

[86] Zijdenbos, A., Dawant, B.M., Margolin, R., Palmer, A.C. (1994) Morphometric Analysis of White Matter Lesions in MR Images: Method and Validation. *IEEE Transactions on Medical Imaging.* 13(4):716-724

[87] Scheenstra, A.E., van de Ven, R.C., van der Weerd, L, van den Maagdenberg, A.M., Dijkstra, J. (2009) Automated segmentation of in vivo and ex vivo mouse brain magnetic resonance images. *Mol Imaging.* 8(1):35-44

[88] Ali, A.A., Dale, A.M., Badea, A., Johnson, G.A. (2005) Automated segmentation of neuroanatomical structures in multispectral MR microscopy of the mouse brain. *Neuroimage.* 27(2):425-435.

Appendix A

A.1 *In Vivo* Imaging - Selection of the ROI (Scout Scans)

To fix the orientation of the image, scout scans were used to obtain one slice with the following parameters: 4.0 cm^2 FOV, 1 average, TR = 3000 ms, effective TE = 15 ms, 1.00 mm slice thickness, 0.3125×0.3125×1 mm^3 resolution, RARE factor 36, acquisition time of 6 seconds.

Scout Scan 1: The first scout scan shows the axial slice of the brain at the centre of the magnet (Figure A.1.1). The brain in this scan will not likely be horizontal to the bottom of the image. Also this image shows an axial slice further back in the brain from the targeted area, therefore the rat will need to be moved to centre the brain. Further scout scans are needed in order to adjust or ensure that the images are centred in the brain and that the axes of the image line up with axes of the brain. Figure A.1.2 shows an axial image which has the rat brain in the targeted area. This axial slice will be then used for the next scout scan.

Figure A.1.1: Axial image showing the entire head of the rat at the centre of the magnet. Further scout scans need to be taken in order to align the brain so that the images are centred on the brain.

Scout Scan 2: Using the Geometry Editor, the axial slice is used as a reference to create a sagittal image (Figure A.1.2). The slice volume (pink box) contains the volume that will be imaged of the brain. This pink box is positioned or aligned along the centreline of the brain. This produces a sagittal image (Figure A.1.3) at the middle of the brain and the

horizontal axis of the image is aligned with the anterior-posterior axis of the brain, as per Figure 3.5.

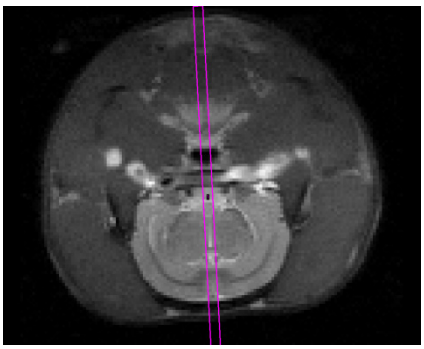

Figure A.1.2: Axial geometry is used. Pink box contains the brain that is to be imaged, and is aligned to the centreline of the brain to produce a sagittal image.

Scout Scan 3: The sagittal image from scout scan 2 is used as a reference to create a coronal image in this scout scan (Figure A.1.3). The slice volume is aligned vertically 2mm from the bottom of the olfactory bulb, and 1.5 mm above the top edge of the spinal cord.

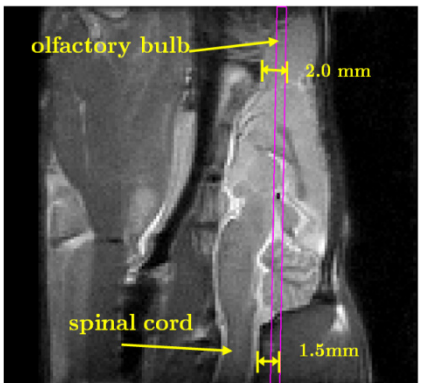

Figure A.1.3: Centred sagittal slice. Next scout slice selected (pink box) in the middle the brain to produce a coronal image.

The coronal slice is produced (Figure A.1.4) with the vertical axis of the image being aligned with the head-foot axis of the brain, and the horizontal axis of the image is aligned with the medial-lateral axis of the brain as per Figure 3.5.

Scout Scan 4: This coronal image (Figure A.1.4) produced from scout scan 3 is used as a reference. The slice volume was aligned along the centreline of the brain, in order to ensure that the images will be centred to the brain. From this scout scan, another sagittal slice was produced (Figure A.1.5) which will be more centred than the previous sagittal image. This sagittal image has its vertical and horizontal axes of the image aligned respectively with the head-foot and anterior-posterior axes of the brain.

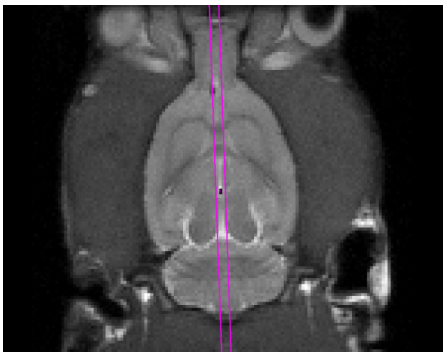

Figure A.1.4: Centred coronal slice. Next scout slice aligned to the centreline of the brain on this coronal slice to produce a sagittal image.

Scout Scan 5: The sagittal image (Figure A.1.5) produced from the previous scan will be used to obtain an axial slice in this scout scan. The slice volume is aligned horizontally at 2 mm below the anterior commissure.

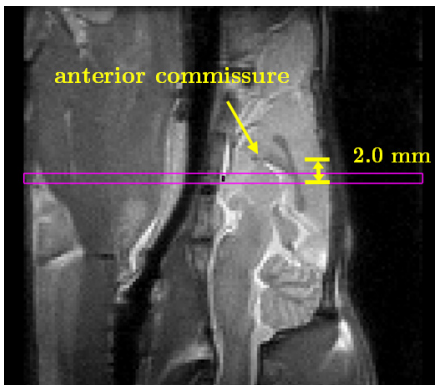

Figure A.1.5: Sagittal slice. Slices are placed 2.0mm below the anterior commissure. This slice will produce an axial image.

For additional verification, the coronal image obtained in scout scan 3 can also be used to obtain the axial image. The slice volume is aligned horizontally along the coronal image (Figure A.1.6).

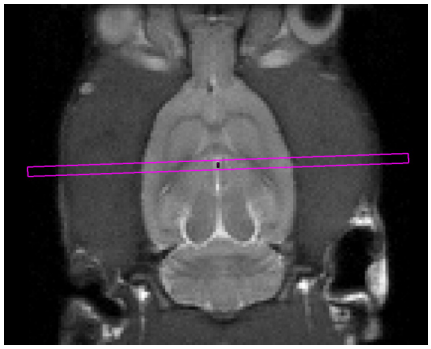

Figure A.1.6: Coronal slice obtained from scout scan 4 is used to select an axial slice. Slice volume was placed horizontal to the coronal image (pink box).

For both of these options, axial image is produced (Figure A.1.7) with the appropriate angles needed to centre the images axes to the axes of the brain, where the vertical and horizontal axes of the image being aligned with the anterior-posterior and medial-lateral axes of the brain. The parameters of both options can be compared, and modified as necessary.

Figure A.1.7: Centred axial slice. The study slice volume (pink box) indicating that the slices will encompass the entire brain.

The axial image (Figure A.1.7) is used to select the image volume for the study. The volume contained in the pink box shows encompass the entire brain but not the entire head in that slice. This centred axial image will be used to acquire T_2-weighted images (in the axial position) taken over the central region of the brain (Figure 3.13). This is done in order to assess for lesion and white matter hyperintensity, by measuring the lesion volumes

(ventricle volumes), which will be discussed in Section 3.5. The amount of wraparound due to phase wrapping is small and affects the outer regions of the image containing muscle and not brain.

A.2 *Ex Vivo* Imaging - Selection of the ROI (Scout Scans)

Prior to data image acquisition, scout scans were performed in order to centre the rat brain/coil in the magnet. Once centred, the desired ROI was obtained using scout scans for axial, sagittal and coronal images of the brain. These were used in order to consistently acquire images from the same volume of brain in each rat. The scout scans obtained one slice with the following parameters: 3.0 cm^2 FOV, 1 average, TR = 3000 ms, effective TE = 15 ms, 1.00 mm slice thickness, 0.2343 × 0.2343 × 1 mm^3 resolution, RARE factor 36, acquisition time of 6 seconds. This type of scout scan (HASTE) was used because of the relatively short acquisition time. This however produced images which did not have a lot of contrast between the features (such as the anterior commissure and the surrounding grey matter) in the brain required in later scout scans to define the ROI.

Another type of scout scan was also used (RARE), because it produced better resolution images, where the contrast between features within the brain was needed, however the acquisition time was much longer than HASTE. The parameters for this RARE scout scan was: 43.0 cm^2 FOV, 1 average, TR = 840 ms, effective TE = 28 ms, 1.00 mm slice thickness, 0.1563×0.1563×1 mm^3 resolution, RARE factor 4, acquisition time of 54 seconds. HASTE scout scans were used to produce the following figures provided in this section.

Scout scan 1: This scout scan shows the position of the brain in the axial position at the centre of the magnet (Figure A.2.1). The brain will not likely be horizontal to the bottom of the image, and therefore further scout scans will be needed in order to adjust or ensure that the images are centred in the brain. By doing these scout scans the axes of the image are then lined up with axes of the brain, and the required ROI is contained within the image.

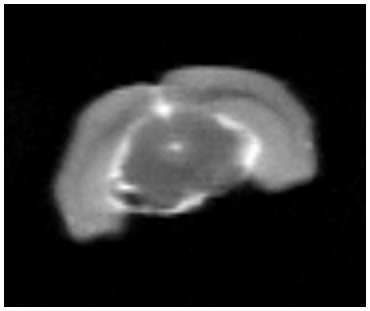

Figure A.2.1: Scout scan 1 - Axial image: Image of the position of the brain in the axial position at the centre of the magnet. Further scout scans are required in order to obtain the proper alignment of the axes of the brain to the axes of the image.

Scout scan 2: With the use of Geometry Editor the axial image is used as a reference in order to choose the next slice. As shown in Figure A.2.2 the slice volume was first aligned horizontally to the bottom of brain in this axial image, where the histology slide touches the brain (yellow box). Then the slice volume was rotated 90 degrees and moved to the midline of the brain, which is vertical with respect to the brain (pink box).

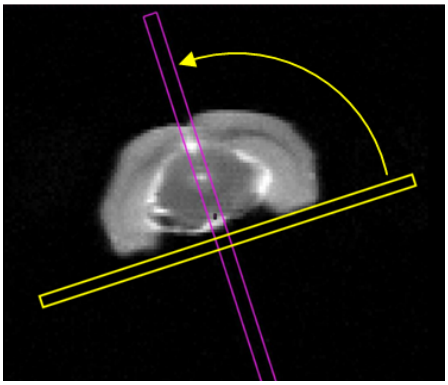

Figure A.2.2: Scout scan 2: Axial geometry was used to select the sagittal image plane. Slice volume was aligned to the bottom of the brain image (yellow box). This slice volume was set perpendicular to the bottom of the brain (90 degree was added) and then aligned to the centreline of the brain (pink box).

This scout scan produces a sagittal image at the middle of the brain with the vertical axis of the image is aligned with the head-foot axis of the brain (Figure A.2.3), and the horizontal axis of the image is aligned with the anterior-posterior axis of the brain as per Figure 3.5.

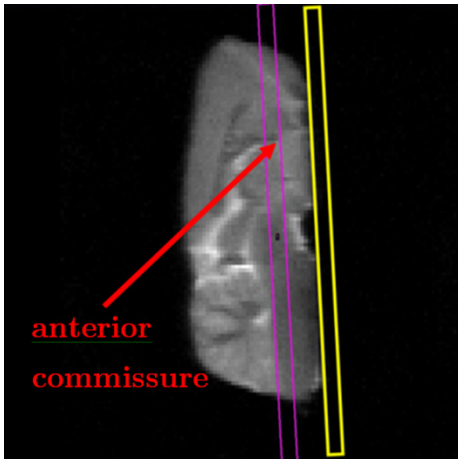

Figure A.2.3: Sagittal slice, as produced by scout scan 2. This sagittal slice was used to select a coronal slice in scout scan 3. Slice volume was aligned to the bottom of the brain image (yellow box). This slice volume was then moved to the middle of the sagittal slice, slice centred on the anterior commissure (pink box).

Scout scan 3: This scan was chosen using the sagittal image from Figure A.2.3 as a reference. The slice volume was selected by centering the 'pink rectangle' on the middle of the sagittal slice. This is done by aligning the slice to the edge where the histology slide hits the brain (yellow box), and then moving the slice to the approximate middle of the brain (pink box) (Figure A.2.3).

This vertical slice will produce a coronal image (Figure A.2.4) with the vertical axis of image being aligned with the head-foot axis of the brain and the horizontal axis of the image aligned with the medial-lateral axis of the brain, as per Figure 3.5.

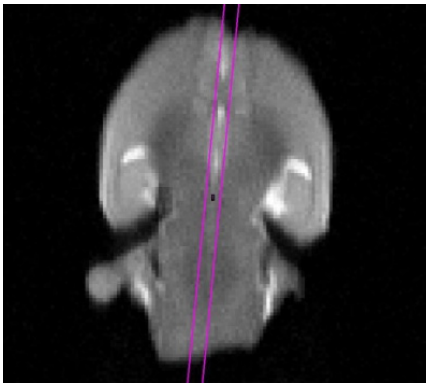

Figure A.2.4: Centred coronal slice as produced by scout scan 3. This coronal slice was used to select a sagittal slice in scout scan 4. The slice volume was aligned to the centreline of the coronal brain slice.

Scout scan 4: Using the coronal image on Figure A.2.4, the slice volume is aligned to the centreline of the brain.. This vertical slice will produce a sagittal image (Figure A.2.5) with the vertical axis of image being aligned with the head-foot axis of the brain and the horizontal axis of the image aligned with the anterior-posterior axis of the brain, as per Figure 3.5.

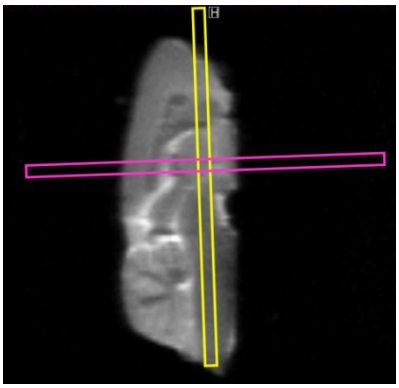

Figure A.2.5: Centred sagittal slice as produced by scout scan 4. This sagittal slice was used to select an axial slice in scout scan 5. Slice volume was aligned to the centre and horizontal to the sagittal image (pink box).

Scout scan 5: Using the sagittal image on Figure A.2.5, the slice volume is aligned to the middle of the brain, similar to scout scan 3 (yellow box). It was then rotated 90 degrees, aligning the slice volume horizonally on the sagittal image (pink box) so that an axial image will be made (Figure A.2.7).

For additional verification, the coronal image obtained in (scout scan 3) can also be used to obtain the axial image. From the coronal slice, the slice volume is aligned to the midline of the coronal slice (yellow box) and then rotated 90 degrees to obtain a slice that is horizontal to the coronal image (pink box)(Figure A.2.6). The parameters of both options can be compared and modified as necessary.

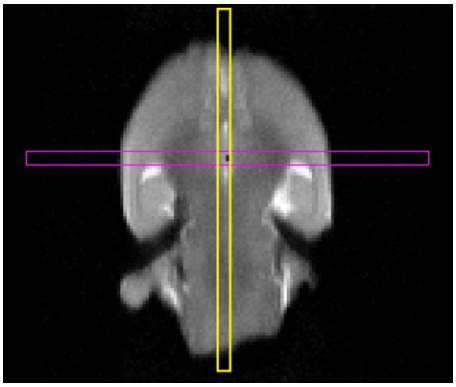

Figure A.2.6: Coronal slice obtained from scout scan 3 is used to select an axial slice in scout scan 5. Slice volume was placed horizontal to the coronal image (pink box).

The axial image that is produced from scout scan 5 (Figure A.2.7) should have similar left/right features in the brain, showing accurate alignment of all axes of the brain and the images. This axial slice will be centred, with the vertical and horizontal axes of the image aligned with the anterior-posterior and medial-lateral axes of the brain, respectively, as per Figure 3.5. This axial slice will then be used to select slices for the high resolution images described in Section 3.5.2.

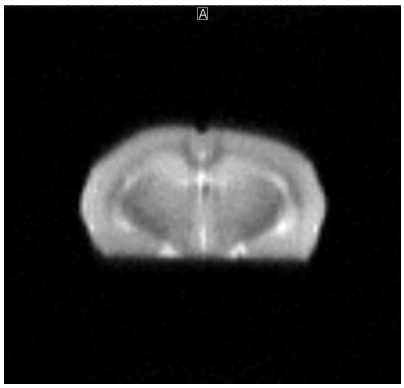

Figure A.2.7: Axial image. Scout scan containing a slice of the brain with symmetric left and right features of the brain.